

Nanoscale four-point charge transport measurements in topological insulator thin films

Arthur Leis

Information

Band / Volume 70

ISBN 978-3-95806-580-2

Forschungszentrum Jülich GmbH
Peter Grünberg Institut (PGI)
Quantum Nanoscience (PGI-3)

Nanoscale four-point charge transport measurements in topological insulator thin films

Arthur Leis

Schriften des Forschungszentrums Jülich
Reihe Information / Information

Band / Volume 70

ISSN 1866-1777

ISBN 978-3-95806-580-2

Bibliografische Information der Deutschen Nationalbibliothek.
Die Deutsche Nationalbibliothek verzeichnet diese Publikation in der
Deutschen Nationalbibliografie; detaillierte Bibliografische Daten
sind im Internet über <http://dnb.d-nb.de> abrufbar.

Herausgeber
und Vertrieb: Forschungszentrum Jülich GmbH
 Zentralbibliothek, Verlag
 52425 Jülich
 Tel.: +49 2461 61-5368
 Fax: +49 2461 61-6103
 zb-publikation@fz-juelich.de
 www.fz-juelich.de/zb

Umschlaggestaltung: Grafische Medien, Forschungszentrum Jülich GmbH

Druck: Grafische Medien, Forschungszentrum Jülich GmbH

Copyright: Forschungszentrum Jülich 2021

Schriften des Forschungszentrums Jülich
Reihe Information / Information, Band / Volume 70

D 82 (Diss. RWTH Aachen University, 2021)

ISSN 1866-1777
ISBN 978-3-95806-580-2

Vollständig frei verfügbar über das Publikationsportal des Forschungszentrums Jülich (JuSER)
unter www.fz-juelich.de/zb/openaccess.



This is an Open Access publication distributed under the terms of the [Creative Commons Attribution License 4.0](https://creativecommons.org/licenses/by/4.0/),
which permits unrestricted use, distribution, and reproduction in any medium, provided the original work is properly cited.

Abstract

Topological insulator (TI) materials, with their exotic electronic properties, cause a growing interest in modern solid state physics as promising systems for novel applications. This work presents the measurement and the analysis of characteristic transport properties of topological insulator films on the nanometer scale. The use of a multi-tip scanning tunneling microscope (STM) allows for position-dependent electrical measurements on the surface of the samples. For this purpose, the high degree of versatility of the individual tips is exploited to realize resistance measurements in dedicated configurations, even at the nanoscale. Chapter 2 presents an introduction into the operation principle of the instrument and the position-dependent four-point measurement technique. The fundamental relation between the measured resistance and the conductivity of the underlying system is derived. Furthermore, the outlined technique and its experimental capabilities are demonstrated on the example of a SrTiO₃ sample, which allows to comprehend the influence of dimensionality on the resistance. In chapter 3, a more sophisticated method of tip positioning based on overlaps of STM scans is presented. Using this method, it is possible to realize four-point measurement configurations on the nanoscale with considerable spatial precision. Chapter 4 provides an introduction into the material class of topological insulators, focusing on the origin of the associated characteristic properties. In chapters 5 – 7, nanoscale four-point resistance measurements on thin films of the strong topological insulator (Bi_{1-x}Sb_x)₂Te₃, enabled by the demonstrated positioning technique, are presented. Chapter 5 is focused on the electrical detection of the intrinsic spin polarization of the surface states of a TI. For this purpose, a ferromagnetic STM tip is used to extract the spin-dependent electrochemical potential of carriers during charge transport. Chapters 6 and 7 are dedicated to the topological phase transition of a 3D TI thin film into a quantum spin Hall (QSH) insulator system with reduced film thickness. In chapter 6, the necessary condition for such a phase transition, namely the interaction of the topological surface states on the two interfaces of the thin film, is studied by means of charge transport. Chapter 7 presents a measurement scheme for helical edge states, which are the sufficient condition for the formation of a QSH phase. While a QSH phase is not

observed in the investigated $(\text{Bi}_{0.16}\text{Sb}_{0.84})_2\text{Te}_3$ system, the demonstrated technique provides a generic method for the detection of topological phases in transport.

Kurzfassung

Materialien für topologische Isolatoren (TI) erwecken mit ihren exotischen elektronischen Eigenschaften ein wachsendes Interesse als vielversprechendes System für neuartige Anwendungen im Bereich der modernen Festkörperphysik. In diesem Werk wird die Messung und die Interpretation charakteristischer Ladungstransporteigenschaften in dünnen Filmen topologischer Isolatoren auf der Nanometer-Skala präsentiert. Durch den Einsatz eines Multispitzen-Rastertunnelmikroskops ist es möglich, positionsabhängige elektrische Messungen auf der Oberfläche der Proben durchzuführen. Dabei wird die vielseitige Einsetzbarkeit der einzelnen Spitzen ausgenutzt, um Widerstandsmessungen in spezifischen Konfigurationen bis hin zur Nanometer-Skala umzusetzen. Kapitel 2 stellt eine Einleitung in das Funktionsprinzip des Instruments und in die Technik des positionsabhängigen Widerstands dar. Dabei wird der fundamentale Zusammenhang zwischen dem gemessenen Widerstand und der zugrundeliegenden Leitfähigkeit des Systems hergeleitet. Des Weiteren wird die dargelegte Technik und ihre experimentellen Möglichkeiten am Beispiel einer SrTiO_3 Probe vorgeführt. In Kapitel 3 wird eine weiterentwickelte Positionierungsmethode, basierend auf Rastertunnelmikroskop-Aufnahmen, präsentiert. Durch diese Methode ist es möglich, Vierpunkt-Messkonfigurationen mit beträchtlicher räumlicher Auflösung auf der Nanometer-Skala zu realisieren. Kapitel 4 bietet eine Einführung in die Materialklasse der topologischen Isolatoren mit Hinblick auf den Ursprung der zugehörigen charakteristischen Eigenschaften. In den Kapiteln 5 – 7 werden, ermöglicht durch die demonstrierte Positionierungsmethode, Messungen des Vierpunktwidestands dünner Filme des starken topologischen Isolators $(\text{Bi}_{1-x}\text{Sb}_x)_2\text{Te}_3$ auf der Nanoskala präsentiert. Kapitel 5 befasst sich mit der elektrischen Detektion der intrinsischen Spinpolarisation der Oberflächenzustände eines topologischen Isolators. In diesem Zusammenhang wird eine ferromagnetische Spitze benutzt, um das spin-abhängige elektrochemische Potential der Ladungsträger im Transport zu erlangen. Kapitel 6 und 7 behandeln den topologischen Phasenübergang eines dünnen 3D TI Films in ein Quanten-Spin-Hall (QSH) System durch die Reduktion der Schichtdicke. In Kapitel 6 wird die notwendige Bedingung eines solchen Phasenübergangs – die Wechselwirkung der

topologischen Oberflächenzustände auf den beiden Grenzflächen des Films – elektrisch untersucht. Kapitel 7 präsentiert ein Messverfahren für helikale Randzustände, deren Existenz die hinreichende Bedingung für das Entstehen einer QSH Phase ist. Obwohl im untersuchten $(\text{Bi}_{0.16}\text{Sb}_{0.84})_2\text{Te}_3$ System keine QSH Phase beobachtet wird, stellt die vorgeführte Methode ein allgemeines Mittel zur Identifikation topologischer Phasen dar.

Contents

1. Introduction	1
2. Four-point measurement technique	3
2.1. Experimental setup	3
2.2. Local four-point resistance measurement technique	5
2.2.1. Two-dimensional conductivity	7
2.2.2. Three-dimensional conductivity	9
2.2.3. Distance-dependent resistance measurement	11
2.2.4. Geometric constraints	13
2.3. Example measurements on SrTiO ₃	16
2.3.1. SrTiO ₃ material system	16
2.3.2. Experimental procedure	18
2.3.3. Evolution of conductivity after thermal reduction	19
2.4. Summary	28
3. Nanoscale tip positioning	29
3.1. Motivation	29
3.2. Principle of positioning	31
3.3. Sources of image distortion	33
3.4. Calibration of non-linear piezo response	34
3.5. Example measurement	37
4. BiSbTe ₃ material system	41
4.1. Topological insulators	41
4.1.1. Chern number	41
4.1.2. Z ₂ topological insulator	43
4.1.3. 2D and 3D topological insulators	44
4.2. BiSbTe ₃ thin films	48

5. Spin-polarized charge current in a topological insulator	53
5.1. Preparation of Ni tips	54
5.1.1. Etching setups	54
5.1.2. Etching procedure	56
5.2. Characterization of the electromagnet	58
5.3. Measurement of the intrinsic TSS spin polarization	60
5.3.1. Sample conductivity	61
5.3.2. Principle of spin voltage detection	63
5.3.3. Spin voltage measurement scheme	68
5.3.4. Distance-dependent four-point measurements	69
5.3.5. Determination of the TSS spin polarization	74
5.4. Effect of magnetic fields in infinite plane samples	76
5.5. Summary	78
6. Thickness-dependent sheet conductivity of ultra-thin topological insulator films	81
6.1. Hybridization of topological surface states	82
6.2. Sample characteristics	83
6.3. Thickness-dependent sheet conductivity measurements	88
6.3.1. Modeling the film conductivity	91
6.4. Summary	97
7. Search for ballistic 1D channels on topological insulator edges	99
7.1. Transition into two-dimensional topological insulator regime	100
7.2. Edge state measurement scheme	101
7.2.1. Scanning tunneling spectroscopy	102
7.2.2. Nanoscale transport measurements	104
7.3. Four-point resistance measurement directly on a step edge	105
7.4. Four-point resistance measurements in proximity to a step edge	108
7.4.1. Influence of a 1D channel on 2D resistance measurements	109
7.4.2. Measurement results	110
7.5. Summary	114
8. Conclusion and outlook	115
Bibliography	133
Publications	135
Acknowledgements	137

A. Detailed derivations	139
A.1. Resistance uncertainty	139
A.2. Dimensionless tip distance χ	141
B. Additional data	143
B.1. Four-point measurements on different $(\text{Bi}_{0.16}\text{Sb}_{0.84})_2\text{Te}_3$ terraces	143
B.2. Analytic solution for a conductive 1D channel	146
C. Technical descriptions	149
C.1. Contacting procedure	149
C.2. Tip cleaning	150
C.2.1. Cleaning by field emission	150
C.2.2. Cleaning in hard contact	151
C.3. Preparation of UHV suitcase	151

CHAPTER 1

Introduction

Technological advances in society over the past century have led to many inventions that not only influence, but define modern everyday life. To this end, the field of condensed matter physics has continuously provided a deep understanding of electronic phenomena in solids, which ultimately allows to design devices with a specific purpose. Modern electronics development was able to harvest the benefits of various discovered electronic phenomena, resulting in fundamental components such as transistors, diodes and lasers. In the course of technological progress, due to the downscaling of device size, quantum effects have become increasingly significant and today are unavoidable. Following developments led to the conception of quantum devices, in which quantum effects not only come into effect, but are also desired and intentionally harnessed for their operation principle [1–3]. Such applications include resonant tunneling devices [4–6], quantum dot systems [7, 8] and proposed device concepts such as the spin transistor [9].

In the past years, the focus in modern research has shifted towards quantum materials [10, 11], which encompass a class of systems which have macroscopic properties that are explicitly based on the quantum nature of the electron wave function. These properties fundamentally arise from strong interactions or entanglement in the underlying systems and generally cannot be understood with conventional descriptions of matter. One category of quantum materials is that of topological insulators (TIs), which since their prediction in 2005 [12] and subsequent experimental discovery [13, 14] have raised large interest in condensed matter physics. The exotic properties of these systems arise from their topological order and include the existence of surface states that are protected by time-reversal symmetry. The topological surface states span across the bulk band gap following a linear dispersion

relation, thereby forming a so-called Dirac cone [15]. Furthermore, the charge carriers inhabiting these states have a spin that is strictly correlated to their momentum. Besides the prospect of dissipationless transport, the properties of topological insulators are promising for applications in spintronics [16] and in quantum computation [17, 18]. The latter is regarded as a possible technological revolution, with a quantum computer being able to solve specific problems faster than a classical one, as suggested by recent demonstrations of quantum supremacy [19]. Certain efforts in quantum computation are focused on approaches based on the implementation of topological insulators, in particular. In conventional quantum computation, TIs can be used as the weak link material in Josephson junctions [20], which constitute the elementary building block of superconducting qubits [21]. Beyond that, one specific approach is topological quantum computing [22–24], which opens the prospect of fault-tolerant quantum computing. The most promising system to host Majorana states [25], which are sought-after candidates for the realization of corresponding topological qubits, are topological insulators in proximity to an *s*-wave superconductor [26]. As these concepts ultimately rely on the use of topological states in an electrical circuit environment, it is crucial to demonstrate their manifestation in transport measurements.

An ideal setup to study the transport properties of topological insulator systems is offered by multi-tip scanning tunneling microscopy (STM) [27, 28]. Such an instrument consists of several individual units, each with the full functionality of a single-tip STM. The independently controlled tips can be used to establish electrical contact to the surface of an investigated sample, which opens the possibility to perform multi-terminal transport measurements. In contrast to conventional measurement setups realized by the deposition of external contacts, the STM tips can be placed in any desired configuration, which enables access to the spatial dependence of the electrical properties as a further experimental parameter. Furthermore, the small extent of the tip apices allows delicate contacting in well-defined geometries and exerts minimal influence on the integrity of the sample system. Most importantly, transport measurements in multi-tip STM systems can be carried out *in situ*, as there is no need for lithographic sample preparation in ambient conditions. This aspect is of substantial significance in regard to the case of topological insulator samples, since the auspicious topological properties are easily influenced or even destroyed upon exposure to atmospheric conditions [29–31].

The present work is dedicated to the investigation of topological insulator thin films using a multi-tip STM. The general transport measurement principle is laid out and demonstrated on an example in chapter 2. An advanced tip positioning method that enables four-tip arrangements on the nanometer scale is presented in chapter 3. Based on this technique four-point resistance measurements were performed on thin films of the compound topological insulator system $(\text{Bi}_{1-x}\text{Sb}_x)_2\text{Te}_3$, as shown in chapters 5 – 7.

Four-point measurement technique

In this chapter, the primary measurement method relevant for all measurements in this thesis is introduced. After a short introduction of the measurement setup, the four-point technique as a tool for performing charge transport measurements is presented. The theoretical model describing the spatial dependence of the electric potential resulting from an isotropic conductivity in two-dimensional and three-dimensional systems is discussed. Also, the disentangling of 2D and 3D conductivity contributions by means of the four-point resistance measurement technique is demonstrated using measurements on SrTiO₃ samples as an example.

2.1. Experimental setup

The instrument used for all measurements in this thesis is a room temperature multi-tip scanning tunnelling microscope (STM) equipped with four tips. Being situated in an ultra-high vacuum (UHV) chamber it allows for all investigations to be carried out under *in situ* conditions.

The STM itself is designed four-fold symmetric, as shown in Fig. 2.1 (a). The instrument is constituted by four *KoalaDrive* nanopositioners [32] (indicated in cyan), each attached to a slider plate (indicated in purple) sitting on three piezoelectric tubes. The STM tips, as depicted in 2.1 (b), are mounted into cylindrically-shaped detachable tip holders which are coupled magnetically to the top of each nanopositioner when inserted into the STM.

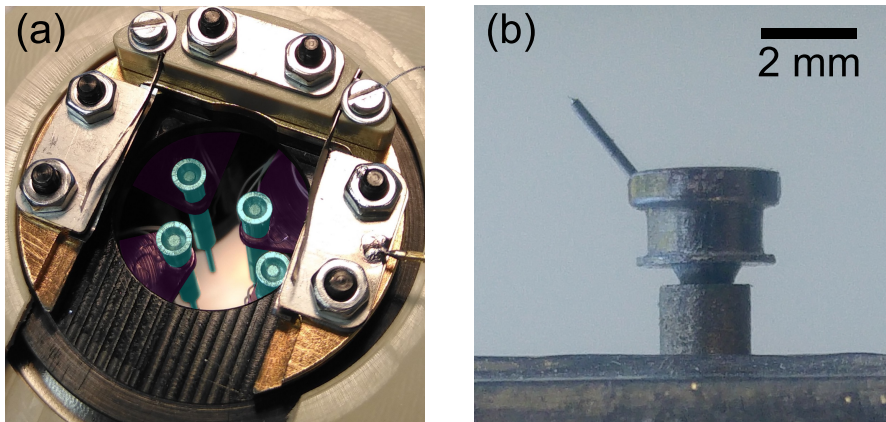


Fig. 2.1.: (a) Color-edited photograph of the multi-tip STM without tips inserted. The STM units are moved laterally by controlling a set of piezoelectric tubes below each slider plate (colored in purple). Using separate piezo elements at each nanopositioner (colored in cyan) allows vertical movement in z -direction. Samples are inserted face down into the gap between the gold- and silver-colored metal parts. (b) Photograph image of an STM tip inserted into a detachable tip holder. When mounted in the STM unit, the cylindrically-shaped tip holder sits on the top of a nanopositioner with the tip pointing towards the center of the multi-tip STM at 45° of inclination.

When mounted into the tip holders, the prepared tungsten tips have a $\sim 45^\circ$ orientation with respect to cylindrical axis of the holder, such that the four tips do not obstruct each other when moved into close proximity in the STM. More information on the instrument can be found in Ref. [28] and [33]. With each new tip mounted into the STM, a tip cleaning process using electric field emission is performed to remove residual oxide layers on the tip apex. A detailed description of the procedure can be found in appendix C.2.

Electrical control of the piezoelectric tubes holding the slider plate allows lateral movement of each STM unit, while applying voltage to the piezo element of the nanopositioner enables perpendicular z -control. With a sample inserted into the appropriate slot in the system, the nanopositioners below are oriented perpendicularly to the sample plane, so that each tip mounted on top can be approached towards the sample surface using z -movement. The contacting procedure in the frame of transport measurements is explained in detail in appendix C.1.

Each of the four STM tips has a separate electrical connection and is equipped with its own set of electronics. It is possible to apply separate bias voltages and record the current flowing through each tip, individually [34]. This way, each unit effectively functions as an individual single-tip STM, making it possible to manipulate the position and acquire STM images with

each tip. By switching a relay in each set of electronics, the STM tips can be toggled to a high-impedance mode, which is used to measure the voltage at the corresponding tip [34]. Furthermore, an additional connection to the sample insertion slot in the STM allows biasing/grounding of the sample itself or even applying a gate voltage, depending on the architecture of the sample system. With its design ensuring precise spatial control and electrical flexibility, the multi-tip STM is a highly versatile instrument that is useful when studying charge transport properties in nanoscale systems.

For visual control of the multi-tip STM, an optical microscope positioned below the STM apparatus outside the UHV chamber is used. An exemplary zoomed-out view through the microscope covering all four STM tips is shown in Fig. 2.2 (a). As the tips are navigated laterally across a sample surface, their movement can be monitored in real time, which is important for placing the tips in desired configurations. Using an optical microscope has clear advantages compared to position control via scanning electron microscopy (SEM). Besides the greater simplicity of use, optical microscopy imaging prevents any damage to pristine samples that the electron bombardment during SEM imaging would inflict [35–37].

In order to accurately realize a specific configuration of the STM tips on the surface of a sample, it is important to know the position of the tips before contacting. The optical microscope image provides an estimation, with the contact points assumed to be at the very end of the imaged tip projections. However, by determining the contact point in this way, the precision of the determination of the tip positions is limited by the resolution of the optical microscope, which is determined to $\sim 1\ \mu\text{m}$. The resulting influence of the uncertainty of tip positions on the electrical measurements is discussed quantitatively in section 2.2.3. Furthermore, it is important to consider that the actual point of contact also might not actually be at the expected point as inferred from the tip projection due to deformations of the tip apex. While this aspect is not a concern for fresh, undamaged tips, it emphasizes that careful approaching to surfaces is advisable when establishing ohmic contact.

2.2. Local four-point resistance measurement technique

As described in the previous section, the multi-tip STM is a versatile instrument that is particularly useful to acquire electrical properties of investigated samples. Using the four STM tips as electrical probes when in contact with a sample surface allows to acquire the four-point resistance, depending on the particular tip configuration.

With the to-be-investigated sample set to a floating potential, two tips (e.g. tip 1 and tip 4) are used to inject and measure a charge current I_{14} . The other two tips are used simultaneously

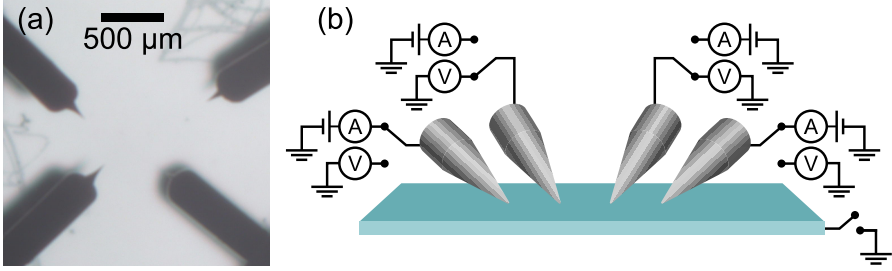


Fig. 2.2.: (a) Optical microscope image showing a zoomed-out view of the four STM tips with a sample surface in the background. Using the microscope view, tip movement is monitored in real time. For actual tip positioning, the used microscope magnification is 20 times higher. (b) Electrical setup of the STM tips for a four-point measurement. All four tips can be biased separately. When in contact with a sample surface, individual tips can be switched between current- and voltage-probe mode.

to measure the resulting potential. Technically, this procedure is enabled by the ability to switch all STM tips between current- and voltage-probe mode individually (Fig. 2.2 (b)). The recorded potential difference V_{23} between the two voltage probes is used to determine the four-point resistance

$$R^{4P} = V_{23} / I_{14} \tag{2.1}$$

corresponding to a particular tip configuration. Contrary to two-terminal measurements, the resistance obtained from this four-probe approach does not contain the contact resistance of the probing tips due to the high impedance of the voltage measurement circuit.

Stemming from the local electric potential, the four-point resistance obtained in this manner contains not solely information about intrinsic properties of the sample, but also depends on the particular geometry of the tip arrangement. Therefore, the four-point resistance of any measurement geometry needs to be deconstructed to gain insight into the desired material specific quantities. For systems with complicated shapes and anisotropies of the conductivity, this is a non-trivial task. For the case of locally isotropic conductivity, however, a simple relation can be found in one-dimensional (1D) wire, two-dimensional (2D) sheet and three-dimensional (3D) bulk systems, such that it is possible to analytically evaluate the related conductivity from the measured resistance. This is universally useful since the respective resistance models are good approximations for investigated areas where the conductivity is isotropic on the scale of the distances between the tips.

To obtain the relation between the conductivity σ of the system and the four-point resistance R^{4P} under isotropic conditions, the local form of Ohm's law

$$\vec{j}(\vec{r}) = \sigma \vec{E}(\vec{r}) \tag{2.2}$$

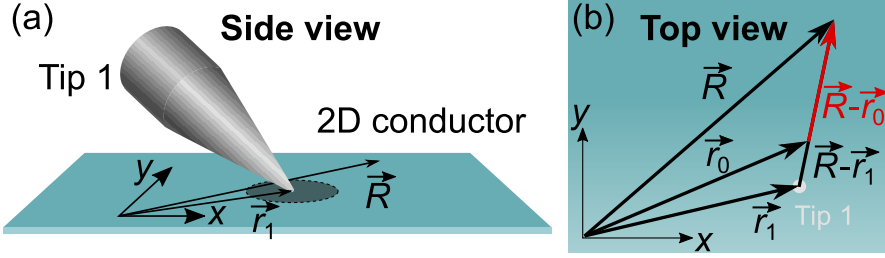


Fig. 2.3.: Conceptual sketch of current injection in a 2D conductor. **(a)** When injected into an isotropic 2D system through a point-like contact such as an STM tip, the current is distributed circularly around the point of injection. **(b)** To obtain the corresponding electric potential at \vec{R} with respect to a reference point \vec{r}_0 , the current density is integrated along a straight line connecting the two points. For simplicity, the reference point \vec{r}_0 is chosen to be between \vec{R} and the tip position \vec{r}_1 .

is used, where $\vec{j}(\vec{r})$ and $\vec{E}(\vec{r})$ are the current density and the electric field at a given point \vec{r} on the probed surface. The spatial dependence of the current density is specific to the dimensionality has to be considered separately.

2.2.1. Two-dimensional conductivity

In two-dimensional systems, the current that is injected by a single point-like electrode, e.g. tip 1 in the experiment, propagates circularly around the corresponding point of injection \vec{r}_1 , as sketched in Fig. 2.3 (a), if the current drain is in the infinite. Due to rotational symmetry, it is required that the injected current has no angular dependence. At an arbitrary point \vec{r} on the probed surface, the current is therefore distributed uniformly across a circumference $2\pi |\vec{r} - \vec{r}_1|$ such that the corresponding current density is given by

$$\vec{j}(\vec{r}) = \frac{I}{2\pi |\vec{r} - \vec{r}_1|^2} (\vec{r} - \vec{r}_1). \quad (2.3)$$

Using Eq. 2.2 in conjunction with the relation between the electric field and the potential Φ , one obtains

$$\vec{\nabla}\Phi(\vec{r}) = -\frac{I}{2\pi\sigma_{2D}} \frac{\vec{r} - \vec{r}_1}{|\vec{r} - \vec{r}_1|^2}, \quad (2.4)$$

which can be integrated along a curve $\vec{r}(t) : [0, 1] \rightarrow \mathcal{C}$ with $\vec{r}(0) = \vec{r}_0$ and $\vec{r}(1) = \vec{R}$

$$\Phi_1(\vec{R}) = -\frac{I}{2\pi\sigma_{2D}} \int_{\mathcal{C}} d\vec{r} \cdot \frac{\vec{r} - \vec{r}_1}{|\vec{r} - \vec{r}_1|^2} \quad (2.5)$$

to find the potential at an arbitrary point \vec{R} with respect to a reference point \vec{r}_0 . The considered geometry is visualized in Fig. 2.3 (b). The reference point is chosen to be on a connecting

line between the current source and the point \vec{R} such that $\vec{R} - \vec{r}_0 \parallel \vec{R} - \vec{r}_1$. Additionally, since Φ is a conservative potential and the integral therefore only depends on the starting and the end point, \mathcal{C} is chosen to be a straight line, resulting in $\vec{r}(t) = \vec{r}_0 + t(\vec{R} - \vec{r}_0)$. With this parametrization, the potential is then given by

$$\Phi_1(\vec{R}) = -\frac{I}{2\pi\sigma_{2D}} \int_0^1 dt \frac{d\vec{r}}{dt} \cdot \frac{\vec{r} - \vec{r}_1}{|\vec{r} - \vec{r}_1|^2} \quad (2.6)$$

$$= -\frac{I}{2\pi\sigma_{2D}} \int_0^1 dt (\vec{R} - \vec{r}_0) \cdot \frac{\vec{r} - \vec{r}_1}{|\vec{r} - \vec{r}_1|} \frac{1}{|\vec{r} - \vec{r}_1|} \quad (2.7)$$

$$= -\frac{I}{2\pi\sigma_{2D}} \int_0^1 dt |\vec{R} - \vec{r}_0| \frac{|\vec{R} - \vec{r}_0|}{|\vec{R} - \vec{r}_0|} \cdot \frac{\vec{r} - \vec{r}_1}{|\vec{r} - \vec{r}_1|} \frac{1}{|\vec{r} - \vec{r}_1|} \quad (2.8)$$

$$= -\frac{I}{2\pi\sigma_{2D}} \int_0^1 dt \frac{|\vec{R} - \vec{r}_0|}{|\vec{r} - \vec{r}_1|} \quad (2.9)$$

$$= -\frac{I}{2\pi\sigma_{2D}} \int_0^1 dt \frac{|\vec{R} - \vec{r}_0|}{|\vec{r}_0 + t(\vec{R} - \vec{r}_0) - \vec{r}_1|}. \quad (2.10)$$

A substitution according to $\vec{R}^\dagger = \vec{R} - \vec{r}_1$ and $\vec{r}_0^\dagger = \vec{r}_0 - \vec{r}_1$ allows the evaluation of the integral to

$$\Phi_1(\vec{R}) = -\frac{I}{2\pi\sigma_{2D}} \int_0^1 dt \frac{|\vec{R}^\dagger - \vec{r}_0^\dagger|}{|\vec{r}_0^\dagger + t(\vec{R}^\dagger - \vec{r}_0^\dagger)|} \quad (2.11)$$

$$= -\frac{I(R^\dagger - r_0^\dagger)}{2\pi\sigma_{2D}} \int_0^1 dt \frac{1}{r_0^\dagger + t(R^\dagger - r_0^\dagger)} \quad (2.12)$$

$$= -\frac{I}{2\pi\sigma_{2D}} \int_{r_0^\dagger}^{R^\dagger} du \frac{1}{u} \quad (2.13)$$

$$= -\frac{I}{2\pi\sigma_{2D}} \ln\left(\frac{R^\dagger}{r_0^\dagger}\right) = -\frac{I}{2\pi\sigma_{2D}} \ln\left(\frac{|\vec{R} - \vec{r}_1|}{r_0^\dagger}\right). \quad (2.14)$$

This solution for the potential distribution of a single point contact coincides with the related harmonic function obtained from solving Laplace's equation in two dimensions. In this single point expression, the potential still includes an open additive component depending on the choice of the open parameter \vec{r}_0 . This component is left over since the electric potential is well defined only with a reference. When potential differences are considered, the undetermined component is canceled.

To reproduce the situation of a current I_{14} flowing between two point contacts on the surface at \vec{r}_1 and \vec{r}_4 , the single-contact solution can be used in conjunction with the superposition

principle

$$\Phi_{14}(\vec{R}) = \Phi_1(\vec{R}) + \Phi_4(\vec{R}) \quad (2.15)$$

$$= -\frac{I_{14}}{2\pi\sigma_{2D}} \ln\left(\frac{|\vec{R} - \vec{r}_1|}{r_0^\dagger}\right) + \frac{I_{14}}{2\pi\sigma_{2D}} \ln\left(\frac{|\vec{R} - \vec{r}_4|}{r_0^\dagger}\right) \quad (2.16)$$

$$= \frac{I_{14}}{2\pi\sigma_{2D}} \left[\ln\left(\frac{|\vec{R} - \vec{r}_4|}{r_0^\dagger}\right) + \ln\left(\frac{r_0^\dagger}{|\vec{R} - \vec{r}_1|}\right) \right] \quad (2.17)$$

$$= \frac{I_{14}}{2\pi\sigma_{2D}} \ln\left(\frac{|\vec{R} - \vec{r}_4|}{|\vec{R} - \vec{r}_1|}\right) \quad (2.18)$$

where the same relative reference point r_0^\dagger is chosen for both tips such that both have a common reference potential.

The potential difference between two voltage probes which enters the four-point resistance in 2.1 is obtained by evaluating the potential distribution resulting from the two current-injecting point contacts at the locations of the voltage-probing tips \vec{r}_2 and \vec{r}_3

$$V_{23} = \Phi_{14}(\vec{r}_2) - \Phi_{14}(\vec{r}_3) \quad (2.19)$$

Consequently, the local four-point resistance for any configuration of the four tips on the surface of a 2D conductor is given by

$$R_{2D}^{4P}(\vec{r}_1, \vec{r}_2, \vec{r}_3, \vec{r}_4) = \frac{V_{23}}{I_{14}} = \frac{1}{2\pi\sigma_{2D}} \left[\ln\left(\frac{|\vec{r}_2 - \vec{r}_4|}{|\vec{r}_2 - \vec{r}_1|}\right) - \ln\left(\frac{|\vec{r}_3 - \vec{r}_4|}{|\vec{r}_3 - \vec{r}_1|}\right) \right]. \quad (2.20)$$

2.2.2. Three-dimensional conductivity

In the three-dimensional semi-infinite half space, the potential distribution corresponding to a current injection by point contacts is found analogously to the 2D case. As sketched in Fig. 2.4, the current injected by a point source at \vec{r}_1 on the surface propagates in a half-spherical shape in the 3D medium

$$\vec{j}(\vec{r}) = \frac{I}{2\pi|\vec{r} - \vec{r}_1|^3} (\vec{r} - \vec{r}_1), \quad (2.21)$$

which results in

$$\vec{\nabla}\Phi(\vec{r}) = -\frac{I}{2\pi\sigma_{3D}} \frac{\vec{r} - \vec{r}_1}{|\vec{r} - \vec{r}_1|^3}. \quad (2.22)$$

Integration of this term along the same curve $\mathcal{C} : \vec{r}(t) = \vec{r}_0 + t(\vec{R} - \vec{r}_0)$ that is defined in section 2.2.1 yields the potential distribution $\Phi_1(\vec{R})$ resulting from a single point contact with respect

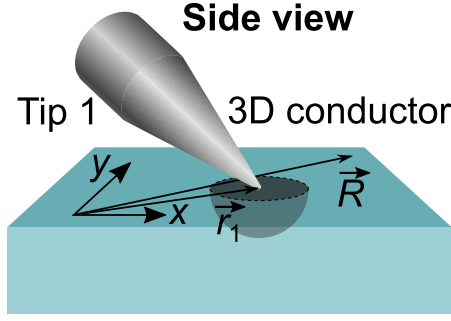


Fig. 2.4.: Conceptual sketch of current injection from a point-like contact in a 3D conductor. In three-dimensional isotropic systems, the current spreads in half-spherical shape from the point of injection. The corresponding electric potential is obtained by performing a line integral of the resulting current density.

to an arbitrary reference point \vec{r}_0

$$\Phi_1(\vec{R}) = -\frac{I}{2\pi\sigma_{3D}} \int_{\mathcal{V}} d\vec{r} \cdot \frac{\vec{r} - \vec{r}_1}{|\vec{r} - \vec{r}_1|^3} \quad (2.23)$$

$$= -\frac{I}{2\pi\sigma_{3D}} \int_0^1 dt |\vec{R} - \vec{r}_0| \frac{\vec{R} - \vec{r}_0}{|\vec{R} - \vec{r}_0|} \cdot \frac{\vec{r} - \vec{r}_1}{|\vec{r} - \vec{r}_1|} \frac{1}{|\vec{r} - \vec{r}_1|^2} \quad (2.24)$$

$$= -\frac{I}{2\pi\sigma_{3D}} \int_0^1 dt \frac{|\vec{R} - \vec{r}_0|}{|\vec{r}_0 + t(\vec{R} - \vec{r}_0) - \vec{r}_1|^2}. \quad (2.25)$$

In this case of three dimensions, \vec{R} and \vec{r}_0 can generally be points below the surface, such that $\Phi_1(\vec{R})$ is also valid in the interior of the 3D bulk. In the experiment, however, only points on the surface are accessible by the STM tips and relevant for the four-point resistance. After performing a translation of coordinates with $\vec{R}^\dagger = \vec{R} - \vec{r}_1$ and $\vec{r}_0^\dagger = \vec{r}_0 - \vec{r}_1$, the expression reduces to

$$\Phi_1(\vec{R}) = -\frac{I(R^\dagger - r_0^\dagger)}{2\pi\sigma_{3D}} \int_0^1 dt \frac{1}{[r_0^\dagger + t(R^\dagger - r_0^\dagger)]^2} \quad (2.26)$$

$$= -\frac{I}{2\pi\sigma_{3D}} \int_{r_0^\dagger}^{R^\dagger} du \frac{1}{u^2} \quad (2.27)$$

$$= \frac{I}{2\pi\sigma_{3D}} \left(\frac{1}{R^\dagger} - \frac{1}{r_0^\dagger} \right) = \frac{I}{2\pi\sigma_{3D}} \left(\frac{1}{|\vec{R} - \vec{r}_1|} - \frac{1}{r_0^\dagger} \right), \quad (2.28)$$

which is equal to the harmonic function denoting the 3D solution of Laplace's equation of a point-like singularity at \vec{r}_1 . Applying the superposition principle to the single-contact solution for the case of a current source (I_{14}) at \vec{r}_1 and a current sink ($-I_{14}$) at \vec{r}_4 yields the

potential distribution resulting from a current flow between two tips at the surface of a 3D bulk system

$$\Phi_{14}(\vec{R}) = \Phi_1(\vec{R}) + \Phi_4(\vec{R}) \quad (2.29)$$

$$= \frac{I_{14}}{2\pi\sigma_{3D}} \left(\frac{1}{|\vec{R} - \vec{r}_1|} - \frac{1}{r_0^\dagger} \right) - \frac{I_{14}}{2\pi\sigma_{3D}} \left(\frac{1}{|\vec{R} - \vec{r}_4|} - \frac{1}{r_0^\dagger} \right) \quad (2.30)$$

$$= \frac{I_{14}}{2\pi\sigma_{3D}} \left(\frac{1}{|\vec{R} - \vec{r}_1|} - \frac{1}{|\vec{R} - \vec{r}_4|} \right). \quad (2.31)$$

The local four-point resistance is ultimately obtained from the difference of the potential Φ_{14} at the locations \vec{r}_2 and \vec{r}_3 of the two voltage-probing tips

$$R_{3D}^{4P}(\vec{r}_1, \vec{r}_2, \vec{r}_3, \vec{r}_4) = \frac{\Phi_{14}(\vec{r}_2) - \Phi_{14}(\vec{r}_3)}{I_{14}} \quad (2.32)$$

$$= \frac{1}{2\pi\sigma_{3D}} \left(\frac{1}{|\vec{r}_2 - \vec{r}_1|} - \frac{1}{|\vec{r}_2 - \vec{r}_4|} - \frac{1}{|\vec{r}_3 - \vec{r}_1|} + \frac{1}{|\vec{r}_3 - \vec{r}_4|} \right). \quad (2.33)$$

2.2.3. Distance-dependent resistance measurement

With the derived expressions in Eq. 2.20 and Eq. 2.33, four-point resistances that are acquired in any configuration of tips can be related to the underlying conductivity of the sample, i.e. σ_{2D} and σ_{3D} , respectively. Furthermore, the different characteristic dependences of the resistance on tip distances in 2D and 3D can be exploited to find the dimensionality that the charge transport takes place in. To enhance the certainty of the conductivity determination, multiple resistance values are acquired at different tip positions in the experiment, which requires the tips to be moved in between. In doing so, it is convenient to use simple tip geometries to reduce the complexity of the position dependence of the resistance function.

The simplest tip geometry is a linear configuration with equal inter-tip distances s , as sketched in Fig. 2.5 (a) for an example with the current injected between the outer two tips, while the potential is probed by the inner pair. In this equidistant arrangement, the four-point resistance in the 2D case and 3D case is given by

$$R_{2D}^{4P} = \frac{1}{2\pi\sigma_{2D}} \left[\ln\left(\frac{2s}{s}\right) - \ln\left(\frac{s}{2s}\right) \right] \quad (2.34)$$

$$= \frac{1}{\pi\sigma_{2D}} \ln(2) \quad (2.35)$$

and

$$R_{3D}^{4P}(s) = \frac{1}{2\pi\sigma_{3D}} \left(\frac{1}{s} - \frac{1}{2s} - \frac{1}{2s} + \frac{1}{s} \right) \quad (2.36)$$

$$= \frac{1}{2\pi\sigma_{3D}s}, \quad (2.37)$$

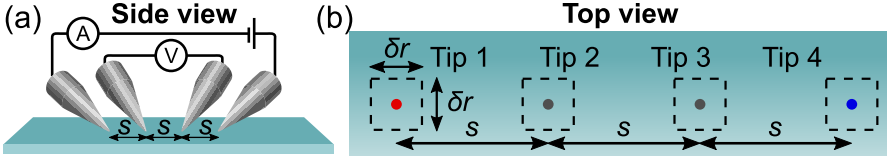


Fig. 2.5.: (a) Schematic representation of a linear four-point resistance measurement configuration with equal inter-tip distances s on the surface of a sample. Using this equidistant tip alignment significantly simplifies the spatial dependence of the four-point resistance in 2D and 3D systems. (b) When positioning the four tips with finite accuracy in the experiment, a position uncertainty δr can lead to a deviation of single resistance measurements from the model resistance $R^{4P}(s)$. This deviation can be estimated by including spatial variations in the general expressions given by Eq. 2.20 and Eq. 2.33.

respectively, which reduces the number of variables significantly. In particular, in the 2D case, the resistance does not depend on the inter-tip distance s in this arrangement, making it a hallmark of two-dimensional charge transport.

It is important to consider that, in the experiment, the distance s is determined from the four tip positions and as such is a quantity with finite accuracy. The influence of the positioning accuracy on the measured resistance can be estimated from a model including a deviation from the desired position for each tip, as sketched in Fig. 2.5 (b). The position of each tip is subject to an uncertainty δr in both directions of the surface plane. The actual tip positions are assumed to be uniformly distributed in a square spanned by δr around the desired location. Within these squares, there exists a set of tip positions corresponding to a maximum and minimum four-point resistance $R^{\max}(s)$ and $R^{\min}(s)$, respectively. As an estimate for the effect of the spatial uncertainty, the relative deviation of the four-point resistance as a function of δr is determined by

$$\delta R/R^{4P} = \frac{R^{\max}(s) - R^{\min}(s)}{R^{4P}}. \tag{2.38}$$

Including the uncertainty δr in the general resistance expressions in Eq. 2.20 and Eq. 2.33 leads to

$$\delta R_{2D}/R_{2D}^{4P} = \frac{1}{2\ln(2)} \ln\left(\frac{1+2\epsilon+2\epsilon^2}{1-2\epsilon+\epsilon^2}\right) \tag{2.39}$$

and

$$\delta R_{3D}/R_{3D}^{4P} = \frac{2}{1-\epsilon} - \frac{2}{\sqrt{(1+\epsilon)^2+\epsilon^2}} \tag{2.40}$$

for the 2D case and the 3D case, where $\epsilon = \delta r/s$ is the relative uncertainty of tip positions. The derivation of these terms can be found in the appendix A.1.

In the experiment, when the positioning of the tips is performed using the optical microscope for visual control, the accuracy of tip positions is limited by its resolution with $\delta r \approx 1 \mu\text{m}$. As a result, this means that in the equidistant configuration with $s < 20 \mu\text{m}$, the estimated relative error of single resistance measurements already exceeds 0.15 and 0.2 for the 2D case and the 3D case, respectively.

This example emphasizes the importance of performing multiple measurements at different distances for the determination of the conductivity. With a greater range of individual measurements, the influence of the error of single measurements arising from mispositioning on the determined conductivity is decreased. Furthermore, the influence of the uncertainty δr that is applying to all tips is reduced by using a non-equidistant linear tip configuration, where only one of the tips is moved from the initial equidistant alignment with inter-tip distances s . In this manner, only one tip suffers from the increased relative uncertainty at small distances, while the others remain stationary at larger spacing and thus smaller $\delta r/s$.

The majority of the results included in the following chapters was produced by measuring the resistance in a linear configuration with the position of one tip being varied.

2.2.4. Geometric constraints

The expressions derived in the previous sections describe the four-point resistance of an infinite 2D sheet and a semi-infinite 3D bulk conductor, respectively. Depending on geometric conditions, these analytic terms are good approximations for real systems with finite dimensions.

Insulating boundary

Deviations from the two infinite models can be observed if the system is interrupted in-plane by an insulating boundary, e.g. a physical limitation of the sample in width or length. Likewise, in case of a 3D conductor, deviations from the model function are caused in the same manner by an interruption of translational symmetry towards the sample interior, e.g. by a finite sample thickness. The effect of both factors is outlined in the following.

The influence of an insulating boundary on the spatial dependence of the electric potential is determined analytically for simple geometries by the method of mirror images [38]. In case of a planar insulating boundary perpendicular to the surface, as depicted in Fig. 2.6, Neumann boundary conditions are imposed on the electric potential, requiring $\frac{d\Phi(\vec{R})}{dx} = 0$ for $x = 0$. If current sources/sinks are introduced in the sample region at $x < 0$, the resulting

electric potential corresponding to the boundary value problem can be constructed from the individual free space solutions $\Phi_i(\vec{R})$ of Laplace's equation. The potential $\Phi(\vec{R})$ is found by including a mirror image with the same polarity across the boundary as the symmetry plane for each current-injecting tip. This method produces the required boundary condition, since $\frac{d\Phi(\vec{R})}{dx} \Big|_{x=0} = 0$ follows directly from $\Phi(\vec{R}) = \sum_i [\Phi_i(x, y) + \Phi_i(-x, y)]$.

With \vec{r}_5 and \vec{r}_6 being the positions of the two mirror images to the current-injecting tips \vec{r}_1 and \vec{r}_4 in a four-terminal setup, the four-point resistance is obtained after superposition analogously to Eq. 2.15 and 2.29 according to

$$\Phi(\vec{R}) = \Phi_1(\vec{R}) + \Phi_4(\vec{R}) + \Phi_5(\vec{R}) + \Phi_6(\vec{R}) \quad (2.41)$$

by the evaluation of the potential difference at the positions \vec{r}_2 and \vec{r}_3 of the two voltage-probing tips.

For an example of a linear tip configuration with equal inter-tip distances s parallel to the boundary at a distance L , as sketched in Fig. 2.6, this results in

$$R_{2D}(s, L) = R_{2D}^{4P}(\vec{r}_1, \vec{r}_2, \vec{r}_3, \vec{r}_4) + R_{2D}^{4P}(\vec{r}_5, \vec{r}_2, \vec{r}_3, \vec{r}_6) \quad (2.42)$$

$$= \frac{1}{\pi\sigma_{2D}} \ln \left(2 \frac{\sqrt{(2s)^2 + (2L)^2}}{\sqrt{s^2 + (2L)^2}} \right) \quad (2.43)$$

and

$$R_{3D}(s, L) = R_{3D}^{4P}(\vec{r}_1, \vec{r}_2, \vec{r}_3, \vec{r}_4) + R_{3D}^{4P}(\vec{r}_5, \vec{r}_2, \vec{r}_3, \vec{r}_6) \quad (2.44)$$

$$= \frac{1}{2\pi\sigma_{3D}} \left(\frac{1}{s} + \frac{2}{\sqrt{s^2 + (2L)^2}} - \frac{1}{\sqrt{s^2 + L^2}} \right) \quad (2.45)$$

for the 2D and the 3D case, respectively. In both cases, these expressions converge towards the terms corresponding to equidistant tip configurations in Eq. 2.35 and Eq. 2.37 with increasing lateral distance L to the boundary. As evident from a comparison, the existence of the insulating boundary in vicinity leads to an increase of the measured resistance, which is reasonable since the boundary acts as a constriction of the current density. The difference to the (semi-)infinite case can be analyzed by the factor s/L . For $s/L = 1$, the deviation of the measured resistance from the value that is expected without a boundary amounts to 25% in 2D and to 16% in 3D, while for $s/L < 0.5$, there is less than 10% (2D) and 4% (3D) of deviation from the (semi-)infinite model, making it a very good approximation.

Similarly to a lateral constriction of the system, the influence of a finite sample thickness t on the three-dimensional resistance can be modeled by applying the method of mirror

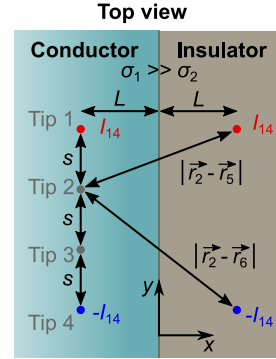


Fig. 2.6.: Sketch of the model used to determine the electrostatic influence of a planar insulating boundary perpendicular to the measured surface. The potential distribution corresponding to a parallel tip configuration at a distance L to the boundary is found by including virtual current sources with the same polarity at \vec{r}_5 and \vec{r}_6 across the boundary plane.

charges to the case of an insulating boundary plane parallel to the surface at a distance t . It is found that in case of $t/s > 3$, the finite sample thickness does not lead to deviations from the semi-infinite 3D bulk, while for smaller thicknesses, a continuous transition to 2D-like behavior takes place [38]. At $t/s < 0.4$, charge transport in the constricted system conforms to two-dimensional distance dependence. Therefore, in order to experimentally distinguish intrinsic 2D and 3D charge transport by the respective characteristic distance dependence, it is required that realized inter-tip distances are small enough to guarantee discernibility in principle.

Conducting boundary

On the contrary, a sample region can be interrupted by a conducting boundary, e.g. a junction to a neighboring region with greatly enhanced conductivity $\sigma_2 \gg \sigma_1$, as indicated in Fig. 2.7. In analogy to an insulating termination of the sample, the influence of such a conducting boundary on the electric potential can also be determined analytically for simple geometries. A planar conducting boundary perpendicular to the surface at $x = 0$, as sketched in Fig. 2.7, introduces Dirichlet boundary conditions to the electric potential with $\Phi(\vec{R}) = 0$ for $x = 0$. Again, using the method of mirror images, the solution $\Phi(\vec{R})$ of the boundary value problem corresponding to a set of current-injecting tips on the surface is obtained by superposition of the individual free space solutions $\Phi_i(\vec{R})$. For this purpose, a mirror image with opposite polarity is considered across the boundary for each current source/sink. The obtained solution $\Phi(\vec{R}) = \sum_i [\Phi_i(x, y) - \Phi_i(-x, y)]$ satisfies the boundary condition $\Phi(\vec{R})|_{x=0} = 0$ by default.

For two current injecting tips at \vec{r}_1, \vec{r}_4 and their respective mirror images at \vec{r}_5, \vec{r}_6 , the four-point resistance is determined from the potential difference of the superimposed expression

$$\Phi(\vec{R}) = \Phi_1(\vec{R}) + \Phi_4(\vec{R}) - \Phi_5(\vec{R}) - \Phi_6(\vec{R}) \quad (2.46)$$

at the voltage probe positions \vec{r}_2 and \vec{r}_3 .

In case of a linear equidistant four-point configuration parallel to the boundary at a lateral

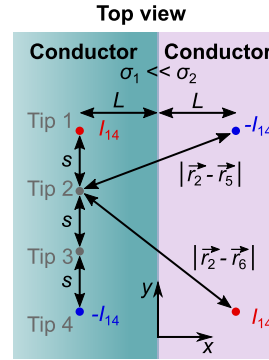


Fig. 2.7.: Sketch of the model used to determine the electrostatic influence of a planar conducting boundary perpendicular to the measured surface. The potential distribution corresponding to a parallel tip configuration at a distance L to the boundary is found by including virtual current sources with opposite polarity at \vec{r}_5 and \vec{r}_6 across the boundary plane.

distance L , as depicted in Fig. 2.7, the measured resistance yields

$$R_{2D}(s, L) = R_{2D}^{4P}(\vec{r}_1, \vec{r}_2, \vec{r}_3, \vec{r}_4) - R_{2D}^{4P}(\vec{r}_5, \vec{r}_2, \vec{r}_3, \vec{r}_6) \quad (2.47)$$

$$= \frac{1}{\pi\sigma_{2D}} \ln \left(2 \frac{\sqrt{s^2 + (2L)^2}}{\sqrt{(2s)^2 + (2L)^2}} \right) \quad (2.48)$$

and

$$R_{3D}(s, L) = R_{3D}^{4P}(\vec{r}_1, \vec{r}_2, \vec{r}_3, \vec{r}_4) - R_{3D}^{4P}(\vec{r}_5, \vec{r}_2, \vec{r}_3, \vec{r}_6) \quad (2.49)$$

$$= \frac{1}{2\pi\sigma_{3D}} \left(\frac{1}{s} - \frac{2}{\sqrt{s^2 + (2L)^2}} + \frac{1}{\sqrt{s^2 + L^2}} \right) \quad (2.50)$$

for the 2D and the 3D case, respectively. In the limit of $L \rightarrow \infty$, the (semi-)infinite case as described by Eq. 2.35 and Eq. 2.37 is retained.

2.3. Example measurements on SrTiO₃

In the previous sections, analytic expressions were presented that allow the ascription of measured four-point resistances to the underlying conductivity of the system depending on its dimensionality. The following sections present exemplary distance-dependent resistance measurements performed with a multi-tip STM on strontium titanate (SrTiO₃). This material is a suitable system to demonstrate the occurrence of charge transport in different dimensions, since a characteristic transition between a 2D and a 3D regime takes place depending on the *in situ* preparation of the sample in-between measurements. Using the four-point measurement technique, it is possible to characterize the changing conductivity profile in this system.

2.3.1. SrTiO₃ material system

Strontium titanate (SrTiO₃) is a ternary transition metal oxide in a perovskite structure as depicted in Fig. 2.8 with unique electronic properties. In its stoichiometric form, this system is a band insulator with a band gap of ~ 3.2 eV [39, 40], whereas as a consequence of an introduction of oxygen vacancies in the system, the material undergoes a transformation to a metal [41]. Over the course of this reduction process, the initial valence state of the transition metal cation Ti in the compound changes from +4 to +3 due to charge compensation [42]. This valence change mechanism makes SrTiO₃ an suitable material for application in memristive devices which can potentially find use in the fields of energy-efficient data storage and neuromorphic computing [43].

The influence of oxygen vacancies on the electronic structure of SrTiO₃ is explained microscopically. As oxygen is removed from the system, electrons are left behind and the system

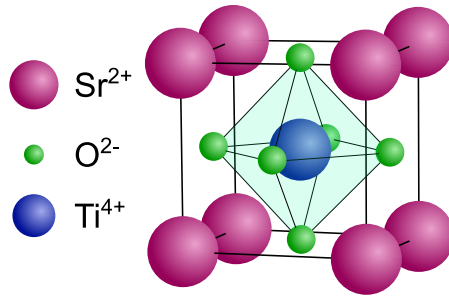


Fig. 2.8.: Cubic unit cell of stoichiometric SrTiO₃. The material compound is ordered in a perovskite crystal structure with a Ti cation sitting in the center surrounded by cationic Sr and anionic O atoms.

is effectively being n-doped. This process is formalized in the Kroeger-Vink notation as $O_O \rightarrow V_O^{\cdot\cdot} + 2e^- + \frac{1}{2}O_2$, where the subscript denotes that the respective entity is situated at an oxygen lattice site. Following a consequential distribution in the t_{2g} orbitals of Ti atoms in the crystal, these residual d -electrons can participate in charge transport [41, 44–47].

One way of realizing the insulator-metal transition of transparent conducting oxides such as SrTiO₃ is reduction by means of thermal treatment at low oxygen partial pressure. Under this condition, oxygen vacancies are generated as oxygen effuses from the material at elevated sample temperature. In macroscopic resistance measurements, it has been shown that metallic behavior in SrTiO₃ starts to emerge after treatment at $T \approx 800^\circ\text{C}$ [47, 48]. In general, the macroscopic conductivity of the material increases with higher temperatures, as more oxygen vacancies are generated due to stronger reduction conditions. In the past, SrTiO₃ has also been studied by single-tip STM [49, 50], demonstrating that the surface structure undergoes various forms of transformations after reduction.

While it is clear that the macroscopically observable conductivity is increased with chemical reduction, the microscopic details of this process and the question how it is tied to structural properties is not trivial. In this regard, a multi-tip STM proves to be a helpful tool, since its ability to access charge transport properties locally can be exploited to investigate the conductivity profile of SrTiO₃ at different stages of reduction. Using *in situ* distance-dependent four-point measurements as outlined in the previous sections, the electronic transport properties of a SrTiO₃ sample are investigated on the microscale. It turns out that slight reduction at comparatively lower temperatures initially results in charge transport that resembles that of a 2D conducting sheet in the surface region. After higher reduction temperature, it is found that apart from increasing by several orders of magnitude, the charge transport behavior changes to appear as three-dimensional. In the intermediate stage of thermal annealing, a complex transport regime exhibiting a mixture of 2D/3D behavior is observed. Using analyti-

cal tools, it is possible to extract the underlying specific conductivity profile resulting from reduction.

2.3.2. Experimental procedure

The sample that was used in the experiment is an epi-polished Verneuil-grown SrTiO₃(100) single crystal available from CrysTec (Berlin) with dimensions of $3 \times 6 \times 0.5 \text{ mm}^3$. Every step of the experiment is performed in the same UHV system without breaking vacuum conditions, which is essential for the experiment since an exposure to air subsequent to reduction otherwise results in immediate reoxidation of the sample.

The evolution of electrical properties of the SrTiO₃ sample after increasing reduction is investigated by means of four-point measurements using the STM tips in linear configuration on the sample surface. For this purpose, distance-dependent resistance measurements are performed at room temperature in between five successive stages of reduction. The steps of the experimental procedure is sketched in Fig. 2.9. The sample is reduced thermally by means of resistive current heating in UHV conditions. During this process, the sample temperature is monitored on the surface using a pyrometer. Since the application of a DC current leads to undesired stoichiometry polarization in the ternary system as a consequence of electrodegradation from the applied field [51], which ultimately affects the electrical properties, it is essential to use an AC current as a means of annealing. Therefore, a 100 Hz AC current is applied using macroscopic contacts during thermal treatment. For each of the annealing steps, the sample is heated up slowly before maintaining it at the target temperature for a duration of 60 min. The pressure of $p < 10^{-9}$ mbar in the UHV system during annealing guarantees reducing conditions. After the successful annealing process, the sample is carefully cooled down to room temperature at a rate of $\sim 50^\circ\text{C}/\text{min}$ and transferred immediately into the STM. The five investigated stages of reduction in between electrical measurements with increasing intensity correspond to a thermal treatment in this manner with constant target temperatures between 600°C and 1000°C in steps of 100°C .

With the SrTiO₃ sample cooled down to room temperature and inserted into the STM subsequent to a reduction step, the STM tips are approached to the sample and positioned on its surface in a linear configuration on the microscale. Using the piezoelement controlling z-movement manually, the tips are each gently moved from tunnelling contact towards the surface to establish ohmic contact. The successful contacting procedure is confirmed by a sudden increase of current between the respective biased tip and the grounded sample. Apart from the equidistant tip arrangement with varied inter-tip distances $s \geq 16 \mu\text{m}$, as outlined in section 2.2.3, a non-equidistant configuration with a distance x between one of

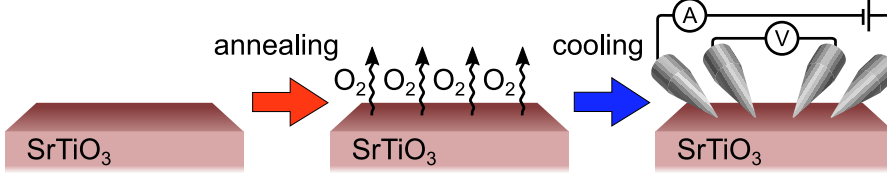


Fig. 2.9.: Schematic representation of the experimental procedure. The SrTiO₃ sample is subjected to reducing conditions by means of resistive heating in UHV. As oxygen effuses from the sample and leaves behind oxygen vacancies acting as dopants, the electronic structure of the sample changes for as long as reoxidation is prevented. After the reduction process, the sample is inserted into the 4-tip STM in the same UHV system, such that four-point resistance measurements can be performed *in situ*.

the current-injecting tips and its neighboring voltage probe is used. In this configuration, only x is varied by moving the respective current-injecting tip, while the other tips remain at fixed positions at $s = 16\mu\text{m} > x$. Using the general position-dependent resistance terms in Eq. 2.20 and Eq. 2.33, the four-point resistance of an infinite 2D sheet and a semi-infinite 3D bulk medium corresponding to this arrangement is given by

$$R_{2D}(x, s) = \frac{1}{2\pi\sigma_{2D}} \left[\ln\left(\frac{2s}{x}\right) + \ln\left(\frac{s+x}{s}\right) \right] \quad (2.51)$$

and

$$R_{3D}(x, s) = \frac{1}{2\pi\sigma_{3D}} \left[\frac{1}{x} + \frac{1}{2s} - \frac{1}{s+x} \right], \quad (2.52)$$

respectively. In between single resistance measurements, the appropriate tips are lifted from ohmic contact before being moved to the next position. All distances between the tips are determined from the optical microscope, as seen exemplary in the upper inset of Fig. 2.10 (a).

By exploiting the different characteristic distance-dependence of Eq. 2.51 and Eq. 2.52, it is possible to determine the dimensionality of the occurring charge transport in the sample.

2.3.3. Evolution of conductivity after thermal reduction

The evolution of the four-point resistance obtained from the same equidistant tip arrangement with $x = s = 16\mu\text{m}$ after each reduction step is presented in Fig. 2.10 (a). From the comparison, the measured absolute resistance appears to follow an exponentially decreasing trend with increasing reduction temperature with the exception of the result obtained after annealing at $T = 700^\circ\text{C}$. As confirmed by a repeated measurement on a separate sample, the result corresponding to reduction at $T = 700^\circ\text{C}$ is reproducible. It should further be noted that prior to any thermal treatment, four-point measurements do not yield any reasonable

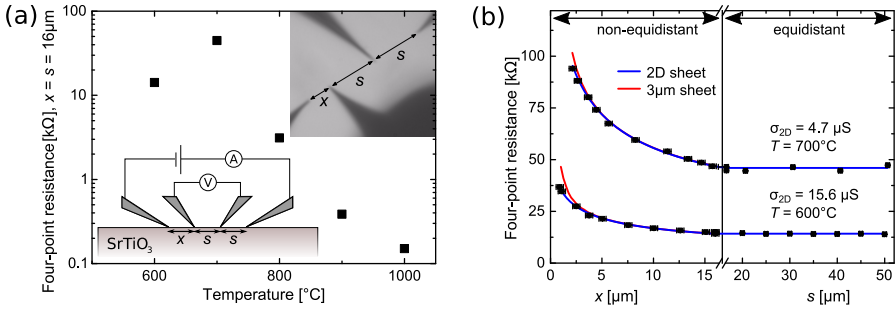


Fig. 2.10.: (a) Logarithmically scaled comparison of four-point resistance results obtained in the same linear tip configuration with $x = s = 16\mu\text{m}$ after thermal treatment at different target temperatures. With exception of the result corresponding to annealing at $T = 700^\circ\text{C}$, resistances measured in the same geometry show monotonously decreasing behavior with increasing intensity of reduction. An exemplary tip arrangement in a linear configuration with $x = 8\mu\text{m}$ and $s = 16\mu\text{m}$ is shown in the upper inset. A generalized depiction of the measurement configuration as seen from the side is also presented schematically in the lower inset. (b) Four-point resistance results of the $\text{SrTiO}_3(100)$ sample subsequent to reduction at $T = 600^\circ\text{C}$ and $T = 700^\circ\text{C}$ measured at different inter-tip distances s and x at room temperature. Being displayed on the right side of the axis break, results from an equidistant tip configuration are obtained upon varying s . In the non-equidistant configuration, x is varied, while the remaining tip distances are kept constant at $16\mu\text{m}$. For both configurations, the appropriate distance-dependent 2D model function given by Eq. 2.51 is used to explain the data, as indicated by the blue curves. To demonstrate deviations from pure 2D transport at small tip distances x , the simulated resistance of a $3\mu\text{m}$ thick sheet with corresponding conductivity is featured as red curves.

results due to the highly insulating behavior of the unreduced SrTiO_3 sample. Over the course of subsequent annealing steps, the initially insulating sample transforms into a conducting medium, confirming the results of macroscopic resistance measurements [47, 48].

2.3.3.1. Slight reduction

The detailed results of distance-dependent measurements after annealing at $T = 600^\circ\text{C}$ and $T = 700^\circ\text{C}$ are shown in Fig. 2.10 (b). Separated by an axis break, the graph features four-point resistance values obtained in both linear configurations with varying inter-tip distances x and s . As evident from the correspondence with the blue curves in both regions, the resistance data is explained by the 2D conductivity model in Eq. 2.35 and Eq. 2.51. The agreement is particularly clear in the set of equidistant resistance measurements due to the constant resistance, which is a hallmark of 2D charge transport. From the fits of the underlying model functions to the measured data, the sheet conductivities corresponding to the two stages of

reduction are determined to $\sigma_{600^\circ\text{C}} = (15.6 \pm 0.2)\mu\text{S}$ and $\sigma_{700^\circ\text{C}} = (4.42 \pm 0.03)\mu\text{S}$, respectively.

The conductivity values obtained from these measurements on the micrometer scale are to be understood quantitatively as in-plane averages, since the used model presupposes an isotropic 2D conductivity. On the nanometer scale, however, local conductivity atomic force microscopy (LC-AFM) reveals small spots with strongly enhanced conductivity on an otherwise insulating surface [52, 53]. This observation suggests that the conductivity constituting the 2D transport behavior witnessed in the experiment is inhomogeneously distributed on the surface.

As discussed in section 2.2.4, depending on the thickness of the respective medium compared to the inter-tip distances of the measurement configuration, a 3D conductivity can in principle appear as two-dimensional due to the spatial confinement of the current lines. Using this insight, it is possible to find a limit for the thickness for the conducting region below the surface of the SrTiO₃ sample after reduction at $T = 600^\circ\text{C}$ and $T = 700^\circ\text{C}$. In order to estimate the maximum thickness of the conducting region exhibiting 2D behavior, a simulation of the four-point resistance of a layer with finite thickness is performed and compared to the experimental data.

For this purpose, the solution of Laplace's equation for a region of specific thickness with an isotropic 3D conductivity corresponding to the experimental result on top of an insulating semi-infinite bulk [54] is determined. At small distances x in the non-equidistant configuration, the first deviations of the simulated results from the measured resistance values appear for calculations with a thickness of $t \geq 3\mu\text{m}$, as seen from the red curve in Fig. 2.10 (b). This means that, in the particular tip configuration used in the experiment, only for $t \leq 3\mu\text{m}$, charge transport occurring in a finite layer is indistinguishable from true 2D transport. Therefore, it is deduced that the observed conductivity in the SrTiO₃ sample at this stage of reduction is spatially limited to $3\mu\text{m}$ below the surface at most.

The spatial confinement of conductivity to the surface after slight reduction at 600°C and 700°C is explained by the mechanism of oxygen vacancy generation. When subjected to thermal treatment at reducing conditions, oxygen vacancies are introduced into the sample system. However, these vacancies do not form in a uniform manner through the sample interior, but are preferentially generated at dislocation cores due to a locally lower activation energy [55]. Furthermore, it is known theoretically [56, 57] and experimentally [58], that generated oxygen vacancies tend to be clustered in a linear manner. Since the investigated SrTiO₃ sample was subject to mechanical polishing as part of the surface preparation procedure, it is expected to host a high density of dislocations concentrated at the surface [59]. Therefore, it is suggested that the observed confinement of conductivity after slight reduction is a result of conducting paths constituted by oxygen vacancies at dislocations close to the

surface [48].

It is clear that such an ordered manner of vacancy formation must inevitably exist, since the amount of effusing oxygen during thermal reduction of SrTiO₃, as measured by mass spectrometry [60], is too low to satisfy the Mott criterion, which needs to be fulfilled to explain a macroscopic conductivity by a diluted distribution of conducting sites across the sample interior. The correlation of nanoscopic local enhancement of conductivity at the surface of reduced SrTiO₃ with dislocation sites is suggested by LC-AFM investigations combined with anisotropic etching [43]. This suggested relation is further supported by the observation of localized conductivity close to the bicrystal boundary of reduced SrTiO₃ bicrystals via LC-AFM [60].

Apart from the existence of dislocations at the surface, the suspected tendency of oxygen vacancies to form at the surface is enhanced by the fact that the respective formation energy is lower for surface vacancies compared to the bulk interior [61]. This circumstance is expected to be particularly influential at lower annealing temperatures ($T \leq 700^\circ\text{C}$), which supports the measured four-point resistance data.

The assumption of the measured 2D conductivity being an average in-plane quantity constituted by a network of conducting paths raises the question how point-like electrodes such as the utilized STM tips placed on the surface can form an electrical connection. In LC-AFM studies [52, 53], the terminating points of the conductive paths on the SrTiO₃(100) surface appear as inhomogeneously distributed nanoscale areas of enhanced conductivity within an insulating medium. The respective density of conductive spots on the surface is estimated to 10^{11} cm^{-2} . Following this density and estimating the curvature radius of an STM tip as $r_{\text{tip}} \approx 25 \text{ nm}$, a contact area of πr_{tip}^2 covers an average of two conductive spots upon contact with the surface. By pushing the STM tip further into the surface, the contact area can be even large due to deformations. For this reason, the inhomogeneous distribution of connections to the conducting network on the surface is not detrimental regarding the establishment of electrical contact.

2.3.3.2. Strong reduction

Detailed results of distance-dependent measurements after strong reduction at $T = 900^\circ\text{C}$ and $T = 1000^\circ\text{C}$ are presented in Fig. 2.11 (a), with the axis break separating the two used linear configurations. As seen from the agreement with the red curves representing a fit of Eq. 2.52, the obtained four-point resistance exhibits 3D transport behavior. The 3D conductivities corresponding to the best fits are determined to $\sigma_{900^\circ\text{C}} = (23.9 \pm 0.5) \text{ S/m}$ and $\sigma_{1000^\circ\text{C}} = (69.3 \pm 0.4) \text{ S/m}$, respectively. Analogous to the 2D case after slight reduction, a

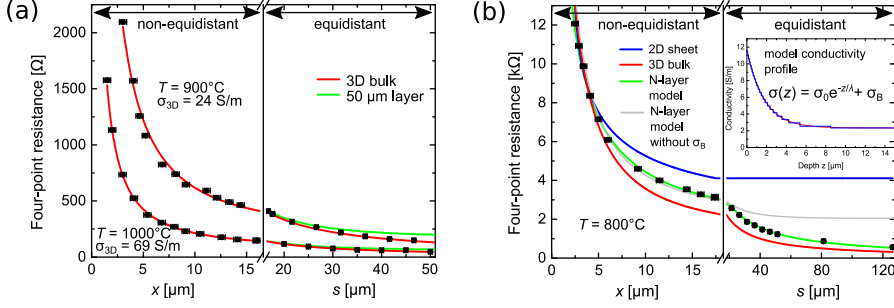


Fig. 2.11.: (a) Distance-dependent four-point resistance of the SrTiO₃(100) sample measured at room temperature after reduction at $T = 900^\circ\text{C}$ and $T = 1000^\circ\text{C}$. Being separated by the axis break, results from equidistant as well as non-equidistant arrangements are presented, where in the non-equidistant arrangement, s is kept constant at $16\mu\text{m}$. The distance-dependent 3D model function given by Eq. 2.52 explains the entirety of the resistance data, as evident from the corresponding fits being illustrated by red curves. Additionally, the simulated resistance of a $50\mu\text{m}$ thick layer with the same 3D conductivity as obtained from the fit is represented by the green curves. Since deviations of the simulation from the pure 3D model are observed up to this thickness, it is suggested that the conducting region in the SrTiO₃ sample extends to at least $50\mu\text{m}$ below the surface. (b) Distance-dependent four-point resistance of the SrTiO₃ sample in the equidistant and non-equidistant configuration after thermal treatment at $T = 800^\circ\text{C}$. Exemplary 2D and 3D resistance functions chosen to fit the data at small distances x are denoted by blue and red curves, respectively. Due to mixed conductivity contributions, neither model can explain the entirety of the data. Represented by the green curve, a fit of the N-layer model with $N = 25$ is used to describe the data set. The corresponding conductivity profile of the sample and its discretization into the 25 segments used as the model input are shown in the inset. As evident from the grey curve, an N-layer model fit assuming a purely exponential decay of conductivity without a constant bulk component does not agree with the measurement results.

minimum thickness of the observed three-dimensional conducting region can be determined by comparison to the simulated resistance of a conducting layer with finite thickness. It is found that for the used inter-tip distances, deviations of simulated results from the half-infinite 3D model are obtained up to thicknesses of $50\mu\text{m}$. The corresponding four-point resistance is illustrated by the green curves in Fig 2.11 (a). For larger layer thicknesses, it is not possible to distinguish between infinitely extending and confined conductivity from the experimental data. Therefore, it is concluded that the observed conducting region after strong reduction of SrTiO₃ extends beyond a depth of $50\mu\text{m}$ below the surface.

It should further be noted that even at high temperature reduction, the concentration of the vacancies constituting conducting sites in SrTiO₃ is still too low to satisfy the Mott criterion [60]. This implies that the 3D conductivity inferred from the resistance data is understood as an in-plane average of the nanoscale conducting network.

The emerging 3D transport behavior observed after strong reduction is consistent with the mechanism of oxygen vacancy generation. As a consequence of the thermal energy at high temperature treatment, oxygen vacancies are formed even in the interior of the sample beyond the dislocations at the surface. The high temperature furthermore facilitates the diffusion of vacancies from the dislocations into the bulk of the material [62]. Therefore, a bulk conductivity surpassing the surface contribution is constituted by an increasingly dominant continuum of conducting sites.

2.3.3.3. Intermediate reduction

Distance-dependent resistance data obtained after intermediate reduction at $T = 800^\circ\text{C}$ is presented in Fig. 2.11 (b). The blue and the red curve denote 2D and 3D resistance model functions according to Eq. 2.51 and Eq. 2.52 chosen to agree with the data at small tip distances. As evident from their disagreement with the data, the sample cannot be understood as a singular isotropic 2D or 3D system and instead, a mixed transport regime has to be considered. To take mixed 2D/3D conduction contributions into account, the resistance data obtained after intermediate reduction is explained using an analytical N -layer conductance model [54, 63].

In principle, mixed conductivity contributions can be described as a first approximation within a circuit model including a 2D and a 3D channel in parallel. The underlying distribution of conductivity in the present sample, however, is expected to be more complex than a strictly parallel connection and requires a detailed description. The data is instead explained by determining the four-point resistance from an anisotropic conductivity distribution $\sigma(z)$ in the sample interior. At a given depth below the surface z , the obtained conductivity is assumed to be isotropic in-plane.

A known conductivity profile as a continuous function $\sigma(z)$ can be discretized into a step function of N segments with isotropic conductivity, such that Laplace's equation can be solved analytically for each of the segments using the resulting $2N + 1$ boundary conditions. With the obtained solutions of the electric potential, a four-point resistance corresponding to the tip configuration of the experiment can be determined [54]. In order to derive an expression for the resistance to compare with the experimental data, a model for the conductivity profile $\sigma(z)$ needs to be assumed. As the in-plane average conductivity is expected to follow the density of dislocations in the sample, which is shown to be exponentially decreasing towards the interior [43, 64], a corresponding exponential conductivity profile

$$\sigma(z) = \sigma_0 \cdot e^{-z/\lambda}, \quad (2.53)$$

is assumed as a first approach, where σ_0 and λ denote the unknown parameters of the model. It is emphasized that, although modeled as a depth-dependent quantity that is isotropic in-plane, the planar distribution of conducting regions on the nanoscale is expected to be inhomogeneous in the reduced sample. The expected distribution of conducting regions in the sample and the corresponding assumed in-plane conductivity profile $\sigma(z)$ are shown schematically in Fig. 2.12 (a).

A calculated fit to the experimental data with $N = 25$ based on the model conductivity in Eq. 2.53 is included as a grey curve in Fig. 2.11 (b). While following the general trend of the data, the calculation according to this model fails to reproduce the four-point resistance at all tip distances. The disagreement to the experimental results is particularly apparent at large tip distances, where the four-point measurement method is more sensitive to charge transport deeper in the interior [65]. As the resistance is overestimated in the assumed model, an unconsidered transport contribution in the sample interior is present and needs to be incorporated to satisfy the data. A comparison to quantitative investigations of the dislocation distribution in SrTiO₃ in literature substantiates this assumption. The exponential decay of the dislocation density is found to be primarily evident in the first few micrometers below the surface [48, 59, 64]. According to the model in Eq. 2.53, such a steep decrease of conductivity would lead to an exhibition of 2D behavior at distances in the order of $s \approx 20\mu\text{m}$, resulting in a larger deviation from the measured four-point resistance than the one obtained from the fit in Fig. 2.11 (b). In transmission electron microscopy measurements of a cut SrTiO₃ surface, it is demonstrated that instead of converging to zero, the dislocation density saturates to a constant level after $\sim 10\mu\text{m}$ of depth [64]. Based on this realization, the conductivity profile model $\sigma(z)$ is expanded by a corresponding constant bulk component σ_B in the sample interior.

As indicated by the green curve in Fig. 2.11 (b), the result from this extended model with $N = 25$ segments is in good correspondence with the entirety of the measured resistance data. The bulk conductivity $\sigma_B = (2.34 \pm 0.01) \text{ S/m}$, the initial conductivity $\sigma_0 = (9.3 \pm 0.2) \text{ S/m}$ and the decay length $\lambda = (1.75 \pm 0.04) \mu\text{m}$ as the three parameters of the underlying conductivity profile are determined from the best fit to the data. The corresponding conductivity profile $\sigma(z)$ and the according discrete step function used as the input for the N-layer model are presented in the inset of Fig. 2.11 (b). The determined decay length λ , which according to the mechanism of oxygen generation is interpreted to correspond to the near-surface exponential decay of the dislocation density, agrees well with quantitative results from literature [48, 59, 64]. Also, a surface investigation on a cross-sectional cut of a reduced SrTiO₃ crystal by LC-AFM reveals a map of locally enhanced conductivity that quantitatively coincides with the reconstructed conductivity profile $\sigma(z)$ [60].

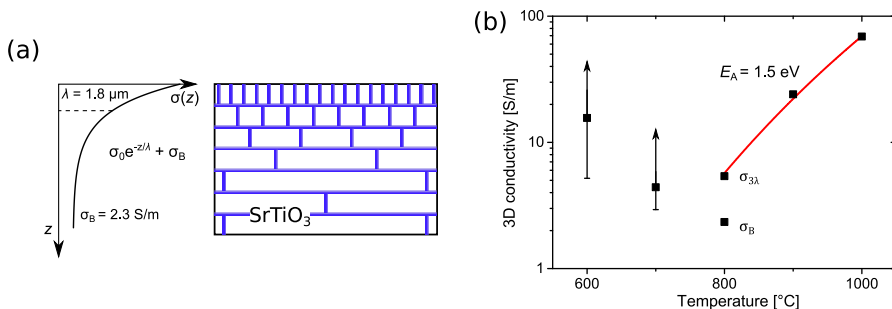


Fig. 2.12.: (a) Crosssectional sketch of the assumed distribution of conducting sites in the SrTiO₃ crystal after intermediate reduction at $T = 800^{\circ}\text{C}$ including the corresponding assumed in-plane average conductivity profile. As oxygen effuses from the sample due to thermal reduction, corresponding vacancies form in the sample and enhance the conductivity locally. Being the energetically preferred option, oxygen vacancies primarily form at dislocation cores and therefore establish a network of conducting filaments along the hierarchical distribution of dislocations at the surface [43]. The resulting conductivity profile $\sigma(z)$ is understood as a saturating exponential decay of average in-plane conductivity. (b) Overview of the experimentally obtained conductivity of the SrTiO₃ sample after different stages of thermal reduction. To enable the comparison, the 2D conductivity values resulting from slight reduction at $T \leq 700^{\circ}\text{C}$ are converted to corresponding 3D conductivity values assuming a finite layer thickness of $1\ \mu\text{m}$. Since the maximum sheet thickness is known to be $3\ \mu\text{m}$ from the simulation shown in Fig. 2.10 (b), a lower limit can be determined for both data points. With the minimum sheet thickness being unknown, however, the respective upper boundary for the conductivity cannot be determined. For $T = 800^{\circ}\text{C}$, where mixed 2D/3D contributions are observed in the form of a conductivity profile, the constant bulk component σ_B as well as an average 3D value $\sigma_{3\lambda}$ obtained from integration up to 3λ below the surface are presented.

Figure 2.12 (b) presents an overview of the obtained conductivity values corresponding to all investigated stages of reduction in SrTiO₃. To enable the direct quantitative comparison, the 2D conductivity values resulting from slight reduction at $T = 600^{\circ}\text{C}$ and $T = 700^{\circ}\text{C}$ are converted to 3D conductivities assuming a confinement to a finite layer of $1\ \mu\text{m}$ thickness. As evident from the simulation results presented in Fig. 2.10 (b), charge transport after slight reduction is extended to a maximum depth of $3\ \mu\text{m}$ below the surface. It is therefore possible to determine a lower limit of the converted 3D conductivity values, which is denoted by the bars in Fig. 2.12 (b). However, it is not possible to determine an upper conductivity limit due to the unknown actual layer thickness. To compare the conductivity resulting from reduction at $T = 800^{\circ}\text{C}$ explicitly, two values obtained from the conductivity profile containing mixed 2D/3D contributions are displayed separately in Fig. 2.12 (b). Apart from the additive 3D bulk component σ_B from the sample interior, the average 3D conductivity in the region of exponential decay $\sigma_{3\lambda}$ is determined from an integration of the continuous conductivity

profile. It is emphasized that even after strong reduction, conductivity in the interior might be confined to a finite depth, even though it is denoted as three-dimensional. With the inter-tip distances used in the experiment, the analysis depth of the four-point method is restricted to $\sim 100\mu\text{m}$.

As evident from the comparison in Fig. 2.12 (b), a general trend of increasing conductivity is observed for increasing annealing temperatures $T \geq 800^\circ\text{C}$, which is interpreted to be due to an increasing amount of generated oxygen vacancies. In case of lower temperatures $T = 600^\circ\text{C}$ and $T = 700^\circ\text{C}$, an opposite trend is observed. This unintuitive trend of decreasing conductivity is not seen in macroscopic resistance measurements. Therefore, it appears reasonable that the measured effect is related to surface properties of the sample due to the surface-sensitive nature of the four-point STM method. One possible explanation is the influence of contaminations on the surface introduced during storage and sample preparation by the manufacturer in ambient conditions. Therefore, the conductivities obtained after slight reduction up to 800°C are not understood to be an intrinsic material property. Additionally, carbon contaminants at the sample surface can dissolve at 700°C according to $\text{CO}_2 \rightarrow \text{CO} + \frac{1}{2}\text{O}_2$, as shown in XPS measurements [53, 66]. The produced oxygen can either effuse or integrate into the crystal. An indication of this effect is found by an abrupt decrease of oxygen effusion rate during thermal reduction between 700°C and 800°C [60]. It is therefore expected that a portion of the produced oxygen below 800°C is also incorporated into the sample, which effectively results in a decrease in conductivity in surface-sensitive measurements. The decrease of conductivity at 700°C might also be facilitated by a rearrangement or annihilation of dislocations during thermal treatment, which leads to a redistribution of the conductivity-enhancing oxygen vacancies.

With more thermal energy provided during reduction at higher annealing temperatures, the counteracting effect on the conductivity due to contaminants is surpassed as oxygen vacancies are increasingly generated beyond the dislocations. As illustrated in Fig. 2.12 (b), this is substantiated by the observed Arrhenius behavior of the conductivity between 800°C and 1000°C , with a corresponding activation energy of $E_A = (1.5 \pm 0.2)\text{ eV}$.

The non-monotonous evolution of conductivity with increasing annealing temperature is therefore explained by two counteracting processes. Overall, it is evident that SrTiO₃ changes its electrical properties drastically after thermal reduction. Apart from the known characteristic insulator-metal transition of the material, the system additionally undergoes a continuous transition from 2D to 3D charge transport due to the changing manner of oxygen vacancy generation. While the preferential formation of vacancies at dislocations concentrated at the surface results in a 2D conductivity at lower temperatures, a 3D conductivity is established at higher temperatures due to enabled vacancy generation in the interior of the material. After

reduction at intermediate temperatures, a transport regime with mixed 2D/3D transport characteristics, which are resolvable by the four-point STM technique.

2.4. Summary

In this chapter, the four-point resistance measurement principle, as well as the theoretical foundation to the measurement technique have been introduced. The fundamental expressions relating the measured resistance in any possible configuration of probes to the underlying conductivity of two-dimensional and three-dimensional systems were derived. Also, the limitations of these derived models due to geometric constraints in real sample systems were discussed.

The fundamental technique of distance-dependent four-point resistance measurements was demonstrated on the suitable example system of SrTiO₃. Using this material, the characteristic appearances of 2D and 3D charge transport behavior, as well as their continuous transition were explored in comparable measurement configurations on the same sample. Furthermore, it was shown that, even in transport regimes with mixed dimensionality contributions, it is possible to resolve different transport components quantitatively.

As already evident from this example system, it is not possible to resolve effects caused by sample properties on the nanoscale using resistance measurements in configurations with inter-tip distances on the scale of several micrometers. In order to access four-point resistances on the nanometer scale, controlled tip movement beyond the resolution of the optical microscope is required. In the next chapter, a positioning method based on STM scans with each tip is presented, which allows to realize more compact measurement arrangements with greater positioning precision.

The results presented in this chapter regarding the investigation of SrTiO₃ are published in Ref. [67].

Nanoscale tip positioning

In this chapter, a precise tip positioning technique based on the verification of tip positions via STM scans is presented. Using this method, it is possible to realize four-point measurement setups with all four tips placed in areas smaller than $1 \times 1 \mu\text{m}^2$.

After a short motivation, the principle of the positioning method is explained. The required calibration procedure of the scanning piezo with the optical microscope is demonstrated. It is then shown how absolute distances are determined from the scan images of the calibrated scanner. Finally, the application of this method is illustrated by presenting an example measurement of distance-dependent four-point resistances on the nanometer scale.

3.1. Motivation

As seen in the example measurements in the previous chapter, position-dependent resistance measurements using the four-tip STM are limited to the micrometer scale when the tip positioning is controlled by an optical microscope. With the scale of inter-tip distances approaching the resolution of the optical microscope, distances between the tips as well as the alignment of their positions to each other cannot be realized with certainty, which impairs the validity of determined conductivities. In order to access effects in charge transport that are expected on the nanoscale, control of tip positions via optical microscopy is impractical.

An exemplary optical micrograph of a measurement configuration with inter-tip distances of $\sim 4 \mu\text{m}$ is shown in Fig. 3.1 (a). When estimated from the top view provided by the micrograph, contact points of the tips are assumed to be at the perceptible end of each tip along the

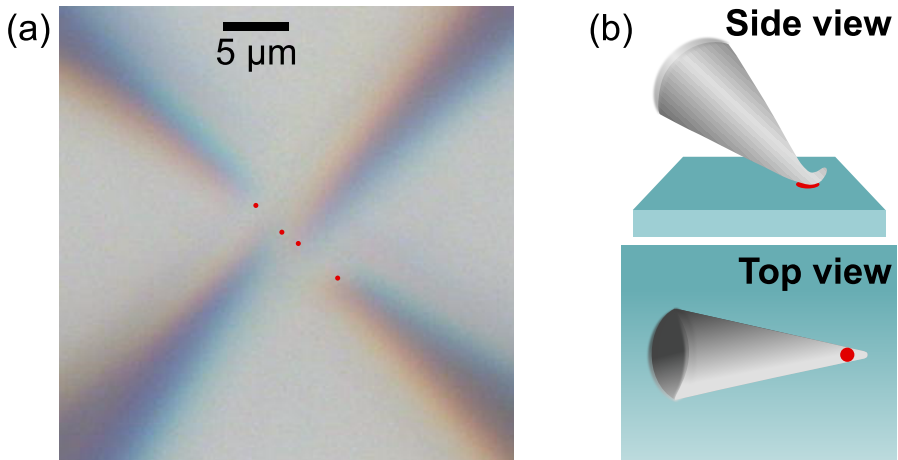


Fig. 3.1.: (a) Optical micrograph of an exemplary linear tip configuration used for four-point resistance measurements. When determining inter-tip distances from optical microscopy, the contact points of the tips are assumed to be at the end of the perceptible tip shape along the mirror symmetry axis, as indicated by the red dots. With inter-tip distances of $\sim 4\ \mu\text{m}$, the dimensions of the configuration are close to the resolution of the microscope. For smaller tip distances, the influence of the uncertainty is too large to reasonably determine electrical sample properties. (b) Schematic illustration of systematic position errors due to plastic tip deformations. When a tip is bent upwards, e.g. due to crude contacting, the respective deformation cannot be identified from the top view. As a result, the actual point of contact to a sample surface is shifted compared to its assumed position at the tip end as determined from the projection.

mirror symmetry axis, as denoted by the red dots in the image. In the presented example configuration, inter-tip distances are close to the order of the microscope resolution, such that a significant uncertainty of the measured four-point resistance is to be expected when moving tips even closer. Furthermore, it is difficult to recognize imminent collisions between the tips when doing so. When an SEM with increased spatial resolution is used for the control of tip positions, as an alternative, tips can in principle be positioned closer. However, the imaging of pristine samples by SEM can have undesired effects on the investigated electronic system [36, 37].

Apart from the image resolution, an additional problem arising from the determination of tip distances using optical means is a possible introduction of systematic position errors due to tip deformations, as depicted in Fig. 3.1 (b). While lateral tip deformations, e.g. due to tip collisions, are easily seen from the top view of the tip arrangement, upward tip deformations cannot be identified as the projected shape of the bent tip appears to be straight. Plastic

upward deformations like this result from repeated crude contacting of hard surfaces. With tip positions nominally assumed to be at the end of the tip shape as it is perceptible in the microscope image, such a deformation introduces an additional error to the determination of inter-tip distances in the order of the bent length segment. As this source of errors is due to the top view of the tip setup being a projection of a three-dimensional objects onto the sample plane, the influence of this issue is also present when tip positions are controlled by SEM imaging.

In order to circumvent the outlined uncertainty issues and reach the nanometer scale of inter-tip distances, a positioning method relying on STM imaging is employed. By using the topography of the sample surface as a basis for tip positioning, tips can be navigated across the surface in tunneling contact with greatly enhanced spatial precision. Furthermore, by using STM scans for identifying desired tip placements on the sample topography, plastic tip deformations do not introduce positioning uncertainties, since the STM images are acquired in tunneling contact by the actual contact point itself. Altogether, tip positioning via STM imaging enables a large range of possible tip configurations only limited by tip radii.

3.2. Principle of positioning

The principal concept of the nanoscale positioning technique is to determine the position of each tip on the surface using the recorded topography of the underlying sample as a reference. This approach is enabled by exploiting the ability of all four STM tips to function as individual scanners.

The principle of the procedure is illustrated in Fig. 3.2. As a first step, one of the four tips (e.g. tip 1) is used to acquire an overview STM scan of a large area of the sample surface, as depicted in Fig. 3.2 (a) for the case of a scan of $4\mu\text{m} \times 10\mu\text{m}$ size. The scanned area is the area of interest for the eventual local four-point investigation. The corresponding topography scan serves as a reference map for the navigation of all tips. Prior to the scanning process, the other tips are moved outside of the scan range to avoid collisions.

After the completion of the overview scan, the idle tips are moved into the scanned region. With the overview scan being large enough, the optical microscope offers sufficient accuracy to do so without tip collisions. Being situated in the scanned overview area, all tips are brought into tunneling contact to perform small scans of the sample surface, as indicated in Fig. 3.2 (b). For the positioning procedure, it is crucial that all tips are located somewhere in the large overview scan in order to guarantee an overlap in the imaged topography with these small scans performed with each tip.

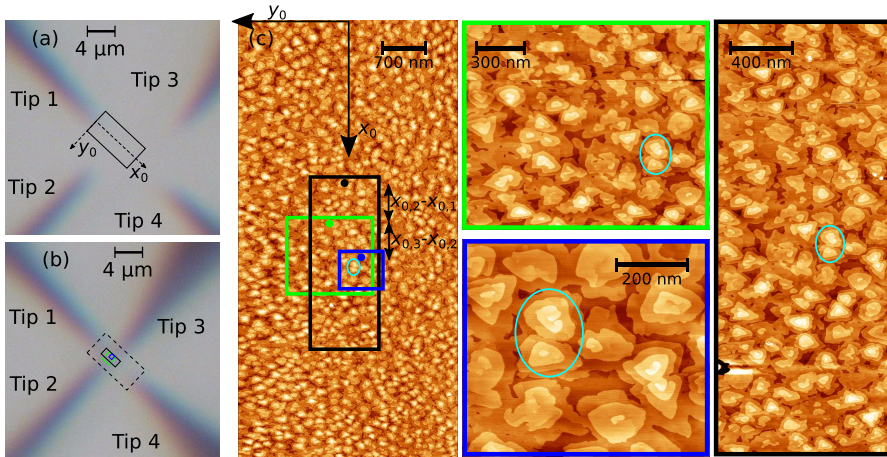


Fig. 3.2.: Principle of the tip positioning procedure based on overlapping STM scans used for transport measurements on the nanoscale. **(a)** One of the STM tips is used to acquire a large overview scan of an area of the sample surface which is targeted for four-point resistance measurements. The recorded overview scan (shown in **(c)** for the present example of a BiSbTe₃ sample) constitutes a reference map for precise tip navigation. **(b), (c)** Subsequently, all four tips are moved into the mapped area to perform small scans individually. The positions of all tips are identified within the reference map by recognition of topographic features from the corresponding small scans in the overview scan. As an example, a characteristically shaped island is highlighted in cyan. After identifying all tip positions in the reference map, the tips are navigated to their target positions to establish electrical contact in the desired configuration. This fine movement is carried out in tunneling contact by piezoelectric control. After every displacement step, the exact position of each tip can be reconfirmed by further scans.

By recognition of distinct features of the imaged sample topography, the small scans performed with each tip can be located in the image of the large overview scan (Fig. 3.2 (c)). Prominent features that are useful for this purpose can be step edges, islands or other characteristically shaped constituents of the topography. If an investigated sample surface happens to have a plain, flat topography without distinct characteristics, features can in principle be generated artificially on the surface prior to performing the overview scan. For this purpose, voltage pulses can be applied with the STM tips while in tunneling contact with controlled separations, leaving marks which can be used as anchor points.

With the small scans identified in the image of the large overview scan, the locations of the respective scanning tips within the overview scan are identified as well. In order to realize a desired tip arrangement on the mapped surface, the tips are navigated across the surface to their target position by xy-control of the scanning piezos without leaving tunneling contact. Fine movement in this fashion is controlled blindly by applying voltage to the scanning piezo

without immediate visual confirmation. Therefore, tips are moved in steps with small STM scans performed in between to reaffirm the changed position within the large overview image.

After navigating all tips to their desired positions, all STM tips are lowered to the sample surface from tunneling contact to establish electrical contact. Within the scope of distance-dependent resistance measurements, the tip positions need to be varied in between electrical measurements. This is done by retracting the respective tips that are intended to be moved back into tunneling contact to navigate them to the next measurement position, while leaving the static tips at their position in hard contact.

From the realized tip configurations in a measurement series, the corresponding tip distances are determined from the positions of the tip in the large overview scan, as indicated in the left panel of Fig. 3.2 (c). As a first approximation, inter-tip distances are evaluated by measuring the nominal lengths in the scan using the calibrated linear piezo constant of the scanner. By considering the non-linearity and the hysteresis of the displacement by the piezo element, as shown in the following sections, distances from the scan can be determined more precisely.

3.3. Sources of image distortion

As mentioned, a first approximation of distances read from the overview scan is given by the known linear piezo constant of the corresponding scanner, which relates the applied voltage to the piezo element from the starting conditions of the overview scan to a nominal lateral displacement x_0 and y_0 in the surface plane. This constitutes the nominal coordinate system indicated in the left panel of Fig. 3.2 (c). However, as can already be seen from the systematically squashed appearance of the imaged islands at large x_0 in the topography scan, the actual displacement x and y of the scanning tip follows a non-linear relation to the applied piezo voltage. Furthermore, the displacement caused by the piezoelectric effect is subject to hysteresis and creep effects. The distortions are pronounced for large nominal displacement. For measurement configurations with small inter-tip distances close to the starting positions of the overview scan, the first approximation is sufficient for distance determination. By accounting for these deviations from the first approximation of a linear response of displacement to applied voltage, however, the precision of distance determination can be improved.

The different sources of error for distance determination from the scan image are evaluated separately. Piezoelectric creep is an effect that only persists for a relatively short time after applying a voltage to the scanning piezo. Its impact on the recorded overview scan can be circumvented by waiting for a sufficient amount of time before starting the scan. Also, even

if a creep effect is present at the start of the scan image, its influence on the determined distances can be easily minimized by realizing a measurement configuration in the center of the overview scan, where the effect has already faded.

Thermal drift in the xy -plane as a further potential source of image distortion is observed to be constant at < 0.3 nm/min in the experiment [34, 68] for the relevant time scale of the overview scan. With an average scanning speed along the slow axis of ~ 17 nm/min, the relative uncertainty of inter-tip distances arising from thermal drift amounts to less than 2%. Thermal drift as a cause of scan distortion is therefore regarded as insignificant with appropriate scanning speeds.

Furthermore, the non-linear response of piezoelectric actuation contributes to image distortion. At large tip displacement, this effect is significant and needs to be considered. To determine the non-linear relation between actual tip displacement x, y and the nominal tip displacement x_0, y_0 directly related to the applied piezo voltage, a quantitative evaluation of the tip displacement as observed in the optical microscope is carried out. This procedure is described in the next section.

Lastly, it is further noted that due to piezoelectric hysteresis, the actual tip displacement as a response to an applied piezo voltage is not only non-linear, but also dependent on the initially applied voltage prior to displacement. To be able to treat the relation of actual displacement to nominal displacement as reproducible, it is necessary that the overview scan in the experiment is performed under the same conditions as the calibration. Therefore, it is crucial to perform the overview scan with the scanning tip after a few hours of rest and according to the same protocol as in the calibration regarding range and speed of the applied piezo voltage.

3.4. Calibration of non-linear piezo response

By evaluating the relative tip movement in the optical microscope, it is possible to find a relation between the nominal displacement and the actual displacement for a specific movement protocol. Constituted by the starting voltage, the voltage range and the speed of voltage application, the movement protocol is chosen to emulate x -motion of the scanning process during acquisition of the overview scan. Optical micrographs that are taken at different stages of displacement during the tip motion are converted into a matrix containing brightness values that can be used for quantitative analysis.

Before the actual displacement can be inferred from the tip movement in microscope images, it is important to first identify the orientation of the x -axis of the scanning system in the

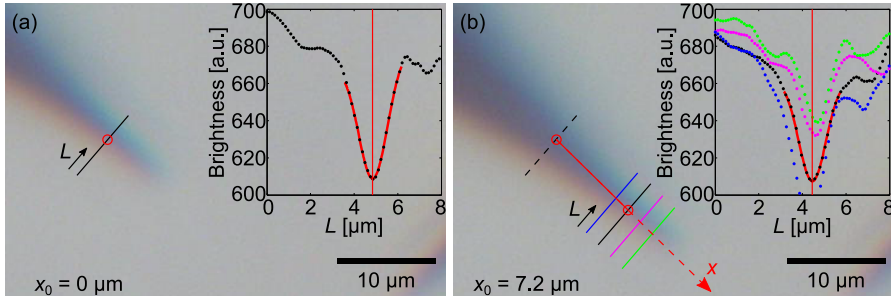


Fig. 3.3.: Identification of the x -axis of the tip movement caused by the piezoelectric actuator. As the tip is moved slowly along the x -direction of the scanning system, a series of microscope images is recorded. **(a)** In the first micrograph, the brightness values of the image are evaluated along a profile line that is drawn across the perceived tip projection. As shown in the inset, the brightness minimum along the line profile is determined as a reference point for the tip position. **(b)** In the other micrographs, multiple line profiles that are strictly parallel to the one in the first image are evaluated across the tip projection. The same reference point as defined in the first micrograph is found by identifying the profile line minimum with the same brightness value, as demonstrated in the inset. The x -axis of the piezo actuation in the microscope perspective is determined as the connecting line between the recognized reference points in all images.

microscope image. To do this, the brightness of the first microscope image during x -motion is evaluated along a profile line that is drawn across the projection of the tip, as depicted in Fig. 3.3 (a). The position of minimum brightness along the profile line is determined as a distinct reference point for the tip projection. In the other microscope images that are taken during the movement protocol, the same reference point can be found by sampling multiple profile lines that are parallel to the one in the previous image across the tip projection and finding the corresponding minimum with the same brightness. This is illustrated in Fig. 3.3 (b). The connecting line between the minima in the microscope images defines the x -axis of the piezo movement.

With the orientation of the x -axis being known, the actual displacement x of the tip can be determined as a function of nominal displacement x_0 from the same microscope images. For this purpose, the image brightness is evaluated along a profile line through the tip projection along the identified x -axis in all micrographs, as shown in Fig. 3.4 (a) and (b). The actual tip displacement in each microscope image is determined by fitting an empiric model function to the line profile and thereby quantifying the movement of the tip projection with respect to the starting point $x_0 = 0$. This method of determining the displacement exploits the fact that while the optical microscope is not useful to identify absolute positions of one tip, relative changes in the tip's positions to each other in the images can be determined more precisely.

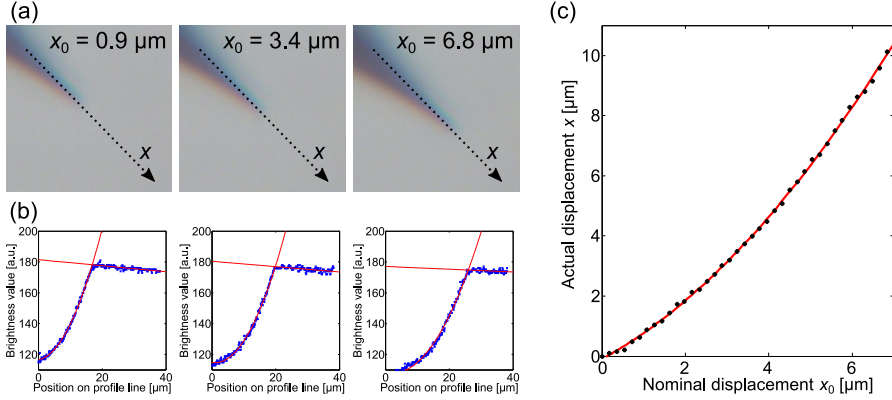


Fig. 3.4.: Calibration of the non-linear piezo response by quantitative analysis of microscope images. **(a),(b)** While being moved along the x -direction according to a defined protocol, microscope images are taken of the tip at different nominal displacement x_0 . The brightness values obtained from the micrographs along the identified x -axis are used to determine the relative movement of the tip projection from one image to another by fitting an empiric model function. The moved distance along the x -axis with respect to the the first image corresponding to starting position $x_0 = 0$ is identified as the actual displacement. **(c)** As expected, quantitatively obtained values of actual displacement follow a characteristic non-linear relation to the nominal displacement. The actual displacement is modeled heuristically by a second order polynomial function. The obtained set of model parameters is strictly associated to the used movement protocol.

The actual tip displacement x as a function of nominal tip displacement x_0 inferred from this quantitative method is presented in Fig. 3.4 (c). The characteristic non-linear behavior of piezoelectric elements is seen clearly. In particular, the deviation of the actual tip displacement from the linear response approximation is apparent for nominal displacements $x_0 > 4\mu\text{m}$. The acquired data set is modeled heuristically by a second order polynomial function

$$x(x_0) = a \cdot x_0^2 + b \cdot x_0 + c, \tag{3.1}$$

which is featured as a red curve in Fig. 3.4 (c). Using this model, any nominal tip position x_0 in the overview scan in Fig. 3.2 (c) can be related to its actual displacement measured from the starting point at the top of the scan. Distances between tips arranged in a vertical line can therefore be determined as

$$x_i - x_j = a \cdot (x_{0i}^2 - x_{0j}^2) + b \cdot (x_{0i} - x_{0j}) \tag{3.2}$$

$$\Leftrightarrow s = a \cdot s_0(x_{0i} + x_{0j}) + b \cdot s_0, \tag{3.3}$$

with s_0 and s denoting the nominal and actual tip distance between a pair of tips indexed by i

and j . It is emphasized that this model is understood to reproduce actual tip displacement in x -direction during the overview scan only for the specific movement protocol it is calibrated to.

The uncertainty of tip distances σ_s determined in this manner is influenced by the uncertainties of the model parameters σ_a and σ_b from the fit and is obtained from the propagation of errors as

$$\frac{\sigma_s}{s} = \frac{\sqrt{(s_0 + 2x_{0j})^2 \sigma_a^2 + \sigma_b^2}}{a(s_0 + 2x_{0j}) + b}. \quad (3.4)$$

For a set of parameters $a = (8.2 \pm 0.3) \cdot 10^{-5} \text{ nm}^{-1}$ and $b = (0.77 \pm 0.02)$ obtained for the exemplary movement protocol presented in Fig. 3.4 (c), the relative uncertainty of determined distances amounts to $\sim 2.5\%$.

The entire displacement calibration procedure relies on the principle that contrary to absolute positions, relative changes in the tip position between several images can be determined confidently by quantitative analysis from optical micrographs. In principle, the calibration of a defined movement protocol could also be done by applying a pattern recognition algorithm to the series of micrographs as a more sophisticated way of determining tip displacement. It is further noted that it is only necessary to characterize the non-linearity of the piezo actuator corresponding to the tip which is performing the large overview scan. Distortions in the smaller scans acquired by the other tips are not relevant, since the determination of tip positions is made via the identification of topographic features in the overview scan.

Since almost all measurements on the nanoscale presented in this work are performed in a linear arrangement along the x -axis of scanning system, only the calibration of piezoelectric x -motion was demonstrated in this section. However, an analogous calibration of the y -motion of the scanning tip can be done using the same principle.

An exemplary distance-dependent four-point resistance measurement realized by the demonstrated positioning technique is presented in the next section.

3.5. Example measurement

Using the presented positioning technique, four-point resistance measurements can be performed in tip configurations that are impossible to realize with optical position control. By using piezoelectric control to navigate tips across the mapped surface in tunneling contact and affirm their positions by performing small local scans, minimum distances between the tips in the experiment are truly only limited by their radii. With high quality tips, it is

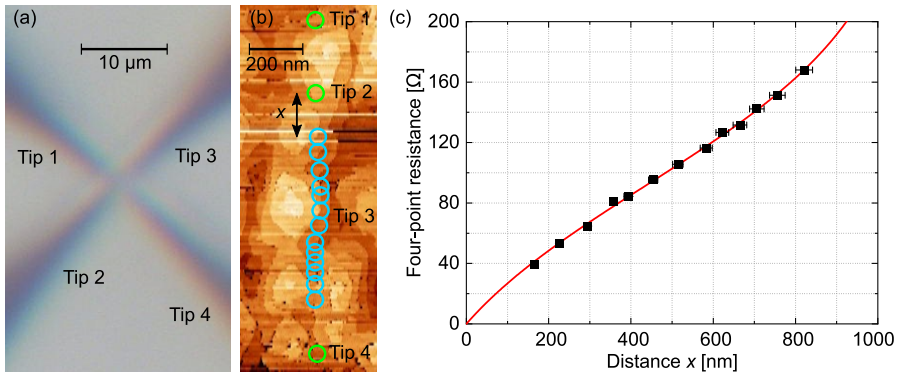


Fig. 3.5.: Distance-dependent four-point resistance measurement of a BiSbTe₃ sample on the nanometer scale. **(a)** Final tip configuration resulting from positioning via STM scans as viewed from the optical microscope. With all four tips placed on the surface within a linear section of just 1.3 μm of length, details of the arrangement are completely indiscernible in the optical view. **(b)** Section of the overview STM scan that is used for the alignment of the tips. The positions of the static tips in the electrical measurements are marked by green circles, while the position of the mobile tip is indicated in cyan. In the experiment, a current is injected between the outer two tips, with the inner two tips probing the resulting potential difference. **(c)** Measured four-point resistance as a function of the distance x between the two voltage-probing tips. The acquired data is explained by a 2D conductivity model represented by the red curve. The conductivity of the sample is determined to (2.76 ± 0.05) mS, which is in agreement with measurements on the micrometer scale.

conceivable to access inter-tip distances $s < 150$ nm in the experiment.

Figure 3.5 presents results of an exemplary distance-dependent four-point resistance measurement on the surface of a template BiSbTe₃ sample. The optical microscope view of the linear tip arrangement with all four tips aligned within 1.3 μm is seen in Fig. 3.5 (a). Evidently, the ends of the tips are indiscernible in the image with the realized inter-tip distances. The positions of the tip in a section of the overview scan are indicated by colored circles in Fig. 3.5 (b).

Within the scope of the corresponding electrical measurements, a current is induced between the outer two tips (tips 1 and 4) of the linear arrangement while simultaneously probing the potential difference between the inner two tips (tips 2 and 3) separated by the distance x . The four-point resistance is acquired at variable x by moving tip 3 along the configuration symmetry line in tunneling contact between each electrical measurement. The measured resistance of the sample as a function of inter-tip distance x is presented in Figure. 3.5 (c). With a spacing of ~ 1 μm left between the mobile voltage probing tip and one of the current-injecting tips, it is possible to probe the local resistance at more than 10 points between the

static tips. As described in the previous section, the distance x , as well as the distances s_{12} and s_{24} between the static tips, are determined from the overview scan image. The acquired data is modeled by applying the general expression for the four-point resistance of a two-dimensional system given by Eq. 2.20 to the geometry of the tip configuration, which results in

$$R_{2D}(x) = \frac{1}{2\pi\sigma_{2D}} \left[\ln\left(\frac{s_{24}}{s_{12}}\right) - \ln\left(\frac{s_{24}-x}{s_{12}+x}\right) \right]. \quad (3.5)$$

From a fit of the model to the data, the two-dimensional conductivity of the sample is determined to (2.76 ± 0.05) mS, which coincides well with measurements at macroscopic distances on the same sample.

In the same manner as in this example, the demonstrated tip positioning method based on STM scans is used for most measurements that are presented in the following chapters.

CHAPTER 4

BiSbTe₃ material system

This chapter is dedicated to the BiSbTe₃ (BST) material system that is the subject of the succeeding investigations. After explaining the conceptual background to the class of topological insulator (TI) systems and the resulting characteristic properties, the ternary compound (Bi_{1-x}Sb_x)₂Te₃ and its realization as a thin film is introduced.

4.1. Topological insulators

Topological insulators are a novel class of materials that, just as an ordinary insulator, possess a bulk energy gap between the valence band and the conduction band. However, at its boundary, a TI additionally hosts gapless states that are protected by time-reversal symmetry. In this context, the boundary of the corresponding system is understood as a surface or an edge in three or in two dimensions, respectively. This means that while the interior of the TI system is insulating, conducting states exist at its termination that are robust against local perturbations.

4.1.1. Chern number

In general, the topological class of an electronic system is determined by its topological invariant. For systems that are not constrained by time-reversal symmetry, this topological invariant is given by the Chern number $n \in \mathbb{Z}$, which can be viewed as analogous to the genus of geometrical shapes in mathematics. For a system with translational symmetry described

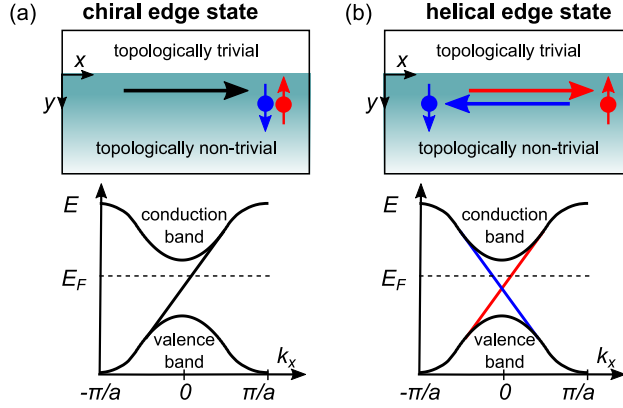


Fig. 4.1.: Sketch of topologically protected edge states with different symmetry relations in two dimensions. **(a)** With broken time-reversal symmetry, topological edge states have chiral character, which means that carriers in the edge states propagate in one direction only. This corresponds to a single branch in the band gap. The depicted spin-degenerate case is the quantum Hall insulator phase. The analogous spin-filtered case is the quantum anomalous Hall phase, where the one-way mode is populated by carriers of only one spin type. **(b)** When time-reversal symmetry is not broken, the edge states of a topological insulator are of helical nature. This property denotes two counter-propagating modes with reversed spin, corresponding to two spin-dependent branches in the band gap. The depicted example case is the quantum spin Hall phase.

by a Hamiltonian $\mathcal{H}(\vec{k})$ such as a crystal, the solutions to Schrödinger's equation are given by periodic Bloch states $|u_m(\vec{k})\rangle$, where m denotes the index of occupied bands. The Chern number of this system is then given by [69]

$$n = \sum_{m=1}^N \frac{1}{2\pi} \int_{\text{BZ}} \vec{\nabla}_k \times i \langle u_m(\vec{k}) | \vec{\nabla}_k | u_m(\vec{k}) \rangle dS \quad (4.1)$$

with dS being the surface element in reciprocal space and BZ denoting the Brillouin zone. The expression in the integral is called *Berry flux* and upon evaluation of the integral results in the additional phase that is picked up by the wave function when traversing a closed loop in the Brillouin zone [70–72]. Systems that share the same n and therefore belong to the same topological equivalence class can be transformed into each other by continuous deformations of the underlying Hamiltonian without closing the energy gap. A direct consequence of this circumstance is the existence of boundary states. At the interface between two insulating systems of different topological equivalence class, the Chern number changes, which implies the closure of the band gap in between and results in a metallic state that is bound to the interface. Since the sole existence of the crossing between the two topologically distinct insulators guarantees the discontinuous transformation of \mathcal{H} at the boundary, the resulting

interface state is *topologically protected*.

Depending on the details of the Hamiltonian of the regarded system, namely its behavior under the effect of the time-reversal operator, the charge-conjugation operator and their combination, the emerging boundary states obey different symmetry relations. The different types of boundary states are frequently termed as *chiral* and *helical* [73]. As illustrated in Fig. 4.1 for the two-dimensional case, *chiral* refers to the fact that the electronic edge states propagate in one direction only (e.g. in the quantum Hall effect and the quantum anomalous Hall effect), while *helical* denotes the existence of counter-propagating modes with correlated spin (e.g. in the quantum spin Hall effect).

4.1.2. \mathbb{Z}_2 topological insulator

The Chern number represents a descriptive example of the principle of classification by topological invariants. However, the use of the Chern number for topological classification is limited to Hamiltonians with broken time-reversal symmetry, such as in the case of the quantum Hall insulator [74]. In systems constrained by time-reversal symmetry, the Chern number is always $n = 0$ [75] and therefore is not a suitable invariant to distinguish between topologically distinct classes. For time-reversal invariant systems of spin $\frac{1}{2}$ particles, the \mathbb{Z}_2 invariant ν [12] is used for this purpose. This quantity is closely related to the Chern number and can have two possible values, which determine whether the system is topologically trivial ($\nu = 0$) or non-trivial ($\nu = 1$).

A fundamental property of time-reversal invariant periodic systems described by a Bloch Hamiltonian $H(\vec{k})$ is the existence of eigenstate pairs. These so-called Kramers pairs are found at opposite \vec{k} , which is shown by the action of the time-reversal operator Θ on the Hamiltonian

$$H(-\vec{k}) = \Theta H(\vec{k}) \Theta^{-1}. \quad (4.2)$$

This property means that at points of time-reversal invariant momenta (TRIM) Γ_i in the Brillouin zone, where $\vec{k} = -\vec{k}$ is satisfied due to periodicity, the Kramers pairs are degenerate and the corresponding bands must intersect. Whether these Bloch eigenstate pairs even exist in the band gap depends on the details of the Hamiltonian. The degeneracy of Kramers pairs at the TRIM points in reciprocal space is exploited to determine the topological \mathbb{Z}_2 invariant ν . This is done by determining the unitary matrix [76]

$$w_{mn} = \langle u_m(\vec{k}) | \Theta | u_n(\vec{k}) \rangle \quad (4.3)$$

from the occupied Bloch states and using it to calculate the time-reversal parities $\delta_i = \pm 1$ for

each of the TRIM Γ_i . The relation to the topological invariant ν of the system is then given by

$$(-1)^\nu = \prod_i^N \delta_i, \quad (4.4)$$

where N is the number of TRIM points in the Brillouin zone given by dimensionality. The Bloch states in the band gap that connect the TRIM points in reciprocal space cross the Fermi surface either an even or an odd number of times. While the nature of these connections is entailed in the expression on right side of this relation, the related number of Fermi surface crossings modulo 2 is given by the invariant ν . For an odd number of crossings $\nu = 1$, the system is topologically non-trivial. The changes in parity between the TRIM necessitating topological non-triviality are caused by a local inversion of the band gap in reciprocal space [77], which is an essential property for the existence of non-trivial \mathbb{Z}_2 topological phases.

In general, the determination of δ_i from Bloch states is intricate, but is simplified if the considered time-reversal invariant system additionally obeys inversion symmetry. In this case, the Bloch states $|u_n(\Gamma_i)\rangle$ are eigenstates of the parity operator with eigenvalues $\xi_m(\Gamma_i) = \pm 1$ and the topological invariant is given by [77]

$$(-1)^\nu = \prod_i^N \prod_m \xi_m(\Gamma_i), \quad (4.5)$$

which reduces the complexity for identifying topological phases from band structure calculations [75].

4.1.3. 2D and 3D topological insulators

In two dimensions, the topologically non-trivial phase that is manifested in a time-reversal invariant system with $\nu = 1$ is the quantum spin Hall (QSH) phase. The respective class of systems is also called 2D topological insulator and hosts characteristic 1D helical edge states at its boundary, as sketched in Fig. 4.2 (a). The helicity of the edge states is due to the underlying constraint imposed by Kramers theorem, which requires that the eigenstate pairs that exist at opposite momentum \vec{k} have a reversed spin. This topological phase was initially hypothesized to exist in graphene with additional spin-orbit interaction [78]. Soon after, HgTe quantum well systems were predicted to exhibit the QSH phase [14], which was subsequently confirmed experimentally [13].

It was found that the concept of the \mathbb{Z}_2 topological insulator can be generalized to three dimensions, resulting in what is called 3D topological insulator [79–81]. In three dimensions, there are more TRIM in the Brillouin zone than in two dimensions and therefore more possible parity changes between them according to Eq. 4.4. Thus, the full topological classification of

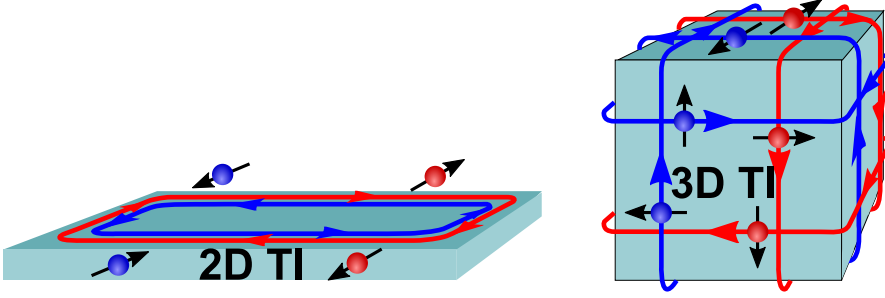


Fig. 4.2.: Real-space illustration of the boundary states of the \mathbb{Z}_2 topological insulator in 2D and 3D. **(a)** In the 2D topological insulator, metallic states exist at the 1D boundary of the system, while the 2D surface is insulating. Due to the helical nature of the edge states resulting from Kramers theorem, carriers with opposite momentum possess opposite spin. **(b)** In the 3D topological insulator, the 3D interior is insulating with helical conducting 2D states existing at the surface of the system. As in the case of the 2D TI, the carrier spin is correlated with carrier momentum. Since all surfaces host topological surface states in the example, the depicted phase is a strong topological insulator.

3D systems requires a notation of four invariants ($\nu_0; \nu_1 \nu_2 \nu_3$). In case of $\nu_0 = 1$, the regarded phase is a *strong* topological insulator and exhibits helical surface states on all of its 2D boundaries, as depicted in Fig. 4.2 (b). As these states are topologically protected, they are usually termed *topological surface states* (TSS). For (0;000), the system is considered topologically trivial. In case of $\nu_0 = 0$, but $\nu_i = 1$ for at least one $i \in \{1, 2, 3\}$, the resulting topological phase is called *weak* topological insulator and hosts topologically non-trivial 2D states only on some of its six surfaces, which are specified by the ν_i . A weak topological insulator can be interpreted as a non-interacting stack of QSH phases on top of each other, in the sense that topologically non-trivial states are only found on those surfaces of the resulting stack that are formed by the edges of the QSH layers. The existence of the 3D topological insulator phase was predicted in different material systems by Fu and Kane [77] before being demonstrated experimentally for the first time shortly after in $\text{Bi}_{1-x}\text{Sb}_x$ [82], also revealing the helical nature of the surface states [83]. The binary alloys of Bi_2Se_3 , Bi_2Te_3 and Sb_2Te_3 were also hypothesized to belong to this topological class [84], which was confirmed experimentally [15, 85, 86]. These material systems are particularly interesting for applications due to their large bulk band gap.

As evident from Eq. 4.4, what makes a system \mathbb{Z}_2 non-trivial is the change of parity between TRIM in the Brillouin zone. This corresponds to a local inversion of the band gap in reciprocal space as a necessary condition for $\nu = 1$. For 2D and 3D topological insulators, this gap inversion is caused by strong spin-orbit interaction [75, 78]. In material systems consisting of different heavy elements, where the effect is particularly strong, the energy level splitting

caused by spin-orbit interaction can reverse the ordering of the atomic orbitals in the energy scheme. In the band structure of the corresponding crystal, this results in a reversal of the valence band and the conduction band, i.e. the inversion of the band gap.

Spin-orbit coupling, in its explicit form is obtained from an expansion of the Dirac equation [87] as

$$H_{\text{SO}} = -\frac{\hbar}{4m^*c^2}\sigma \cdot (\vec{p} \times \vec{\nabla}V), \quad (4.6)$$

where σ and V are the Pauli matrices and the coulomb potential of the nucleus, respectively. In the crystal, this component of the Hamiltonian acts on charge carriers similar to an effective magnetic field caused by $(\vec{p} \times \vec{\nabla}V)/(m^*c^2)$. However, contrary to external magnetic fields, spin-orbit interaction does not break time-reversal symmetry and therefore is no contradiction to the constraint imposed on a \mathbb{Z}_2 topologically non-trivial phase. The nuclei of heavy elements exert a particularly strong potential gradient on charge carriers, causing a strong spin-orbit interaction in the crystal. For this reason, many known compound topological insulator materials contain such elements [88].

Since the essential spin-orbit interaction is a relativistic effect, the description of a 2D or 3D topological insulator suggests the use of the Dirac Hamiltonian [84]

$$H = c\vec{p} \cdot \alpha + mc^2\beta, \quad (4.7)$$

which in general enables coupling of electron spin, momentum, coulomb interaction and optional external fields with each other. The Dirac matrices α and β in this equation satisfy specific relations arising from anticommutation and can be expressed by the Pauli matrices σ_i depending on the dimensionality. As described in detail in Ref. [89], the character of the edge states arising from 2D and 3D topological insulators can be motivated from a quadratic correction to the Dirac equation as

$$H_{2\text{D}/3\text{D}} = v\vec{p} \cdot \alpha + (mv^2 - B\vec{p}^2)\beta, \quad (4.8)$$

where mv^2 represents the band gap and B^{-1} is a parameter with the dimension of mass. The description of topological boundary states entails a solution of the 1D Dirichlet problem for a boundary at $x = 0$ for zero energy

$$h_{1\text{D}}\phi(x) = [-i\hbar v\partial_x\sigma_x + (mv^2 + B\hbar^2\partial_x^2)\sigma_z]\phi(x) \quad (4.9)$$

and treating the extension of the problem to 2D and 3D as a perturbation of the 1D Hamiltonian by the additional y - and z -dependent components

$$H_{2\text{D}/3\text{D}} = h_{1\text{D}}(x) + \Delta H_{2\text{D}/3\text{D}}, \quad (4.10)$$

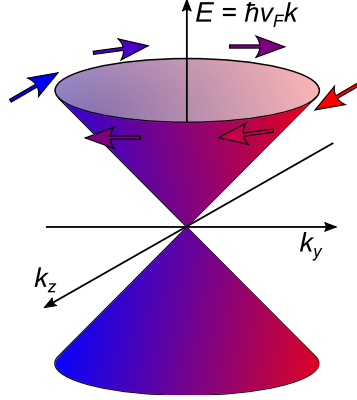


Fig. 4.3.: Illustration of the Dirac cone of a 3D topological insulator. The conical shape in reciprocal space describing the linear TSS is resulting from the surface dispersion relation. Therefore, the Dirac cone is only found at the interface of the 3D TI. For each point \vec{k} on the Dirac cone, a state with opposite carrier spin exists at reversed momentum $-\vec{k}$, which denotes helicity.

with the perturbation terms

$$\Delta H_{2D}(y) = -i\hbar v \partial_y \alpha_y + B\hbar^2 \partial_y^2 \beta \quad (4.11)$$

$$\Delta H_{3D}(y, z) = -i\hbar v \partial_y \alpha_y - i\hbar v \partial_z \alpha_z + B(\hbar^2 \partial_y^2 + \hbar^2 \partial_z^2) \beta. \quad (4.12)$$

For both cases, the effective boundary Hamiltonian describing the topological edge states are obtained from

$$H_{2D/3D}^{\text{eff}} = (\langle \Psi_1 |, \langle \Psi_2 |) \Delta H_{2D/3D} \begin{pmatrix} | \Psi_1 \rangle \\ | \Psi_2 \rangle \end{pmatrix} \quad (4.13)$$

where $|\Psi_1\rangle$ and $|\Psi_2\rangle$ are the eigenstate spinors assembled from the two solutions of $\phi(x)$ to Eq. 4.9. The explicit forms of the boundary Hamiltonian in 2D and 3D are determined to

$$H_{2D}^{\text{eff}} = \text{sgn}(B) v p_y \sigma_z \quad (4.14)$$

$$H_{3D}^{\text{eff}} = \text{sgn}(B) v (p_y \sigma_z - p_z \sigma_y), \quad (4.15)$$

which emphasize the helical nature of the boundary states, as evident from the correlation of spin and momentum. The dispersion relations corresponding to these effective edge/surface Hamiltonians are found as

$$E_{2D}^{\pm}(k_y) = \pm \hbar v k_y \quad (4.16)$$

$$E_{3D}^{\pm}(k_x, k_y) = \pm \hbar v \sqrt{k_y^2 + k_z^2} = \pm \hbar v k, \quad (4.17)$$

denoting that carriers have opposite velocity $\pm v$ in their two spin states. The dispersion of the 2D case corresponds to the illustration in the lower panel of Fig. 4.1 (b). The 3D

topological insulator dispersion is shown schematically in Fig. 4.3 as what is termed *Dirac cone*. The rotation of the charge carrier spin with momentum around the Fermi surface denotes helicity, as indicated by the arrows in the sketch. This perpendicular relation is also called spin-momentum locking. As the topological surface states of BST material systems are described by such a Dirac cone in reciprocal space, this dispersion relation is essential for this work.

One fundamental property which is conditioned by the helical character of boundary states of topological insulators is the suppression of backscattering. Since there do not exist available states with the same carrier spin at momenta \vec{k} with different orientation due to Kramers theorem, carrier scattering always necessitates a simultaneous change of the spin. In 2D TIs, this implies in a complete prohibition of scattering without spin-flipping processes, resulting in ballistic transport. Similarly, direct backscattering is suppressed entirely on the surface of a 3D TI [90, 91]. However, small-angle scattering requiring only small changes of spin orientation are still possible in the TSS, which allows diffusive transport.

4.2. BiSbTe₃ thin films

Since the discovery of their non-trivial character as strong topological insulators [84–86], the binary materials Bi₂Te₃ and Sb₂Te₃ are in the focus of 3D TI research. In particular, their large bulk band gaps of 0.17 eV [85, 86] and 0.3 eV [92], respectively, make these alloys interesting for applications at room temperature. However, as the Fermi level in both materials cuts the bulk bands, both systems possess a significant number of bulk carriers. While Bi₂Te₃ is intrinsically n-doped, Sb₂Te₃ exhibits p-type behavior. Due to the opposite doping of the two binary systems and their similar lattice parameters, it is possible to realize crystalline ternary compounds consisting of the three elements, which results in a significantly reduced bulk carrier concentration [93–97]. The topological \mathbb{Z}_2 classification of the BST system is (1;000), which implies that there is only one Dirac cone in the Brillouin zone, located at the Γ point. This circumstance and the lack of hexagonal warping, i.e. deviations from the circular shape of the 2D Fermi surface, facilitate the interpretation of experimental results based on the TSS.

Throughout the entire composition range, the (Bi_{1-x}Sb_x)₂Te₃ crystal is ordered in a tetradymite structure [88]. The compound crystallizes in sequences of five covalently bonded atomic layers of Te-X-Te-X-Te, with X being substituted partially with Bi and Sb atoms. One such sequence defines a quintuple layer (QL) and is approximately 1 nm in height. One unit cell of the crystal consists of three quintuple layers in the stacking order ABC-ABC, as depicted in Fig. 4.4 (a). In this structure, the individual quintuple layers are only weakly bonded to each other by van der Waals forces, making it in principle possible to cleave the layers with ease.

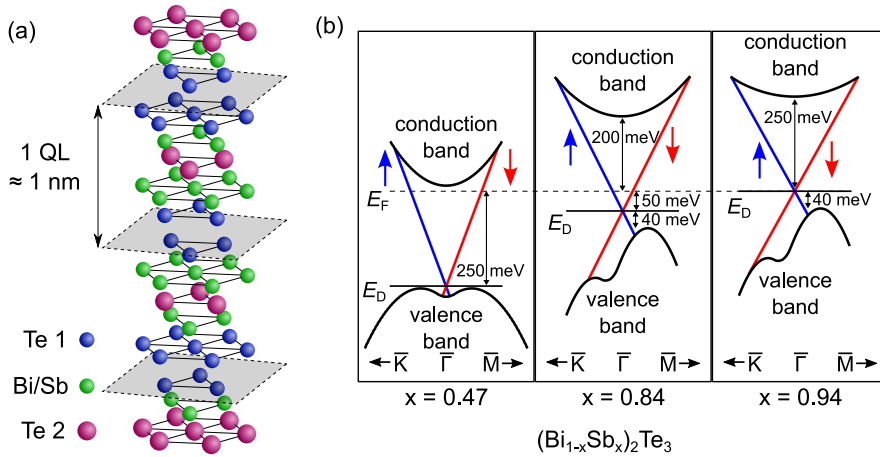


Fig. 4.4.: (a) Schematic representation of a BST unit cell. The crystal forms in a tetradymite structure. Five covalently bonded atomic layers constitute a quintuple layer stack. An ABC-ABC ordering sequence of van der Waals bonded quintuple layers composes the periodic structure of the crystal. The atomic layers denotes as Te 1 and Te 2 differ in their distinct bonding character to the neighboring Bi/Sb atoms. (b) Illustration of the band structure of the BST system at the Γ point. Depending on the proportion of Bi and Sb, the position of the bands with respect to the Fermi energy can be tuned in a controllable manner [100], resulting in a population of the TSS at different levels. The three illustrated material compositions signified by x are the ones that were investigated in this work.

There are various methods of realizing BST systems. All samples investigated in this work are thin films of BST grown by molecular beam epitaxy (MBE) on Si(111) substrates. The MBE growth of the investigated thin films is carried out according to Ref. [98]. The process entails slow deposition of the atomic components on the Si(111) surface in UHV conditions. The simultaneous deposition of Bi and Sb at appropriate rates enables the formation of the ternary system in desired compositions. Prior to the simultaneous material deposition, a single layer of Te is used to saturate the dangling bonds of the Si(111) surface. This procedure called van der Waals epitaxy minimizes strain on the grown BST structure which otherwise is significant due to the lattice mismatch. The additional layer of Te has been shown to have negligible conductance compared to the BST system [99], which is important in terms of undesired parallel contributions to charge transport. All BST samples discussed in this work were grown by Michael Schleenvoigt.

Depending on the proportion of Bi and Sb atoms in the material composition, the bulk carrier concentration of the resulting thin film can be controlled. In the frame of the band structure, this corresponds to a relative shift of the bands of the TI with respect to the Fermi level. As the

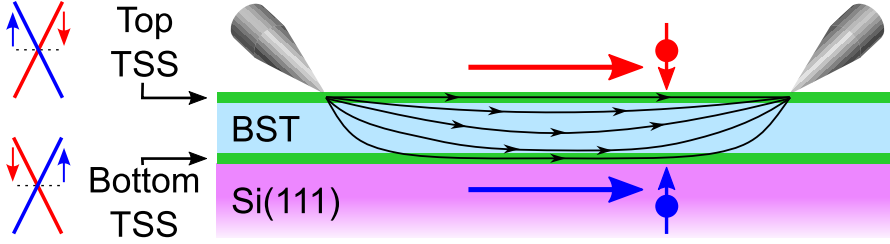


Fig. 4.5.: Illustration of charge transport in BST thin films. With film thicknesses $L \ll s$, where s is the distance between tips, the injected current is in principle transmitted by all parallel conduction channels. Even when the contribution from bulk states in the interior of the TI can be neglected, both TSS at the opposite interfaces need to be considered.

(Bi_{1-x}Sb_x)₂Te₃ composition is varied between $x = 0$ and $x = 1$, the material system changes its behavior from n-type to p-type.

The position of the Fermi level in the band structure is an important quantity for the interpretation of acquired electrical measurement results. For the three BST compositions that were investigated in the scope of this work, namely those corresponding to $x = 0.47$, $x = 0.84$ and $x = 0.94$, the Fermi level position is inferred from interpolation of previous ARPES results of BST samples grown in the same system. In a prior investigation of a BST thin film with $x = 0.94$, the position of the Fermi level with respect to the Dirac point was determined to $E_F = (2 \pm 7)$ meV by means of angle-resolved photoemission spectroscopy (ARPES) [100]. Furthermore, the study revealed the position of the Dirac point to be ~ 40 meV above the bulk valence band. For a BST thin film with $x = 0.47$ grown in the same MBE system, ARPES results show that the Fermi level position with respect to the Dirac point is $E_F = 250$ meV [101], with the Dirac point being at the valence band edge. For the BST composition range $0.5 \leq x \leq 1$, the position of the Fermi level with respect to the Dirac point in the band gap is linearly dependent on the portion of Sb x [93]. Using this relation and the experimentally confirmed values of $E_F(x = 0.47) = 250$ meV and $E_F(x = 0.94) = 0$ meV, the location of the Fermi level in case of $x = 0.84$ is determined to $E_F(x = 0.84) = 50$ meV. For this attribution, the stoichiometry of the samples investigated in this work was determined *ex situ* after all electrical measurements. The positions of the Fermi level for the three compositions of interest are shown schematically in Fig. 4.4 (b). The bulk band gap of the material composition of $x = 0.47$ is known to be ~ 260 meV [101]. In case of the Sb-rich composites with $x = 0.94$ and $x = 0.84$, the band gap is assumed to be close to the value of ~ 300 meV that is found for Sb₂Te₃ [92].

It should further be noted that the band structure inferred from ARPES refers to the surface

of the material. As sketched in Fig. 4.5, in thin film systems with thicknesses in the range of $L \approx 10$ nm, TSS from both film interfaces, at the top interface with the vacuum, as well as at the bottom interface with the substrate, contribute to transport. In general, the positions of the Fermi level at the two interfaces can be different [97, 101]. Furthermore, the ARPES data used for interpolation is valid for BST films of ~ 10 nm thickness. In the ultra-thin film limit of single-digit nanometer thicknesses, the Fermi level can shift due to increasing interaction of the interfaces.

Spin-polarized charge current in a topological insulator

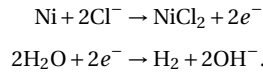
As introduced in the previous chapter, the topologically protected surface states in the band gap of the TI are helical in character. Electrons populating the TSS therefore have a spin that is locked to their momentum. This property is a hallmark of topological insulators. Due to this spin-momentum locking, TI materials in principle enable a straightforward way of generating spin-polarized charge carriers. In contrast to topologically trivial systems, where external magnetic fields or ferromagnetic current-injection contacts are needed to polarize charge currents, spin polarization in TIs is achieved by the mere injection of a charge current alone. The intrinsic polarization is therefore a valuable property for spintronics applications [16, 102] and also finds use in quantum computation [25].

This chapter demonstrates the determination of the intrinsic spin polarization of TSS in BST films by the detection of a spin voltage signal in charge transport. Using the four-tip STM, the locking of carrier spin and momentum is investigated in transport measurements for samples of two different compositions, $(\text{Bi}_{0.06}\text{Sb}_{0.94})_2\text{Te}_3$ and $(\text{Bi}_{0.53}\text{Sb}_{0.47})_2\text{Te}_3$. For this purpose, a magnetized ferromagnetic Ni tip is used as one of the voltage-probing contacts as a means of spin detection. In the past, a similar *in situ* multi-tip investigation of the spin voltage was performed on bulk $\text{Bi}_2\text{Te}_2\text{Se}_3$ by Hus et al. [103]. Due to the high bulk carrier contribution of the underlying sample, a finite signal was obtained only at low temperatures [104]. In case of the thin film samples studied here, a finite spin signal is detected at room temperature conditions. To satisfy the required conditions regarding the precision of tip positions for measuring a spin signal, the precise positioning method employing STM scans of the local

topography with each individual tip, as described in chapter 3, is used to contact the sample.

5.1. Preparation of Ni tips

The ferromagnetic tip that is used as a spin-sensitive contact in the experiment is etched from a nickel wire. The initial wire is 250 μm in diameter and is etched in a KCl solution. Two methods of electrochemical etching based on the same principle were considered for fabrication of Ni tips, as shown schematically in Fig. 5.1. In both setups, the Ni wire is etched by an electrolysis process involving the to-be-etched wire, a counter-electrode and the electrolyte. The nickel wire serving as the anode, as well as a platinum cathode, are in contact with the KCl solution and form a closed circuit. Upon application of a DC voltage between the electrodes, a chemical reaction occurs according to [106, 107]



This process entails the flow of a current from the anode to the cathode and results in the desired dissolution of the Ni wire which eventually forms the tip shape during the etching. The details of the tip shape are governed by the etching dynamics and determined by various parameters of the procedure such as bias voltage, electrolyte concentration and the nature of contact between the nickel wire and the electrolyte. Furthermore, the application of an AC current can lead to a modified tip apex.

5.1.1. Etching setups

In one of the considered etching methods, which is depicted in Fig. 5.1 (a), a Pt wire serving as the cathode is formed into a ring with a diameter of 10mm which holds a thin film of the KCl electrolyte by surface tension. This film suspension is realized by immersing the ring in a beaker of KCl solution. Then, the to-be-etched Ni wire is threaded through the thin film, such that the etching circuit is closed by the contact area between the wire and the liquid. In the second approach, the Ni wire and the Pt ring are both submerged into a beaker containing the KCl electrolyte, as illustrated in Fig. 5.1 (b). In both methods, the etching process is finished by shutting off the bias voltage once the entire tip diameter is etched through, resulting in a hyperboloid shape of the tip apex. For this purpose, a supplementary etching circuit according to Ref. [105] is used to automatically terminate the power supply when the tip is etched through. This immediate cut-off is realized by an operational amplifier after a significant increase in the resistance load relative to a preset reference value is detected.

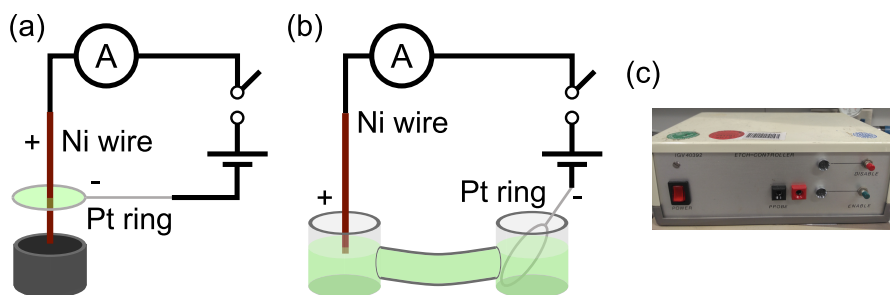


Fig. 5.1.: Schematic illustration of the setups considered for electrochemical Ni tip etching. **(a)** The to-be-etched Ni wire is threaded through a suspension of KCl solution which is held by a Pt ring due to surface tension. The etching occurs by applying a bias voltage between the Ni wire (anode) and the Pt ring (cathode), resulting of a current flow through the electrolyte. This method of etching proves to yield inconsistent results due to variable thickness of the electrolyte film. **(b)** Similarly in principle, the second considered etching setup is obtained by submerging the Ni wire and the Pt ring into a beaker containing the KCl solution. Since the contact area between the Ni wire and the electrolyte is well-defined for a given immersion depth, the etching process results in reproducible outcomes. This etching method is chosen for all Ni tips used in this work. **(c)** Photograph of the etch controller according to Ref. [105] that is used to automatically terminate the etching process.

The resistance load is determined by the contact area between the Ni wire and the electrolyte, while the reference value is adjusted using a potentiometer. The etch controller that is used for terminating the etching process is depicted in Fig. 5.1 (c).

The etching method using the suspension of electrolyte generally yields two available tips. Once the Ni wire is successfully etched through, the lower part of the wire is dropped and can be caught in a small tube. The two resulting tips are found to systematically differ in their appearance. As presented in Fig. 5.2 (a), the lower tip tends to be sharp, but elongated with a small opening angle of the apex. This characteristic shape is likely to be caused by the force of the own tip weight acting on the wire neck. Due to a sudden termination of electrical contact, the etching of the lower tip stops immediately after the rupture of the two wire sections. It is frequently observed that, especially when the length of the lower tip section exceeds ~ 7 mm, the tip apex is microscopically bent at the end. This is explained by a recoil effect due to a sudden mechanical rupture of the neck region as the two tip sections separate [105]. The upper tip, as shown exemplary in Fig. 5.2 (b), generally has a more compact shape and exhibits a high variance of apex sharpness. The sharpness of the upper tip is most notably influenced by the cut-off time of the etching electronics. When the tip is etched in the suspended electrolyte film, the initial resistance load is dependent on the thickness of the film, which is difficult to control. As a result, the cut-off mechanism is observed to behave

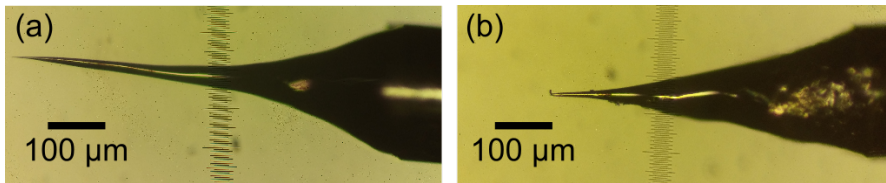


Fig. 5.2.: Examples of the two Ni tips resulting from etching in a suspended KCl film. **(a)** The lower tip resulting from the etching process generally exhibits an elongated apex. The sharp apex is caused by an immediate termination of etching after the rupture of the two wire sections. As a consequence of the abrupt release of mechanical stress, the lower tip can be bent microscopically at the apex end [105]. **(b)** The upper tip usually has a shorter apex, but suffers from inconsistent termination of the etching process due to the hardly controllable wire-electrolyte interface area. The delayed stop of etching results in blunt tip apices.

inconsistently for a given set of etching parameters. With both tips showing a variable degree of quality, the etching method using a film suspension is considered unreliable.

In contrast, the etching procedure yields reliable results when the Ni wire and the Pt ring are submerged into the KCl solution. The etching parameters can be adjusted to result in a desirable tip shape. Since there is little variability in the details of the wire-electrolyte interface for a given immersion depth, the cut-off mechanism yields reproducible and sharp tip apices if configured appropriately. Due to superior reliability, this etching setup is used for the realization of all relevant Ni tips in this work.

5.1.2. Etching procedure

The characteristics of the fabricated Ni tip generally depend on various parameters of the etching process. While the sharpness of the tips is most sensitive to the cut-off time of the power supply to stop the chemical reaction, the applied voltage, the concentration of the electrolyte and the immersion depth all have an influence on the tip quality. The best outcome is achieved by a specific set of parameters and the quality of resulting tips is ensured by the reproducibility of the process when etched while submerged in the solution.

After cleaning the Ni wire by immersion in isopropanol and careful wiping with a tissue, the power source is connected to the Ni wire and the Pt ring as sketched in Fig. 5.1 (b). Both elements are then submerged in a 1.5M solution of KCl contained in a beaker. The Ni wire is submerged in the liquid to an immersion depth of ~ 0.75 mm, while the Pt ring is immersed in such a way that the entire circular shape is beneath the surface. To start the electrolysis, a bias voltage of 3V is applied, resulting in an average etching current of ~ 12 mA using these

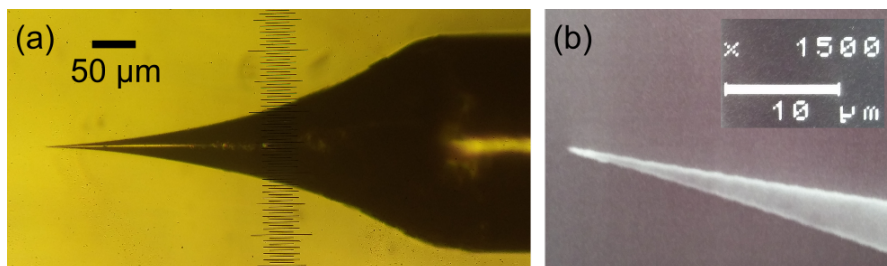


Fig. 5.3.: Typical Ni tip obtained from etching when submerged in a KCl solution. **(a)** When submerged in the electrolyte for a defined depth, the etching process corresponding to a given set of parameters is reproducible. As a result, the immediate voltage cut-off determining the sharpness as controlled by the etching circuit behaves consistently. **(b)** Scanning electron microscope image of a typical Ni tip produced from submerged etching. The radius of curvature of tips resulting from this method is below 200 nm.

conditions. Generally, lower bias voltages of $\leq 1.5\text{V}$ result in a process outside of the polishing regime and yield unusable tips with irregular and rough apices. An exemplary resulting tip is presented in Fig. 5.4 (a).

On average, the entire etching process takes approximately 2 min before the Ni wire is etched through at the neck region and small piece of the wire drops into the liquid. To stop the process as soon as this happens without delay, the reference resistance of the cut-off electronics is fine-tuned for the presented set of parameters. If the dissolution of the Ni wire continues after the rupture of the neck region, the reference resistance of the circuit is too high.

Throughout the procedure, the electrolyte close to the wire assumes a green tint due to the reaction product NiCl_2 which dissolves in the liquid. Already after $\sim 15\text{s}$ of ongoing etching, insoluble residual material – possibly nickel oxides – accumulates at the wire close to the etching point, as seen in Fig. 5.4 (b) as dark agglomerate. It is frequently observed that this residue can disturb the local etching dynamics as it drifts on the surface, which leads to inconsistent results. This disturbance can be circumvented by manually interrupting the etching process after $\sim 20\text{s}$ to clean the accumulating residue. For this purpose, the pre-etched Ni wire is dipped into isopropanol before carefully wiping its end with a clean tissue. As a result, a silverish shimmer is visible at the end of the wire. Subsequently, the Ni wire is submerged in the solution again at the same immersion depth as in the pre-etching phase and the electrolysis process is continued, as presented in Fig. 5.4 (c). If the tip is submerged deeper into the solution than before the cleaning, the etching point is above the pre-etched end of the wire and the produced tip tends to be too blunt. With the residue removed, the dissolution of Ni can proceed undisturbed until the fabrication of the tip is complete after

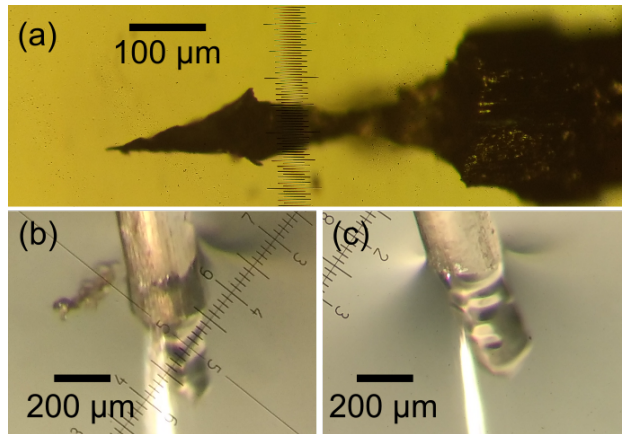


Fig. 5.4.: (a) Nickel tip obtained after etching at low bias voltages of ≤ 1.5 V. Due to the electrolysis process proceeding outside of the electropolishing regime, the Ni wire is eroded into rough and irregular shapes. Tips resulting from this process are unsuitable for STM. (b) Initial stage of the etching process as observed by an optical microscope. After ~ 15 s into the process, insoluble residual material accumulates at the submerged Ni wire. The residue can influence the etching dynamics depending on its diffusion on the surface of the liquid and therefore leads to inconsistent outcomes. (c) Continued etching of the same Ni wire after removing the residue material. After 20 s of pre-etching, the process is interrupted to remove the accumulating residue using isopropanol and a clean tissue. Subsequently, the wire is placed back into the setup at the same immersion depth to finish the etching process.

the remaining 1.5 min of the process. Once the etching process is finished, the resulting tip is rinsed in water and isopropanol.

Obtained Ni tips that are satisfactory for STM are mounted into the same tip holding units as ordinary tungsten tips, as depicted in Fig. 2.1 (b). However, due to the comparatively high elasticity of the material, Ni tips cannot be fixed in the holding units mechanically by wedging them in the corresponding opening. Instead, Ni tips are mounted by gluing them in position with silver conductive paste. Once transferred into the UHV system, Ni tips are cleaned by field emission according to the same procedure as is done in case of tungsten tips.

5.2. Characterization of the electromagnet

Immediately before a spin-sensitive transport experiment, the ferromagnetic Ni tips are magnetized *in situ*. For this purpose, an electromagnetic coil constructed by Sven Just [33] is used inside the UHV system. The electromagnet, as depicted in Fig. 5.5 (a), consists of

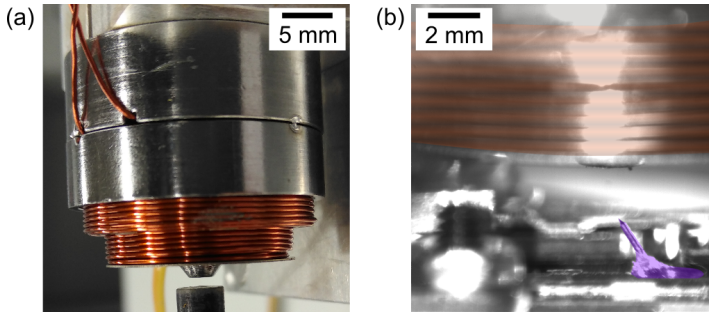


Fig. 5.5.: Photographs of the electromagnet used for *in situ* magnetization of Ni tips. **(a)** Electromagnet as it is characterized in ambient conditions. The copper wire is wound around a ferrite core with ~ 500 turns in total. The current is driven through the ends of the wire to apply the magnetic field. The apex of the ferrite core is seen sticking out of the coil. **(b)** Color-shaded photograph of the setup in UHV used for tip magnetization. Being held by a manipulator, the electromagnet is situated above the STM with its radial axis pointing orthogonally to the sample plane. As indicated by the purple color, the Ni tip is positioned inside the tip transfer shuttle ~ 2 mm below the ferrite core apex.

~ 500 turns of copper wire around a ferrite core. The apex of the ferrite core sticks out of the cylindrical coil and is brought close to the Ni tips for magnetization. An exemplary color-shaded photograph of the magnetization setup is presented in Fig. 5.5 (b), where the ferrite core has a distance of $z \approx 2$ mm to the tip. The cylindrical coil is held above the STM by a manipulator which also provides electrical contacts to the copper wire. In this position, the radial axis of the magnet is directed orthogonally to the sample plane.

The corresponding relation between the current through the copper wire and the resulting magnetic field, as measured in ambient conditions by a Hall probe at a distance of $z = 1$ mm from the core apex, is presented in Fig. 5.6 (a). At this distance, a maximum current of 5.4 A through the copper wire results in a magnetic field of > 300 mT. The spatial distribution of the magnetic field strength close to the coil is shown in Fig. 5.6 (b) and (c). For all experimentally relevant distances up to $z = 3$ mm along the radial axis of the coil, the magnetic field is ≥ 150 mT in strength. The magnetic field also decays laterally from the radial axis, with half of its strength reached at a displacement of $y \approx 3$ mm. Repeated use of the electromagnet is observed to lead to significant resistive heating of the coil. Three subsequent uses, each involving a current ramp to 5.4 A within 15 s, result in a temperature of $> 60^\circ\text{C}$ at the outer windings of the copper wire. When operated in the UHV system, this results in a temporary increase in pressure.

When the ferromagnetic tip is magnetized in the experiment as depicted in Fig. 5.5 (b), a current of 2 A is driven through the electromagnet. During the procedure, the apex of the

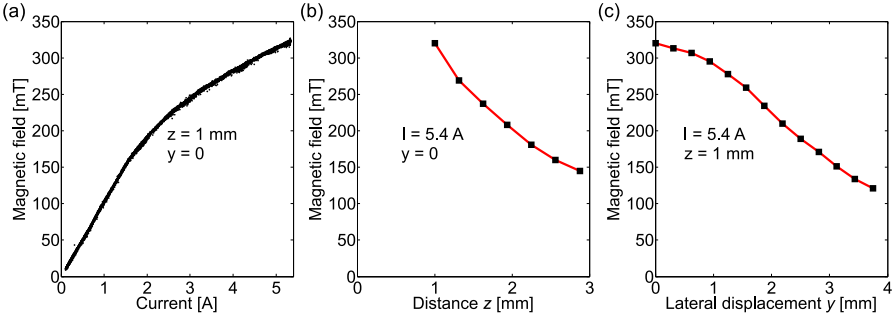


Fig. 5.6.: Characterization of the electromagnetic coil in ambient conditions. **(a)** Magnetic field as a function of current as measured by a Hall probe at a distance of $z = 1 \text{ mm}$ from the apex of the ferrite core. **(b)** Decay of the magnetic field strength at a constant current with increasing distance z along the radial axis of the coil. **(c)** Lateral distribution of the stray magnetic field measured as a function of displacement y . The applied current $I = 5.4 \text{ A}$ and the longitudinal distance from the ferrite core $z = 1 \text{ mm}$ are kept constant.

ferrite core is situated directly above the single Ni tip at a distance of $z \approx 2 \text{ mm}$, with no sample in between. The corresponding magnetic field at the tip position is estimated to $\sim 120 \text{ mT}$. It is noted that using these parameters in this setup, the force acting on the tip is strong enough to move the tip holder. For higher magnetic field strengths, it is frequently observed that the tip holder is detached from the nanopositioner entirely and caught by the ferrite core. To stabilize the procedure, the cylindrical tip holder is kept in the tip transfer shuttle where it is fixed by a spring during magnetization. After magnetizing the Ni tip according to this scheme, the investigated sample is inserted into the STM to perform the spin-sensitive measurements.

5.3. Measurement of the intrinsic TSS spin polarization

The intrinsic spin polarization of the TSS of a 3D TI that constitutes the helical spin texture of the Dirac cone is a property that is difficult to access in transport experiments. While the spin polarization of TSS can be revealed conveniently by means of ARPES [15, 84, 108–110], its manifestation in charge transport is obfuscated by various factors. As the propagation of charge carriers in a defined direction is forced by the injection of a current, the helicity of the TSS causes a majority spin polarization of the current. In principle, the electrical detection of the underlying intrinsic spin polarization of the TSS is then enabled by performing a multi-terminal potentiometric measurement with ferromagnetic (FM) contacts [103, 104, 111–117]. However, parasitic contributions to charge transport that enable a portion of the total current to be carried by trivial electronic states can cover the influence of the TSS. Furthermore,

experiments that require the *ex situ* deposition of contacts as part of the device preparation allow the introduction of contaminations on the surface, which in turn can modify the electronic structure of the TI and consequently reduce its spin polarization.

In this work, two BST thin films of different composition were investigated regarding the intrinsic spin polarization of charge carriers. The small TI film thickness of ~ 10 nm allows to limit the contribution of trivial electronic states to transport due to the small amount of charge carriers in the bulk [118]. By using the four-point STM for *in situ* electrical characterization, it is possible to prevent contaminations of the pristine sample surface and investigate the TSS transport properties in their as-grown state. To ensure this condition, the TI samples are transferred into the STM chamber immediately after growth by means of a UHV suitcase with a base pressure of $\sim 2 \cdot 10^{-10}$ mbar. For this purpose, the UHV suitcase is prepared beforehand as described in appendix C.3.

5.3.1. Sample conductivity

As outlined in section 4.2, the two investigated BST compounds have different positions of the Fermi level E_F in the band gap. It is therefore expected that the two samples differ in their electrical properties. The conductivity of the thin films is determined in distance-dependent four-point resistance measurements on the micrometer scale, as presented in Fig. 5.7. Three of the STM tips are kept in linear alignment with a spacing of $s = 50 \mu\text{m}$. The remaining current-injecting tip with a distance x to the neighboring voltage probe is moved collinearly in between electrical measurements. As is expected for thin films of 10 nm thickness, the acquired resistance exhibits two-dimensional behavior for both sets of measurements. This is confirmed by the correspondence with the appropriate model function given by Eq. 2.20, which is represented by red curves in Fig. 5.7. The corresponding 2D conductivities are determined to $\sigma_{2D} = (0.41 \pm 0.01)$ mS for the $(\text{Bi}_{0.53}\text{Sb}_{0.47})_2\text{Te}_3$ film and $\sigma_{2D} = (2.86 \pm 0.01)$ mS in case of $(\text{Bi}_{0.06}\text{Sb}_{0.94})_2\text{Te}_3$.

Upon comparison of the obtained conductivity values, it is apparent that the conductivity of the Sb-rich thin film is higher than that of the other compound by a factor of ~ 7 . This seems counterintuitive at first sight, since the number of charge carriers occupying the TSS in the $(\text{Bi}_{0.06}\text{Sb}_{0.94})_2\text{Te}_3$ film is expected to be lower due to the position of the Fermi level $E_F \approx 0$ (Fig. 4.4 (b)). Using the density of states $D(E) = E/(2\pi(\hbar v_F)^2)$ and the Fermi distribution functions $f_n(E)$, $f_p(E)$ for electrons and holes, the total TSS charge carrier density at room temperature

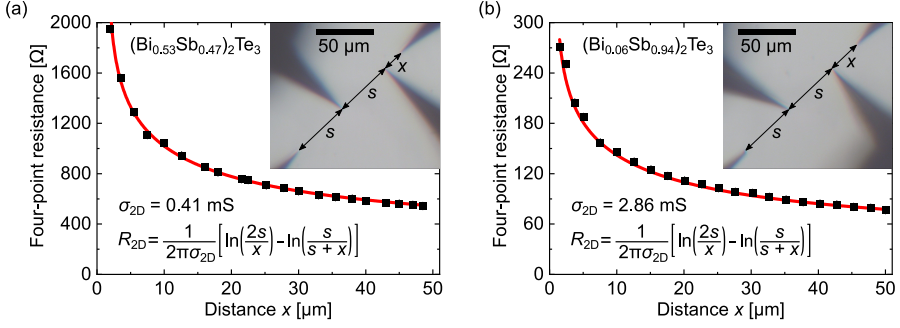


Fig. 5.7.: Measurement of the conductivity of two different BST samples on the micrometer scale. (a) Four-point resistance as a function of inter-tip distance x on the surface of a $(\text{Bi}_{0.53}\text{Sb}_{0.47})_2\text{Te}_3$ thin film. As expected from a film of 10 nm thickness, the resistance shows 2D behavior. Using the related resistance model function (Eq. 2.20), the conductivity is determined to $\sigma_{2\text{D}} = (0.41 \pm 0.01)$ mS. (b) Corresponding distance-dependent four-point resistance measurement on a $(\text{Bi}_{0.06}\text{Sb}_{0.94})_2\text{Te}_3$ thin film of the same thickness. The film conductivity is found as $\sigma_{2\text{D}} = (2.86 \pm 0.01)$ mS.

can be determined by

$$n_{\text{tot}} = n_{\text{TSS}} + p_{\text{TSS}} = \int_0^{\infty} dE D(E) [f_n(E) + f_p(E)] \quad (5.1)$$

$$= \frac{1}{2\pi(\hbar v_F)^2} \int_0^{\infty} dE E \left[\left(1 + \exp\left(\frac{E - E_F}{k_B T}\right) \right)^{-1} + \left(1 + \exp\left(\frac{E + E_F}{k_B T}\right) \right)^{-1} \right], \quad (5.2)$$

with v_F being the Fermi velocity defining the slope of the Dirac cone. Using their respective Fermi levels $E_F = 0$ and $E_F = 250$ meV in this expression, the charge carrier densities of the two thin films are determined to $n_{\text{tot}} \approx 2.8 \cdot 10^{11} \text{ cm}^{-2}$ and $n_{\text{tot}} \approx 4 \cdot 10^{12} \text{ cm}^{-2}$, respectively.

With the conductivity being a product of charge carrier density and carrier mobility, the observed discrepancy could in principle be explained either by an increased contribution of bulk states to transport or by an increased TSS mobility in the $(\text{Bi}_{0.06}\text{Sb}_{0.94})_2\text{Te}_3$ film. The former can be excluded as a possibility by the following estimation. The charge carrier density in the interior of the film arising from bulk states is determined to $n_{\text{film}} = 3 \cdot 10^{11} \text{ cm}^{-2}$ using the Boltzmann approximation in conjunction with the known difference of 50 meV between the Fermi level and the bulk bands [100]. Due to the exceptionally low mobility of bulk states $\mu_{\text{film}} < 2 \text{ cm}^2/\text{Vs}$ at room temperature [101], the contribution of these bulk carriers to the conductivity of the TI is insignificant. Conclusively, the high conductivity of the $(\text{Bi}_{0.06}\text{Sb}_{0.94})_2\text{Te}_3$ film is attributed to an increased TSS mobility compared to the BST system with lower Sb percentage. Under the assumption that the mobility and position of the Fermi level of the bottom TSS are equal to those of the top TSS, the mobility of the Sb-rich thin film is estimated to $\mu = \frac{\sigma_{2\text{D}}/2}{e(n_{\text{TSS}} + p_{\text{TSS}})} \approx 32,000 \text{ cm}^2/\text{Vs}$ according to the Drude formalism. This is a

significant increase compared to the mobility value of $\mu \approx 580 \text{ cm}^2/\text{Vs}$ that is determined for the $(\text{Bi}_{0.53}\text{Sb}_{0.47})_2\text{Te}_3$ system [101]. A sharp increase of TSS carrier mobility is known to occur in TI systems featuring a Dirac point close to the Fermi level [93, 104, 119].

5.3.2. Principle of spin voltage detection

The spin polarization of charge carriers involved in transport can be detected using a FM contact as a voltage probe [120, 121]. In ferromagnetic materials, there is a substantial imbalance in the occupation of the two spin subbands. According to the Stoner model, the density of states at the Fermi level $D(E_F)$ of one spin type is larger than that of the other, such that there is a majority and a minority spin type in equilibrium, as illustrated schematically in Fig. 5.8.

Due to the different occupation of the spin subbands, an imbalance in the conductance corresponding to both spin types exists, as $G \propto D(E)$. Therefore, a material with finite magnetic polarization can be used as a spin-sensitive probe in transport experiments. The effective magnetic polarization of the probe is given by [122]

$$P_{\text{FM}} = \frac{G_{\uparrow} - G_{\downarrow}}{G_{\uparrow} + G_{\downarrow}}. \quad (5.3)$$

When an ideal FM ($|P_{\text{FM}}| = 1$) is in contact to a conducting medium with a nonzero carrier spin polarization and is used as a voltage probe in a high-impedance circuit, there is no current flow and the chemical potential of the FM probe aligns with that of the majority spin subband in the conducting medium [123]. The measured voltage difference compared to a non-magnetic (NM) probe is proportional to the spin imbalance in the conducting medium.

In the context of the performed four-point resistance measurements on the surface of the investigated TI, this voltage difference V_s is called *spin voltage*. Since the spin imbalance in the TI thin film, representing the conducting medium, is provided by the spin-momentum locking of the TSS, there is a direct relation of the injected charge current I to the spin voltage V_s measured by the FM Ni tip.

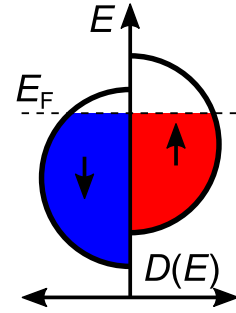


Fig. 5.8.: Schematic representation of a ferromagnet in the Stoner model. Due to exchange interaction, the density of states of the FM is split into two subbands which are shifted relative to each other in energy, such that $D_{\uparrow}(E_F) \neq D_{\downarrow}(E_F)$. Therefore, there is a majority and a minority spin at the Fermi level. As a result of the imbalance, the FM is more sensitive the majority spin type when it is used as a voltage probe.

In the experiment, the current is injected by two NM tungsten tips on the surface of the TI film. As a bias voltage is applied between the two tips, a shift $\vec{\Delta k}$ of the Fermi circle from its equilibrium position in reciprocal space is introduced in the transport direction. This results in a current density

$$\vec{j} = -e \int \frac{d^2 k}{(2\pi)^2} \vec{v}(\vec{k}) f(\vec{k}) \quad (5.4)$$

$$= -\frac{e}{(2\pi)^2} \int d_x d_y v_F (\cos \phi \vec{e}_x + \sin \phi \vec{e}_y) \left[f_0(\vec{k}) + \vec{\Delta k} \cdot \vec{\nabla}_k f_0(\vec{k}) \right] \quad (5.5)$$

where the non-equilibrium Fermi distribution function $f(\vec{k})$ is expressed by the Fermi circle shift $\vec{\Delta k}$ according to the Boltzmann transport equation. $f_0(\vec{k})$ represents the equilibrium Fermi distribution and the carrier velocity $\vec{v}(\vec{k})$ is given by the Fermi velocity v_F that is constant around the Fermi circle.

Assuming $\vec{\Delta k} \parallel \vec{e}_x$, i.e. $\Delta k = \Delta k_x$ without the loss of generality, a transformation to polar coordinates (k, ϕ) in reciprocal space results in

$$\vec{j} = -\frac{e v_F}{(2\pi)^2} \int_0^{2\pi} d\phi (\cos \phi \vec{e}_x + \sin \phi \vec{e}_y) \int_0^\infty dk k \Delta k_x \frac{df_0}{dk_x} \quad (5.6)$$

$$= \frac{e v_F}{(2\pi)^2} \int_0^{2\pi} d\phi (\cos \phi \vec{e}_x + \sin \phi \vec{e}_y) \int_0^\infty dk k \Delta k_x \frac{\exp\left(\frac{\hbar v_F k - E_F}{k_B T}\right)}{\left(1 + \exp\left(\frac{\hbar v_F k - E_F}{k_B T}\right)\right)^2} \frac{\hbar v_F}{k_B T} \frac{k_x}{k} \quad (5.7)$$

$$= \frac{e v_F}{(2\pi)^2} \int_0^{2\pi} d\phi (\cos \phi \vec{e}_x + \sin \phi \vec{e}_y) \int_0^\infty dk k \cos \phi \Delta k_x \frac{\exp\left(\frac{\hbar v_F k - E_F}{k_B T}\right)}{\left(1 + \exp\left(\frac{\hbar v_F k - E_F}{k_B T}\right)\right)^2} \frac{\hbar v_F}{k_B T}, \quad (5.8)$$

where the dispersion relation $E(k) = \hbar v_F k$ of the TSS is used.

Substituting $u = \frac{\hbar v_F k - E_F}{k_B T}$ leads to

$$\vec{j} = \frac{e v_F \Delta k_x}{(2\pi)^2} \int_0^{2\pi} d\phi (\cos^2 \phi \vec{e}_x + \sin \phi \cos \phi \vec{e}_y) \int_{-E_F/k_B T}^\infty du \left(\frac{E_F}{\hbar v_F} + u \frac{k_B T}{\hbar v_F} \right) \frac{\exp(u)}{(1 + \exp(u))^2} \quad (5.9)$$

$$= \frac{e v_F \Delta k_x}{4\pi} \vec{e}_x \left[k_F + \frac{k_B T}{\hbar v_F} \ln \left(1 + \exp\left(\frac{-E_F}{k_B T}\right) \right) \right]. \quad (5.10)$$

This expression establishes the direct relation between the induced current density j and the shift of the Fermi circle Δk_x at room temperature. To determine the spin chemical potential that is measured as a consequence of the intrinsic spin polarization p of the TSS carrying the current j , it is necessary to relate the shift of the Fermi circle Δk_x to the measured potential. Due to the linear dispersion relation of the TSS, the shift in momentum Δk_x is translated to a shift $\hbar v_F \Delta k_x \cos \phi$ of the electrochemical potential of all states at the original Fermi level. As a result of the nonzero intrinsic spin polarization p of the TSS, as indicated by the arrows in Fig. 5.9 (a), this leads to a shift between the average electrochemical potentials of spin-up

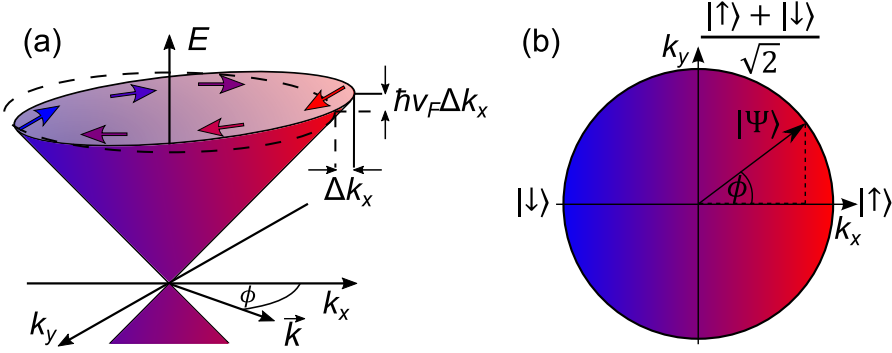


Fig. 5.9.: (a) Sketch of the tilt of the Dirac cone as an effect of applied bias. With the induction of a current j in x -direction, a shift Δk_x of the Fermi circle is caused according to the Boltzmann transport equation. Following the linear dispersion of the TSS, the electrochemical potential is shifted by $\hbar v_F \Delta k_x \cos \phi$, resulting in a shift of the average electrochemical potential of spin-up(-down) carriers due to the relation between spin and momentum. (b) Schematic representation of the TSS helicity in reciprocal space for ideal intrinsic spin polarization $p = 1$. The orientation of charge carrier spin is perpendicular to their corresponding momentum $\hbar \vec{k}$ and the surface normal around the Fermi circle. For each \vec{k} in the Dirac cone, the spin wave function of charge carriers is given by the pure state $|\Psi\rangle = \cos \frac{\phi}{2} |\uparrow\rangle + \sin \frac{\phi}{2} |\downarrow\rangle$. The momentum-dependent probability of finding a charge carrier in the spin-up(-down) state is determined by the projection $|\langle \uparrow | \Psi \rangle|^2$ ($|\langle \downarrow | \Psi \rangle|^2$).

and spin-down states. Consequently, a spin-split local electrochemical potential, i.e. a spin imbalance of charge carriers, is induced by the shift in reciprocal space Δk_x .

The resulting spin voltage V_s that is measured by a FM voltage probe is proportional to the shifted average electrochemical potential of the FM majority spin state. The proportionality is determined by P_{FM} , such that for $P_{\text{FM}} = 1(-1)$, V_s is equal to the average electrochemical potential of the spin-up(-down) state. For general P_{FM} , V_s is obtained by the interface condition at the FM contact requiring that there is no net current flow between the FM probe and the TI surface [124]

$$\int_0^{2\pi} d\phi [G_{\uparrow} |\langle \uparrow | \Psi \rangle|^2 + G_{\downarrow} |\langle \downarrow | \Psi \rangle|^2] \left(V_s - \frac{\hbar v_F}{e} \Delta k_x \cos \phi \right) = 0, \quad (5.11)$$

where conductance values G_{\uparrow} and G_{\downarrow} of the two spin subbands constituting P_{FM} are multiplied by the probability to find a charge carrier in the respective spin state, with $|\Psi\rangle$ being the spin wave function of charge carriers. The expression in the second pair of brackets is the local difference between the spin potential acquired by the FM contact and the tilted Fermi circle in reciprocal space. The spin wave function describes the spin-momentum relation along the Dirac cone and for a spin polarization p of 100% is given by the pure state $|\Psi\rangle = \cos \frac{\phi}{2} |\uparrow\rangle + \sin \frac{\phi}{2} |\downarrow\rangle$, as depicted in Fig. 5.9 (b). In case of $p = 0$, spin-momentum

locking is absent and the probability to find a charge carrier in the spin-up(-down) state is constant at $\frac{1}{2}$ for all ϕ around the Dirac cone.

For general $0 \leq p < 1$, the spin state of charge carriers cannot be written as a pure state $|\Psi\rangle$ and thus, the charge carrier spin needs to be treated as a statistical ensemble of spin states. The resulting mixed spin state for a given \vec{k} on the Fermi circle is represented by the density operator

$$\hat{\rho} = P_{\Psi} |\Psi\rangle \langle \Psi| + P_{\tilde{\Psi}} |\tilde{\Psi}\rangle \langle \tilde{\Psi}|, \quad (5.12)$$

where $|\tilde{\Psi}\rangle = -\sin\frac{\phi}{2}|\uparrow\rangle + \cos\frac{\phi}{2}|\downarrow\rangle$ is the orthogonal pure state to $|\Psi\rangle$, such that $\langle \tilde{\Psi}|\Psi\rangle = 0$. The intrinsic spin polarization of the TSS p determines the probabilities $P_{\Psi} = \frac{1+p}{2}$ and $P_{\tilde{\Psi}} = \frac{1-p}{2}$ of finding a charge carrier in the respective pure spin state. Consequently, $p = 1$ results in all of the carriers in the ensemble being in the pure spin state $|\Psi\rangle$ corresponding to the right-handed helicity of the 3D TI. On the opposite, $p = 0$ represents a fully mixed incoherent superposition with its orthogonal state $|\tilde{\Psi}\rangle$. $p = -1$ in principle corresponds to left-handed helicity around the Fermi circle.

Following Eq. 5.12, the general expression for the density operator of the mixed state is written in the basis of $|\uparrow\rangle$ and $|\downarrow\rangle$ as

$$\hat{\rho} = \begin{pmatrix} \frac{1}{2} - \frac{p}{2} \left(\sin^2 \frac{\phi}{2} - \cos^2 \frac{\phi}{2} \right) & \frac{p}{2} \sin \phi \\ \frac{p}{2} \sin \phi & \frac{1}{2} + \frac{p}{2} \left(\sin^2 \frac{\phi}{2} - \cos^2 \frac{\phi}{2} \right) \end{pmatrix}. \quad (5.13)$$

With the probabilities $\langle \uparrow|\hat{\rho}|\uparrow\rangle$ and $\langle \downarrow|\hat{\rho}|\downarrow\rangle$ of finding a charge carrier of the ensemble in the spin-up and the spin-down state, the interface condition for a voltage probe on the TI surface can be written for arbitrary intrinsic spin polarization $0 \leq p \leq 1$ as

$$\int_0^{2\pi} d\phi \left[G_{\uparrow} \langle \uparrow|\hat{\rho}|\uparrow\rangle + G_{\downarrow} \langle \downarrow|\hat{\rho}|\downarrow\rangle \right] \left(V_s - \frac{\hbar v_F}{e} \Delta k_x \cos \phi \right) = 0, \quad (5.14)$$

which is solved for the spin voltage V_s

$$\int_0^{2\pi} d\phi \left[G_{\uparrow} \left(\frac{1}{2} - \frac{p}{2} \left(\sin^2 \frac{\phi}{2} - \cos^2 \frac{\phi}{2} \right) \right) + G_{\downarrow} \left(\frac{1}{2} + \frac{p}{2} \left(\sin^2 \frac{\phi}{2} - \cos^2 \frac{\phi}{2} \right) \right) \right] \left(V_s - \frac{\hbar v_F}{e} \Delta k_x \cos \phi \right) \quad (5.15)$$

$$= V_s \pi (G_{\uparrow} + G_{\downarrow}) - \frac{\hbar v_F}{e} \Delta k_x \int_0^{2\pi} d\phi \left[G_{\uparrow} \left(-\frac{p}{2} \right) + G_{\downarrow} \frac{p}{2} \right] \cos \phi \left(\sin^2 \frac{\phi}{2} - \cos^2 \frac{\phi}{2} \right) \quad (5.16)$$

$$= V_s \pi (G_{\uparrow} + G_{\downarrow}) - \frac{\hbar v_F}{e} \Delta k_x \frac{p}{2} \pi (G_{\uparrow} - G_{\downarrow}) \stackrel{!}{=} 0 \quad (5.17)$$

$$\Rightarrow V_s = p P_{\text{FM}} \frac{\hbar v_F}{2e} \Delta k_x. \quad (5.18)$$

This term relates the shift Δk_x of the Fermi circle to the spin voltage V_s that is probed by a contact with magnetization P_{FM} through the intrinsic polarization of the TSS p . Using

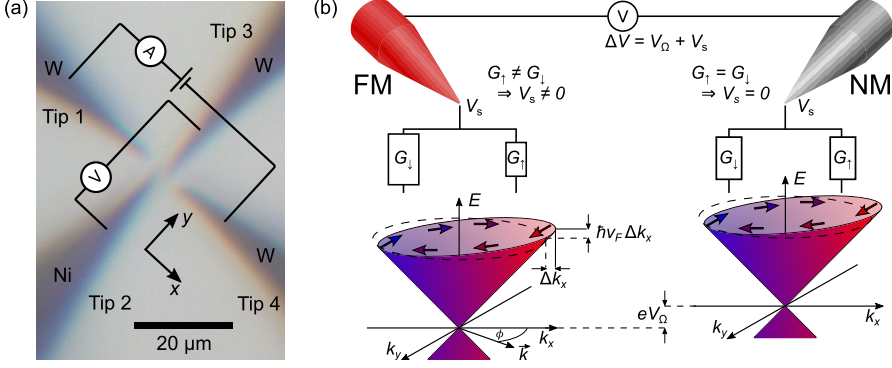


Fig. 5.10.: Measurement principle of the spin-dependent potential with STM tips. **(a)** Typical transport measurement setup as seen by the optical microscope. With the four linearly arranged STM tips in contact to the sample surface acting as electrical probes, a current is induced between the outer two tips, while the resulting potential difference is measured between the inner ones. **(b)** Due to the helical nature of the TSS, the orientation of charge carrier spin is perpendicular to their corresponding momentum $\hbar\vec{k}$ and the surface normal, with the intrinsic TSS spin polarization p being the degree of helicity. The electrical contact between a voltage probe and the TI surface can be regarded as two parallel channels with conductances G_\uparrow and G_\downarrow for the two spin orientations. For a finite probe magnetisation ($G_\uparrow \neq G_\downarrow$), the voltage probe acquires a spin-dependent potential V_s , which is given by the interface condition requiring zero current flow (cf. Eq. 5.14). In this sketch, charge transport takes place in k_x -direction and Δk_x denotes the shift of the Fermi circle due to applied bias. Note that the indicated shift in electrochemical potential $\hbar v_F \Delta k_x \cos \phi$ refers to the extremal position $\phi = 0$.

Eq. 5.10, the spin voltage is expressed by the current density j that is induced by the applied bias as

$$V_s = p P_{\text{FM}} \frac{\hbar}{e^2} j \left[k_F + \frac{k_B T}{\hbar v_F} \ln \left(1 + \exp \left(\frac{-E_F}{k_B T} \right) \right) \right]^{-1}. \quad (5.19)$$

In the low temperature limit $E_F \gg k_B T$, this general expression reduces to $V_s = p P_{\text{FM}} \frac{\hbar}{e^2} \frac{1}{k_F} j$, which is usually used in spin voltage investigations [103, 104, 124]. For finite temperatures, with a Fermi level E_F close to the Dirac point, the first term vanishes as $k_F \rightarrow 0$, resulting in

$$V_s = p P_{\text{FM}} \frac{\hbar}{e^2} \left(\frac{\hbar v_F}{k_B T} \frac{1}{\ln 2} \right) j, \quad (5.20)$$

where the term in brackets denotes the effective wave number of thermally excited charge carriers.

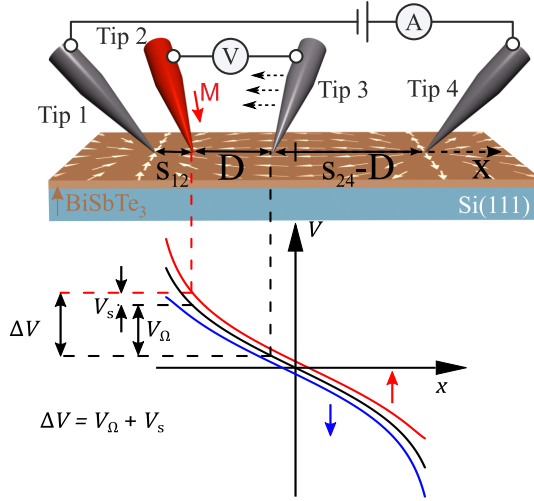


Fig. 5.11.: Sketch of the spin voltage measurement principle in real space. A current that is induced by the outer tips defines the potential along the line of the linear configuration. Due to the equal conductances of the two spin subbands, the NM voltage probe senses the logarithmically-shaped local spin-averaged 2D potential indicated by the black line. In contrast, the magnetized FM tip additionally acquires the electrochemical potential that is spin-split by V_s . The obtained spin signal is larger if the FM probe is placed close to a current-injecting tip due to its proportionality to the current density (Eq. 5.19).

5.3.3. Spin voltage measurement scheme

In the experiment, the four STM tips are arranged linearly as presented in Fig. 5.10 (a), enabling the distance-dependent measurement of V_s on the TI surface. While the outer NM tungsten tips induce the spin-polarized charge current in the TI, the two voltage probes in between – one of which is the FM Ni tip – measure the resulting potential difference.

As illustrated in Fig. 5.10 (b), the electrical contact between the voltage probes and the TI surface is represented by two channels in parallel, one for each spin subband. At their respective position on the TI surface, the voltage probes float to the potential that is created by the voltage drop between the injection tips. The NM tip can only probe the spin-averaged ohmic potential due to its equal conductances for both spin subbands. This is evident from the interface condition in Eq. 5.14 yielding V_s for $G_1 = G_1$. In contrast, the FM tip with its nonzero effective spin sensitivity P_{FM} probes the additional spin-dependent potential component V_s according to Eq. 5.19, with j representing the local current density at the position of the FM tip.

During the distance-dependent four-point resistance measurement, the two current-injecting tips as well as the magnetized voltage-probing Ni tip are kept at fixed positions, such that the local current density $j(x)$ at the FM tip that is dictating V_s is constant. The remaining NM voltage probe is moved in x -direction as defined by the symmetry line of the tip arrangement (Fig. 5.10 (b)). A real space representation of the measurement scheme is depicted in Fig. 5.11. While the NM tip only probes the spin-averaged ohmic potential denoted by the black curve, the FM tip acquires the spin-split potential. The measured voltage difference between the two tips therefore contains an ohmic component V_Ω and the spin-dependent component V_s , since only one of the two voltage probes is sensitive to the spin chemical potential. Due to spin-momentum locking, the reversal of the current direction in a four-point measurement leads to a change of the sign in V_s . However, as the sign of the ohmic component V_Ω changes as well, the spin signal cannot be extracted from the total measured voltage difference in a static tip configuration by only reversing the current. The voltage difference is given by

$$\Delta V = V_\Omega + V_s \quad (5.21)$$

$$= \frac{I}{2\pi\sigma_{2D}} \left[\ln\left(\frac{s_{24}}{s_{12}}\right) - \ln\left(\frac{s_{24}-D}{s_{12}+D}\right) \right] + V_s, \quad (5.22)$$

where the ohmic component is inferred from the 2D resistance (Eq. 2.20) corresponding to the linear tip geometry. The distance D between the two voltage probes as well as the other inter-tip distances s_{12} and s_{24} are indicated in Fig. 5.11.

5.3.4. Distance-dependent four-point measurements

Apart from the material parameters p , v_F and P_{FM} , the spin voltage in Eq. 5.19 depends on the local current density j at the position of the FM probe, which is given by the tip geometry as $j = \frac{I}{2\pi} \left(\frac{1}{s_{12}} + \frac{1}{s_{24}} \right)$. Consequently, the determination of the spin signal in the transport measurements is limited by the uncertainty of the four-point resistance originating from the mispositioning of STM tips on the TI surface. The resolution of the optical microscope is too low to detect the spin signal. Even when assuming an optimistic positioning error of ± 250 nm, the resulting uncertainty of the ohmic resistance component would amount to $\delta R_\Omega \approx 8 \Omega$, as estimated from Eq. 5.22. This estimate is approximately the same magnitude as the spin-dependent signal. Furthermore, the uncertainty of the ohmic component depends on the local slope of the electric potential and therefore scales with the current density with $dR_\Omega/dx \propto j(x)$, just as the spin signal itself. This means that the problem of the resistance uncertainty obfuscating the spin signal cannot be solved by a sophisticated tip arrangement tuning the local potential slope. The only way to reduce the uncertainty of the measured resistance is to reduce the uncertainty of tip positions. To resolve the spin voltage in the experiment, it is therefore required to use the positioning method described in chapter 3.

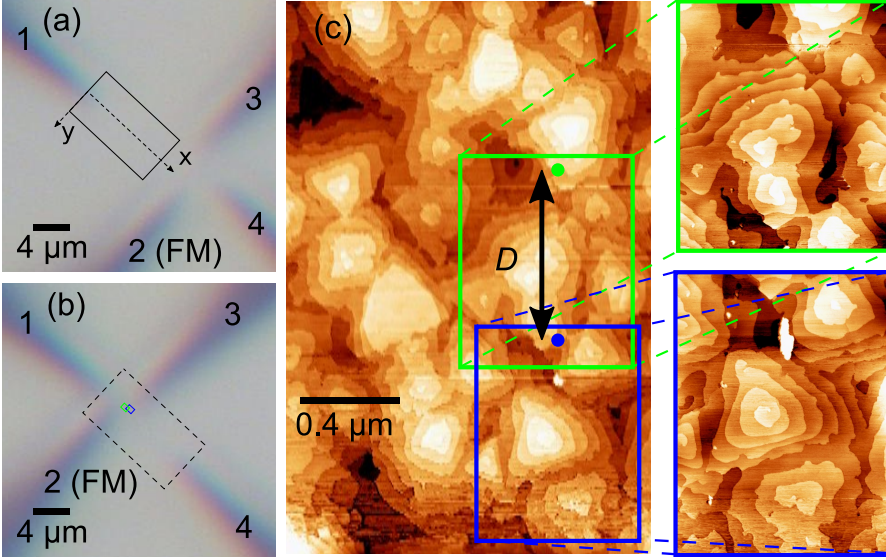


Fig. 5.12.: Exemplary measurement procedure based on STM scans used for spin-sensitive transport measurements. **(a)** Using one of the STM tips, a $4\mu\text{m} \times 10\mu\text{m}$ sized area of the TI surface that is chosen for the transport measurements is imaged. **(b)** After acquisition of the overview scan, all four tips are moved close to their target positions to perform small scans. **(c)** Using the overview scan as a reference map, all tips are navigated to their desired configuration. Each tip position is known from recognition of topographic structures from small STM scans. In between subsequent resistance measurements, the inter-tip distance D is varied by repositioning the NM voltage probe.

Figure 5.12 illustrates a representative measurement procedure for the determination of the spin voltage. Using the positioning method based on STM scans with each tip, the tips are positioned linearly along the slow scan axis of the overview STM scan. While the current-injecting tips are positioned at a distance of $\sim 7\mu\text{m}$, the distance between the two voltage probes D is varied down to the nanometer scale by moving the NM voltage-probing tip in tunneling contact in between subsequent resistance measurements.

Experimentally, the spin voltage V_s is obtained in the four-point measurement in the limit of vanishing inter-tip distance $D \rightarrow 0$. The four-point resistance $R_{4P} = \frac{\Delta V}{I}$ is inferred from $I - V$ characteristics with an induced current of $I \approx 50\mu\text{A}$ at various D for opposite FM tip magnetization directions. From the distance-dependent resistance, the constant spin contribution containing the spin polarization of the TSS is determined by the interpolation

$$R_s = \frac{\Delta V(D \rightarrow 0)}{I} = pP_{\text{FM}} \frac{h}{e^2} \frac{1}{2\pi} \left(\frac{1}{s_{12}} + \frac{1}{s_{24}} \right) \left[k_F + \frac{k_B T}{\hbar v_F} \ln \left(1 + \exp \left(\frac{-E_F}{k_B T} \right) \right) \right]^{-1}. \quad (5.23)$$

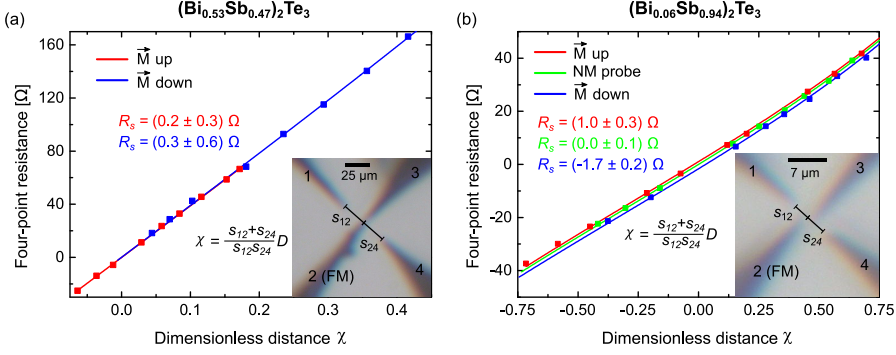


Fig. 5.13.: Results of the spin voltage measurement in the symmetric configuration ($s_{12} = s_{24}$) for two BST samples of different composition. The respective tip configuration is depicted in the insets. The spin-dependent four-point resistance is measured as a function of distance between the voltage-probing tips D . To compare the different sets of measurements with different s_{12} and s_{24} , the resistance is plotted versus a dimensionless inter-tip distance χ . Data points in red and blue correspond to measurements with opposite magnetization directions of the FM tip. **(a)** In case of the $(\text{Bi}_{0.53}\text{Sb}_{0.47})_2\text{Te}_3$ film, the spin signal R_s , as obtained from fits of the resistance model (Eq. 5.25), is zero within measurement errors. **(b)** As seen from the offset in the fit curves, a finite R_s is determined from corresponding measurements on the $(\text{Bi}_{0.06}\text{Sb}_{0.94})_2\text{Te}_3$ film. A control measurement with only NM tips, represented by the green data points, yields $R_s = 0$, as expected.

Measurements in symmetric probe configuration

The distance-dependent measurements according to the described scheme are performed on two BST films of 10 nm film thickness. The measured four-point resistance as a function of distance between the voltage-probing tips is presented in Fig. 5.13 for both samples in a symmetric tip configuration.

In this configuration, the voltage-probing FM tip is positioned in between the current-inducing tips with $s_{12} = s_{24}$. This arrangement is useful for minimizing errors arising from mispositioning of the tips due to the small potential slope in the middle. Red and blue data points correspond to sets of measurements for which the FM tips have been magnetized oppositely beforehand. On one of the investigated BST samples, the graph also includes a control measurement with only NM tips represented by green data points. To compare the data sets, each with different distances s_{12} and s_{24} , to each other, the varied inter-tip distance D is scaled to a dimensionless quantity

$$\chi = D \frac{s_{12} + s_{24}}{s_{12}s_{24}}, \quad (5.24)$$

which results in resistance slopes $\frac{dR}{d\chi}$ that are independent of the parameters s_{12} and s_{24} , as

shown in appendix A.2. For each of the measurement sets in Fig. 5.13, a fit of the model function

$$R = \frac{1}{2\pi\sigma_{2D}} \left[\ln\left(\frac{s_{24}}{s_{12}}\right) - \ln\left(\frac{s_{24}-D}{s_{12}+D}\right) \right] + R_s \quad (5.25)$$

is performed to the measured resistance. The model parameters of s_{12} and s_{24} are determined from the distances of the tip positions in the overview STM scan. The sample conductivity σ_{2D} is known from electrical measurements on the micrometer scale (Fig. 5.7).

In case of the $(\text{Bi}_{0.53}\text{Sb}_{0.47})_2\text{Te}_3$ film, no resistance offset R_s is obtained within the error margins for either magnetization direction, as evident from the fit results with $R_s = (0.2 \pm 0.3)\Omega$ and $R_s = (0.3 \pm 0.6)\Omega$ in Fig. 5.13 (a). In contrast, distance-dependent measurements on the $(\text{Bi}_{0.06}\text{Sb}_{0.94})_2\text{Te}_3$ film in the symmetric tip configuration with $s_{12} = s_{24} \approx 3.5\mu\text{m}$ yield a nonzero spin resistance with opposite sign for the two FM magnetization directions. As can be inferred from the fits of the model function in Eq. 5.25, denoted by the lines of corresponding color in Fig. 5.13 (b), the resistance curves are offset to each other by a finite intercept. The model fits for the two opposite tip magnetization directions result in $R_s = (1.0 \pm 0.3)\Omega$ and $R_s = (-1.7 \pm 0.2)\Omega$, respectively. The complementary control measurement that is performed according to the same measurement scheme, but with four NM tips, yields $R_s = (0.0 \pm 0.1)\Omega$, as is expected according to Eq. 5.23 with $P_{\text{FM}} = 0$.

Evidently, the four-point measurements on the $(\text{Bi}_{0.06}\text{Sb}_{0.94})_2\text{Te}_3$ sample reveal a spin signal at $D \rightarrow 0$, while the $(\text{Bi}_{0.53}\text{Sb}_{0.47})_2\text{Te}_3$ film exhibits no spin-dependent resistance offset within the measurement errors. Considering the material parameters of the two BST films, this result is not surprising. According to Eq. 5.23, the spin-dependent R_s signal depends on the inverse of k_F , which is determined by the position of the Fermi level in the Dirac cone of the BST system. While the Fermi level in the Sb-rich composition is known to be located at the Dirac point from ARPES [100] (Fig. 4.4 (b)), such that $E_F = 0$ and thus $k_F = 0$, the Fermi wave number of the $(\text{Bi}_{0.53}\text{Sb}_{0.47})_2\text{Te}_3$ system is larger with $k_F \approx 0.07\text{\AA}^{-1}$ [101]. Therefore, the room temperature spin resistance R_s is expected to be approximately 10 times smaller than that of the Sb-rich TI film. Using $k_F \approx 0.07\text{\AA}^{-1}$, the expected resistance offset of a perfectly polarized TSS would amount to $R_s \approx 0.2\Omega$, which is smaller than the measurement error. Regarding TI samples of different materials or doping levels, the most pronounced spin-dependent signal in these resistance measurements is generally obtained for sample systems with k_F and the bulk carrier contribution being as small as possible.

Measurements in high current density configuration

While the distance-dependent resistance measurements on the surface of the $(\text{Bi}_{0.06}\text{Sb}_{0.94})_2\text{Te}_3$ film reveal a finite spin resistance with reversed sign for opposite magnetization direction,

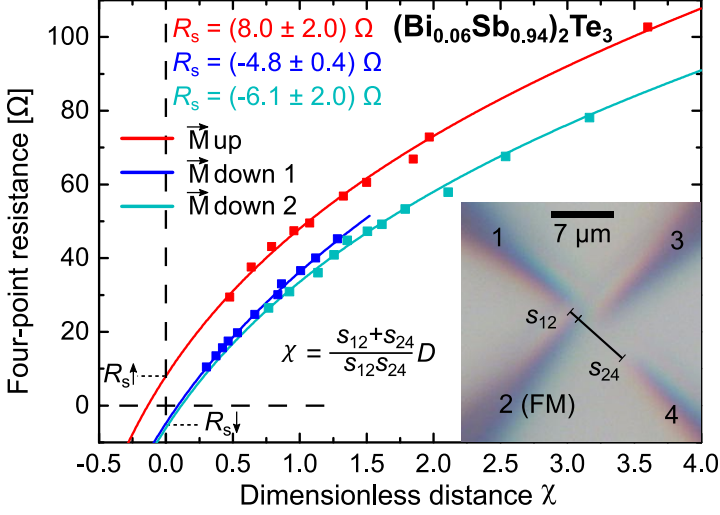


Fig. 5.14.: Results of the spin voltage measurement in the high current density configuration. The respective tip arrangement is shown in the inset. In the respective tip arrangement, which is depicted in the inset with constant $s_{12} \approx 400\text{nm}$ and $s_{24} \approx 7\mu\text{m}$, the spin-dependent four-point resistance is measured under variation of the distance between the voltage-probing tips D . To facilitate the comparison between the measurement sets, D is translated to the dimensionless distance $\chi(D)$. The four-point resistances acquired with reversed FM magnetization directions are denoted by red and blue/cyan data points, respectively. Fits of the underlying resistance model (Eq. 5.25) are shown as lines of corresponding color.

the magnitude of the spin-dependent signal is rather small. The magnitude of $R_s \propto j/I$ can be enhanced by using a probe arrangement with the FM tip placed in a position of high current density. Following from Eq. 5.23, reducing the distance s_{12} between the FM tip and its neighboring current-injecting tip leads to a more pronounced spin-splitting of the chemical potential, as sketched in Fig. 5.11.

In this high current density configuration, with $s_{12} \approx 400\text{nm}$, the four-point resistance measurements under variation of D are repeated for the $(\text{Bi}_{0.06}\text{Sb}_{0.94})_2\text{Te}_3$ sample. Figure 5.14 shows the corresponding measurement results obtained with different FM magnetization directions. As seen from the fits of the model function (Eq. 5.25) to the three data sets, clearly pronounced offsets are found between the resistance curves. The spin resistances obtained at $D \rightarrow 0$ are determined to $R_s = (8 \pm 2)\Omega$ for one FM magnetization direction and $R_s = (-4.8 \pm 0.4)\Omega$ and $R_s = (-6 \pm 2)\Omega$ for the opposite one. Compared to the symmetric configuration in Fig. 5.13 (b), the spin-dependent signal is larger by a factor of ~ 5 , as expected from the corresponding increase of the local current density $j(s_{12}, s_{24})$.

5.3.5. Determination of the TSS spin polarization

The spin-dependent resistance offset R_s that is obtained experimentally from the distance-dependent four-point measurement scheme comprises parameters that are specific to the measurement configuration (Eq. 5.23). To access the underlying intrinsic spin polarization p of the TSS that causes the spin-splitting of the electrochemical potential in the experiment, a configuration invariant offset parameter

$$S = R_s / \left(\frac{1}{s_{12}} + \frac{1}{s_{24}} \right) = p P_{\text{FM}} \frac{\hbar}{2\pi e^2} \frac{\hbar v_{\text{F}}}{k_{\text{B}} T} \frac{1}{\ln 2} \quad (5.26)$$

only depending on intrinsic quantities is defined based on Eq. 5.20, with the constant inter-tip distances inferred from the recorded STM scans for each measurement set.

The spin signals obtained for $(\text{Bi}_{0.06}\text{Sb}_{0.94})_2\text{Te}_3$ in Fig. 5.13 (b) correspond to $S = (1.9 \pm 0.5) \Omega\mu\text{m}$ and $S = (-2.9 \pm 0.4) \Omega\mu\text{m}$ for the two respective FM magnetization directions. In the measurements presented in Fig. 5.14, $S = (3.0 \pm 0.8) \Omega\mu\text{m}$, $S = (-2.9 \pm 0.2) \Omega\mu\text{m}$ and $S = (-1.6 \pm 0.5) \Omega\mu\text{m}$ are found.

Being only influenced by material parameters, the determined S originating from the spin-dependent potential are expected to be constant in all measurements, but with inverted signs for opposite FM magnetization. The variance of the absolute values of the observed S is attributed to a variation of P_{FM} , which is influenced by the microscopic details of the FM Ni tip. In the experiment, each set of distance-dependent measurements was performed with a fresh FM tip.

The spin polarization of the TSS is determined from the measured offset parameters S by using the material parameters according to

$$p = \frac{2S}{v_{\text{F}} P_{\text{FM}} / \sqrt{2}} \frac{(2\pi e)^2 k_{\text{B}} T \ln 2}{\hbar^2}, \quad (5.27)$$

where P_{FM} is corrected for an additional geometrical factor of $1/\sqrt{2}$ due to the 45° -inclination of the FM Ni tip defining the magnetization direction with respect to the surface. In the experimental geometry, a fully magnetized FM tip would therefore effectively act with $1/\sqrt{2}$ of its spin detection capacity following from the projection of the magnetization on the surface. Furthermore, the expression in Eq. 5.27 is also corrected by a factor of 2 due to the partial involvement of the bottom TSS in transport. So far, the top TSS was considered as the only transport channel. For the determination of the spin polarization p detected by the FM tip on the TI surface, only the fraction of the current that propagates through the top TSS is relevant. Assuming an equal division of current between the top and the bottom TSS as a first approximation corresponds to the correction factor of 2.

The Fermi velocity $v_F = 3.8 \cdot 10^5$ m/s of the investigated BST film is acquired from ARPES results of a sample with identical atomic composition [100]. As an estimate for the magnetization of the used Ni tip, typical values of $P_{FM} \sim 0.25 - 0.5$ [125–127] are assumed. Using these parameter values in Eq. 5.27, the intrinsic TSS spin polarization of the BST sample is determined to $p \sim 0.3 - 0.6$, with the main source of variation being the value of the tip magnetization. This range is in agreement with results from other transport investigations of the spin voltage [103, 112, 114, 116, 128].

The definition of the spin polarization p observed in charge transport as a result of spin-momentum locking is ambiguous in literature. The quantity p is sometimes defined as the average spin of all charge carriers with a positive group velocity in transport direction [122, 129]. With the spin of charge carriers in the TSS being oriented strictly perpendicular to the momentum at each \vec{k} in reciprocal space, such a momentum averaging over parts of the Fermi circle yields geometrical normalization factors resulting in maximum spin polarization values smaller than 1. For example, the definition of p of Yazyev et al. [129] entails the integration over half the Fermi circle, resulting in a value of $\pi/4$ in case of an ideal spin texture. In the present work, p is defined as the intrinsic spin polarization of the Fermi circle following the definition of the ensemble of spin states in Eq. 5.12 and as such denotes the degree of helicity in the TSS. In this interpretation, the maximum value of p is 1, corresponding to perfect correlation of carrier spin and momentum around the Fermi circle.

Practically, the intrinsic spin polarization p as defined here can be reduced by ~ 0.35 , as shown in ab initio calculations for TI systems, since spin-orbit entanglement effects can disrupt the conservation of the electron spin quantum number [129]. Assuming a presence of spin-orbit entanglement in the investigated $(\text{Bi}_{0.06}\text{Sb}_{0.94})_2\text{Te}_3$ film, the value of $p \sim 0.3 - 0.6$ measured in the distance-dependent four-point resistance experiment is remarkably close to the theoretical limit. Generally, another cause for a reduction of p is an unidentified involvement of trivial bulk states in charge transport severely limiting the magnitude of the spin voltage [104, 112, 123]. With a parallel conduction channel provided by excited bulk states, only a fraction of the total current j is sustained by carriers obeying spin-momentum locking, which proportionally attenuates the spin-dependent signal (Eq. 5.23). In this regard, BST thin film systems as the one investigated here are advantageous as the bulk contribution to the conductivity is insignificant [101, 118].

It is suggested in literature [124, 130] that perceived spin-dependent signals in transport measurements of TI materials can in principle have other causes than the spin polarization of the TSS, such as the bulk Rashba effect or the local Hall effect caused by stray fields of magnetized FM contacts. In the presented measurements based on the four-tip STM, an influence of stray fields from the FM probe can be excluded due to the small dimension of the

tip contact area [103]. While a parallel contribution of the Rasha effect to the spin signal is in principle possible in a TI system [123], the population of the corresponding spin-split bulk states in the interior of the thin film system investigated here is small due to the position of the Fermi level in the band gap and the small film thickness. Moreover, Rashba contributions from charge carriers that are possibly accumulated at the surface due to band bending [131] are excluded as well, since the near-surface bending is insignificant in case of only 10 nm film thickness [101, 118]. The spin signal R_s inferred from the distance-dependent four-point measurements is also larger in magnitude than what is expected from Rashba-split bulk states, which contribute less to spin polarization in transport due to the partial suppression from counteracting Rashba states with opposite helicity [122].

5.4. Effect of magnetic fields in infinite plane samples

In the framework of the spin-sensitive transport measurements, an electromagnet inside the UHV chamber was used above the STM to magnetize the FM tip *in situ*. Intuitively, the question arises whether the magnet can also be used during the electrical investigation to perform magnetotransport measurements.

In measurement geometries using Hall bar structures with lithographic contacts, the application of a magnetic field perpendicular to the sample surface allows direct experimental access to the carrier mobility of investigated samples. Here, it is explored if, using the STM tips as mobile electrical point-contacts, an analogous approach can be found for the case of infinite-plane samples. The following consideration is based on the findings of Buehler et al. on the Hall effect in infinite-plane systems [132, 133].

The injection of a current through point-contacts on the surface of a 2D conducting plate in the presence of a magnetic field constitutes a boundary-value problem which can be solved by the method of Corbino images. With an applied magnetic field B , the Lorentz force acts on the moving charge carriers that constitute the flow of a current. In the case of a point-like current source, the resulting current density is distorted from its usual radial shape at $B = 0$ into a logarithmic spiral described by a Corbino source. In a planar sample with finite dimensions, a current source/sink is mirrored across the edge of the plate by an imaginary source/sink, similar to the method of image charges used in electrostatics. For each of the sources/sinks, a Corbino source (Fig. 5.15) is used to describe the resulting current density, which forms logarithmic spirals under the influence of a perpendicular magnetic field. For an arbitrary configuration of four probes on the conducting plate as seen in Fig. 5.15, where probe 1 and 4 inject a current and probe 2 and 3 are voltage-probing contacts, two imaginary probes (5 and 6) are constructed to satisfy the boundary conditions. The current density of

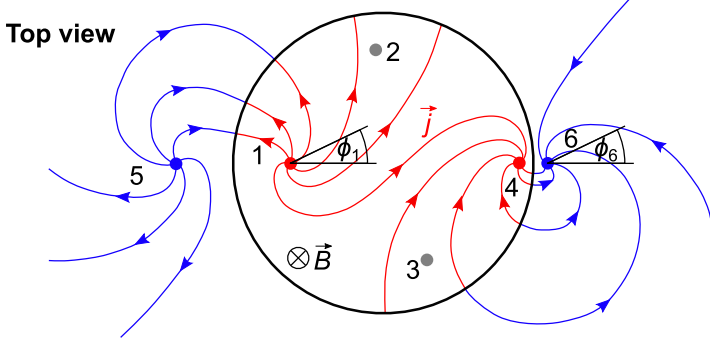


Fig. 5.15.: Sketch of a four-probe measurement for an arbitrary probe configuration on a circular conducting plate with finite radius under the influence of a perpendicular magnetic field. Probes 1 and 4 inject a current through the plate, while probes 2 and 3 serve as voltage-probing contacts. Under the influence of a magnetic field, the point-like current sources are described by logarithmically shaped Corbino sources. To satisfy the boundary conditions of the problem, image sources are constructed across the edge of the conducting plate. The total current density is obtained by the superposition principle. Red/blue lines represent the current density of the real/imaginary sources, respectively.

the four current sources/sinks is expressed by

$$\begin{aligned}\vec{j}_1 &= \frac{I}{2\pi|\vec{r}_1|d} (\vec{e}_{r_1} + A_H B \sigma \vec{e}_{\phi_1}), & \vec{j}_5 &= \frac{I}{2\pi|\vec{r}_5|d} (\vec{e}_{r_5} - A_H B \sigma \vec{e}_{\phi_5}) \\ \vec{j}_3 &= -\frac{I}{2\pi|\vec{r}_3|d} (\vec{e}_{r_3} + A_H B \sigma \vec{e}_{\phi_3}), & \vec{j}_6 &= -\frac{I}{2\pi|\vec{r}_6|d} (\vec{e}_{r_6} - A_H B \sigma \vec{e}_{\phi_6})\end{aligned}$$

where d is the thickness of the plate with conductivity σ , A_H is the Hall constant and $\vec{e}_{r_i}, \vec{e}_{\phi_i}$ are the unity vectors of the polar coordinates with respect to probe i . Using Ohm's law with the included Lorentz force acting on the charge carriers

$$\vec{E} = \frac{1}{\sigma} \vec{j} - A_H (\vec{j} \times \vec{B})$$

allows to find the electric field \vec{E}_i of the four current sources/sinks

$$\begin{aligned}\vec{E}_1 &= \frac{I}{2\pi\sigma|\vec{r}_1|d} (1 + (A_H B \sigma)^2) \vec{e}_{r_1}, & \vec{E}_5 &= \frac{I}{2\pi\sigma|\vec{r}_5|d} [(1 - (A_H B \sigma)^2) \vec{e}_{r_5} - 2A_H B \sigma \vec{e}_{\phi_5}] \\ \vec{E}_3 &= -\frac{I}{2\pi\sigma|\vec{r}_3|d} (1 + (A_H B \sigma)^2) \vec{e}_{r_3}, & \vec{E}_6 &= -\frac{I}{2\pi\sigma|\vec{r}_6|d} [(1 - (A_H B \sigma)^2) \vec{e}_{r_6} - 2A_H B \sigma \vec{e}_{\phi_6}].\end{aligned}$$

With the principle of superposition, one can determine the potential difference V_{23} between the voltage-probing contacts by solving the curve integrals between their positions $\vec{r}_{i,3}$ and

$\vec{r}_{i,2}$ with respect to each Corbino source/image i as follows

$$\begin{aligned}
 V_{23} &= - \sum_{i \in \{1,4,5,6\}} \int_{\vec{r}_{i,3}}^{\vec{r}_{i,2}} d\vec{r}_i \cdot \vec{E}_i \\
 &= - \frac{I}{2\pi\sigma d} \left\{ \left[\ln\left(\frac{r_{12}}{r_{13}}\right) + \ln\left(\frac{r_{52}}{r_{53}}\right) - \ln\left(\frac{r_{62}}{r_{63}}\right) - \ln\left(\frac{r_{42}}{r_{43}}\right) \right] \right. \\
 &\quad + (A_H B \sigma)^2 \left[\ln\left(\frac{r_{12}}{r_{13}}\right) - \ln\left(\frac{r_{52}}{r_{53}}\right) + \ln\left(\frac{r_{62}}{r_{63}}\right) - \ln\left(\frac{r_{42}}{r_{43}}\right) \right] \\
 &\quad \left. + 2A_H B \sigma [(\phi_{52} - \phi_{53}) - (\phi_{62} - \phi_{63})] \right\},
 \end{aligned}$$

where $\phi_{52} - \phi_{53}$ and $\phi_{62} - \phi_{63}$ are the two angles that are obtained by counterclockwise integration from probe 2 to probe 3 at the positions of Corbino images 5 and 6, respectively. In this expression, the term that is odd in the magnetic field is identified as the Hall effect voltage. Moreover, the second term is related to the classical quadratic geometrical magnetoresistance that is seen in magnetotransport measurements. When regarding the case of an infinite plane conducting plate, which is a reasonable assumption for microscale four-point arrangements on samples with an exemplary sample size of $1 \text{ cm} \times 1 \text{ cm}$, the positions of the Corbino images \vec{r}_5, \vec{r}_6 extend to infinity and the measured voltage difference is simplified to

$$\begin{aligned}
 V_{23} &= - \frac{I}{2\pi\sigma d} (1 + (A_H B \sigma)^2) \left[\ln\left(\frac{r_{12}}{r_{13}}\right) - \ln\left(\frac{r_{42}}{r_{43}}\right) \right] \\
 &= - \frac{I}{2\pi\sigma d} (1 + (\mu B)^2) \left[\ln\left(\frac{r_{12}}{r_{13}}\right) - \ln\left(\frac{r_{42}}{r_{43}}\right) \right],
 \end{aligned}$$

where the definition of the Hall constant $A_H = \frac{1}{nq}$ is used. As one can see, under infinite plane conditions, there is no Hall effect measured in four-probe measurements in any probe configuration and only the classical geometrical magnetoresistance remains as an influence of magnetic field. According to this expression, the mobility μ of a sample can in principle be inferred from the geometrical magnetoresistance, if the product μB is sufficiently high. With the electromagnet used in this work, i.e. with an estimated $B \approx 200 \text{ mT}$ at typical sample positions $z \approx 2 \text{ mm}$ below the apex of the magnet, a minimum carrier mobility of $\mu \approx 16000 \text{ cm}^2/\text{Vs}$ is required to observe a magnetoresistance of $\Delta R(B)/R(0) = 0.1$.

5.5. Summary

In this chapter, the measurement of spin polarization in charge transport using a four-tip STM was demonstrated in the example of the BST material system.

An investigation of the preparation procedure for ferromagnetic Ni tips was performed. The electromagnet that is used for the *in situ* magnetization of Ni tips in UHV was characterized. The concept of the spin voltage as a quantity resulting from the spin-splitting of the

electrochemical potential and the principle of its detection using magnetized probes was introduced. The connection between the applied charge current and the resulting spin voltage was derived using an interpretation of the spin polarization as the degree of helicity of the TSS. For this purpose, a description of the electronic system as a statistical ensemble of spin states was used.

Using the nanoscale tip positioning method relying on STM scans, spin-sensitive distance-dependent four-point resistance measurements were performed on the surface of two BST thin films of different atomic composition. The room temperature spin signal observed in the case of the $(\text{Bi}_{0.06}\text{Sb}_{0.94})_2\text{Te}_3$ thin film was used to determine the underlying intrinsic spin polarization of the Dirac cone to $p \sim 0.3 - 0.6$.

The results presented in this chapter are largely published in Ref. [134].

Thickness-dependent sheet conductivity of ultra-thin topological insulator films

This chapter demonstrates the investigation of a transition of a 3D TI with a Dirac cone into a massive Dirac fermion regime as its size in one dimension is reduced continuously. On the example of a $(\text{Bi}_{0.16}\text{Sb}_{0.84})_2\text{Te}_3$ thin film, the four-tip STM is used to acquire charge transport characteristics on the nanometer scale depending on the thickness of the film. It is shown that such a transition takes place at a critical film thickness of 5QL. In the 3D TI regime, for 5QL thickness and above, charge transport is found to only occur through the TSS of the TI. In the ultra-thin film limit below 5QL, cross-interaction of TSS opens a gap in the Dirac cone, such that the material system cannot be considered a 3D TI anymore.

After a short introduction into the concept of the transition from a 3D TI to a 2D TI, the geometry of the investigated BST sample system is described. The measurement of the four-point resistance on single terraces of different thickness is demonstrated and a semiclassical model used for its interpretation is derived. From the quantitative results, it is concluded that apart from the arising of a massive Dirac dispersion, charge transport is influenced by an emerging scattering mechanism with reduced sample dimension.

6.1. Hybridization of topological surface states

In chapter 4, it was outlined that the six surfaces of a strong 3D TI each host topological surface states in the shape of a Dirac cone. It was also motivated that the 3D TI phase can be interpreted as a generalization of the QSH phase to three dimensions. Likewise, thin film systems of 3D TIs can be used to realize a phase transition into exotic topological phases such as the QSH or the quantum anomalous Hall (QAH) phase. By the intended breaking of time-reversal symmetry through the manipulation of the stoichiometry of the 3D TI system, 1D chiral edge states can be obtained [135–139]. In terms of the band structure, this mechanism is accompanied by the opening of a finite energy gap in the linearly dispersed TSS of the 3D TI. In particular, the ternary BST material system is a popular template system to study these phase transitions due to its simplicity, as it only has a single Dirac cone at the Γ -point.

Another intuitive approach to cause the emergence of a QSH system, i.e. a 2D TI, is to reduce one dimension of a 3D TI [140–143]. The helical TSS on two opposite faces of a 3D TI material possess reversed spin orientation, as illustrated in Fig. 6.1 (a). If the thickness L of a 3D TI film sufficiently large, such that the TSS at the two interfaces are well separated, they appear as two independent massless Dirac cones. Upon bringing the two TSS close to each other by reducing the sample thickness, their wave functions overlap and the states couple together. The reduction of the physical distance between the interfaces below a critical thickness L_c defines the onset of this interaction. As an effect of the hybridization, an energy gap Δ is opened at the Dirac point [89], such that the charge carriers populating the states act as massive Dirac electrons. This situation is sketched in Fig. 6.1 (b). It is noted that this opening of the TSS gap is a necessary condition for the emergence of the QSH phase. The sufficient condition is determined by the 2D topological invariant ν^{2D} of the resulting system. A thin film of a 3D TI with $\nu^{3D} = 1$ is therefore not necessarily a QSH insulator [143]. If a TI film in the ultra-thin limit $L < L_c$ additionally satisfies $\nu^{2D} = 1$, a QSH phase emerges and the system exhibits helical 1D states within the opened gap Δ at the edges along its circumference. It is known that the topological invariant ν^{2D} can change with varied thickness [140, 141].

The mathematical description of 3D TI films in the ultra-thin film limit is outlined by Lu et al. [140]. For systems with a single Dirac cone in the Brillouin zone, the four-band effective model for bulk Bi_2Se_3 can be applied [84]. The Hamiltonian of the respective model is used to find the four solutions to the TSS of the 3D TI system with the film thickness L being a parameter that defines the boundary condition of vanishing wave functions at the two surfaces at $z = \pm L/2$. The original Hamiltonian is then mapped to the Hilbert space spanned

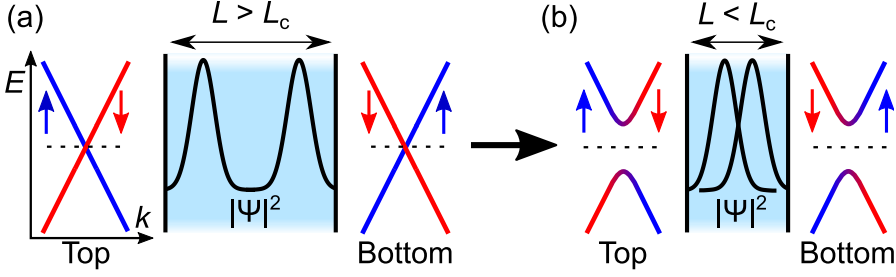


Fig. 6.1.: Illustration of the hybridization between overlapping TSS wave functions in a 3D TI thin film. **(a)** The two opposite surfaces of a 3D TI film each host helical TSS with inverted spin orientations. For a film with sufficiently large thickness $L > L_c$, the Dirac cones act as independent states. **(b)** As the physical distance between the interfaces is reduced below the critical thickness $L < L_c$, the bound wave functions couple and the TSS start to interact. Consequently, a gap opens at the Dirac point and the surface bands evolve into hyperbolic curves.

by the four TSS eigenstates to obtain an effective Hamiltonian for the ultra-thin film [144]

$$H_{\text{eff}} = \begin{pmatrix} h_+(k) & 0 \\ 0 & h_-(k) \end{pmatrix} \quad (6.1)$$

with

$$h_{\pm}(k) = E_0 - Dk^2 - \hbar v_F(k_x \sigma_y - k_y \sigma_x) \pm \left(\frac{\Delta}{2} - Bk^2 \right) \sigma_z, \quad (6.2)$$

where E_0 , D and B are material-dependent parameters of the Hamiltonian. The Dirac fermions obeying this Hamiltonian have a dispersion relation [140]

$$E_{\pm}(k) = E_0 - Dk^2 \pm \sqrt{(\hbar v_F k)^2 + \left(\frac{\Delta}{2} - Bk^2 \right)^2}, \quad (6.3)$$

with the index \pm denoting the conduction/valence band and $E_0 = \frac{E_+(0) + E_-(0)}{2}$ being the mid-gap energy (Dirac point). This expression describes the opening of a gap $\Delta = E_+(0) - E_-(0)$ in the TSS at the Γ -point. The dependence on the film thickness L which defines the boundary conditions of the wave functions is contained in the model parameters. It is noted that in the limit of large L , the linear dispersion $E(k) = \hbar v_F k$ of the massless Dirac fermions of a 3D TI is retained [140].

6.2. Sample characteristics

The investigated sample is a $(\text{Bi}_{0.16}\text{Sb}_{0.84})_2\text{Te}_3$ thin film of 12QL thickness that is realized on a silicon-on-insulator (SOI) substrate, as sketched in Fig. 6.2 (a). The SOI substrate is

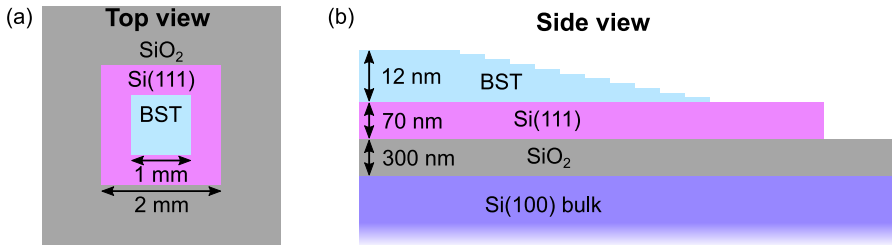


Fig. 6.2.: Layout of the investigated BST sample. **(a)** Enabled by growth through a shadow mask, the TI film is formed as an isolated patch on the SOI substrate with a lateral boundary to the underlying Si layer. **(b)** Due to the shielding effect of the shadow mask, the thickness of the resulting BST film in the boundary region decreases in single QL steps down to the substrate level. The single terraces with 1 QL height difference define the wedge shape of the TI film.

comprised of a degenerately doped Si(100) handle wafer, a 300 nm SiO₂ layer and an undoped Si(111) template layer of 70 nm thickness. The sheet conductivity of the intrinsic Si layer is determined to ~ 2 nS in the experiment, which is a value that is sufficiently low to prevent parasitic contributions to charge transport.

Sample layout

The BST thin film is deposited by MBE through a shadow mask, which allows the formation of isolated TI patches with boundaries on the substrate without the need of ex situ processing. Moreover, the use of the shadow mask results in a wedge shape of the TI structure in the boundary region. As indicated in Fig. 6.2 (b), the thickness of the film decreases in steps of single quintuple layers from 12QL at its center down to the substrate level. The specific BST composition is determined *ex situ* after the experiment and is initially chosen deliberately for its position of the Fermi level $E_F = 50$ meV in the band gap (Fig. 4.4 (b)).

In the experiment, the STM tips are brought to the sample surface by means of a capacitive approach. Since the BST patches are situated electrically isolated on the oxide layer of the SOI substrate, a conventional tip approach by detecting a DC current through the sample is not possible. Instead, an AC voltage is applied to the back gate of the sample, causing an AC current between the back gate and the tip due to the capacitive coupling that is provided by the oxide layer. As the tip is closing the distance to the sample surface, the tip-sample capacity is increased. Upon reaching tunneling contact, a drastic increase in capacity occurs, resulting in a sharp current ramp. By choosing appropriate parameters, the tip approach can be interrupted by the STM feedback loop at this moment. To approach the BST thin film in this way, an AC voltage of 110 mV at ~ 520 Hz was used, with the tip kept at a potential of 1 V and

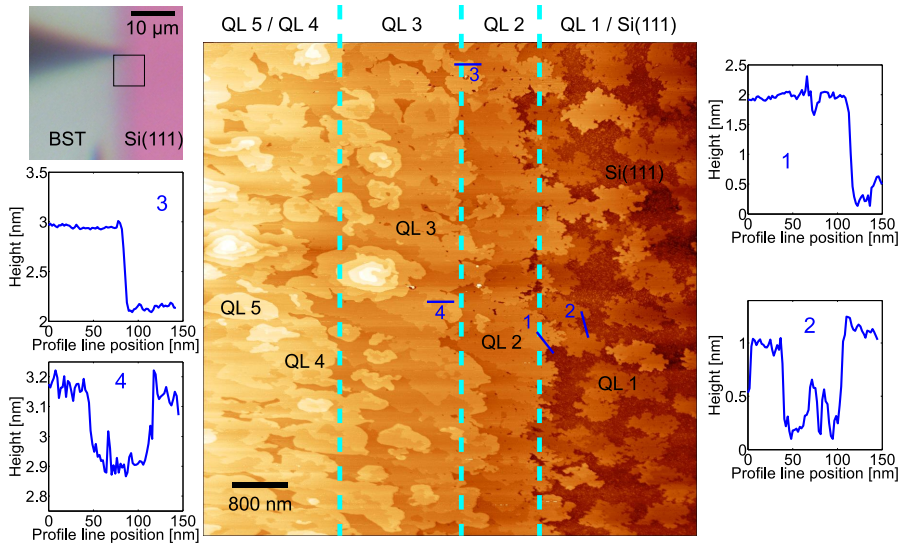


Fig. 6.3.: Topography scan of the wedge-shaped BST film at its boundary to the substrate. An corresponding optical micrograph with a rectangle indicating the scanned area is featured in the top left panel. In the scan image, the film is seen to increase in thickness perpendicularly to the film boundary. The average orientation of step edges is indicated by the cyan lines. The blue-colored height profile lines 2 and 3 show that the increase in thickness occurs in single QL steps. As evident from profile line 1, the first closed terrace on the substrate is of 2QL thickness. Profile line 4 shows a sub-QL step of 0.3 nm height originating from a Si substrate step [98, 145, 146].

the set-point current set to ~ 100 pA. Using this set of parameters, the approach is terminated right when the tip reaches tunneling contact. With maintained AC voltage, the tip can be kept in tunneling contact to the sample which is stable enough to also image the topography. After lowering the tip to the surface to establish ohmic contact, the sample potential is controlled via the tip bias, such that the other STM tips can be brought to tunneling contact using the DC current.

Figure 6.3 presents a $7\mu\text{m} \times 7\mu\text{m}$ STM scan at the boundary of a BST patch. As can be seen in the topography, the TI film thickness decreases in a wedge shape towards the substrate, revealing approximately parallel terraces of different height. For comparison, the corresponding orientation of the scan is indicated in the optical microscope of the sample boundary view in the top left panel. Cyan dashed lines are included in the scan image as a guide to the eye to indicate the average orientation of the step edges between the terraces.

The increase in height between each terrace is found to be $1\text{ nm} \cong 1\text{ QL}$, as evident from height

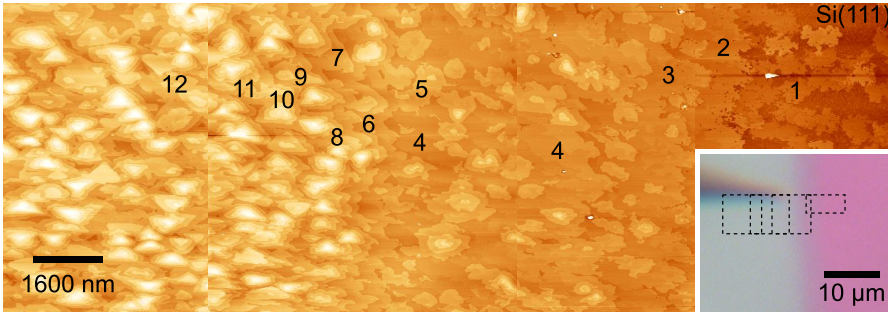


Fig. 6.4.: Full range of the TI film boundary region imaged by overlapping of successive topography scans. Within a lateral span of $\sim 13\mu\text{m}$, the film thickness increases up to a maximum value. By counting the discernible terraces of increasing height, the thickness of the film interior is determined to $L = 12\text{QL}$. For $L > 4\text{QL}$, the island density is enhanced sharply.

profile lines perpendicular to the step edges (blue lines 2 and 3 in the scan image). Terraces of 1 QL thickness are only found as small islands on the substrate. The first TI layer that forms in a closed manner is the 2QL terrace (blue line 1 in Fig. 6.3), such that its step edge is mostly bordering the Si(111) substrate. In addition to the single QL steps between the terraces, sub-QL steps of $\sim 0.3\text{ nm}$ height are observed throughout the TI topography (blue line 4 in Fig. 6.3). These steps are mostly seen at low film thickness and are known to occur as a propagation of the underlying Si substrate steps [98, 145, 146].

It is apparent that flat and closed sections of the TI film are predominantly seen on terraces with $1\text{QL} < L < 5\text{QL}$, while film regions of thickness $L \geq 5\text{QL}$ feature various small islands, resulting in an increased surface roughness. This is more evident in Fig. 6.4, where multiple large topography scans at the boundary region are overlapped, encompassing regions of the film with saturated film thickness. An increase in film thickness up to a maximum value in the interior of the BST patch can be observed in the topography. The maximum film thickness $L \approx 12\text{QL}$ is inferred from the last terrace that can be considered closed and is determined by counting the individual terraces from the Si substrate level, as indicated by the numbers in the scan image. Evidently, there is a sharp increase in island density on the surface of the film for $L > 4\text{QL}$ resulting from a transition to island-dominated growth [145].

Microscale characterization

Before performing transport measurements with nanoscale tip spacing, the $(\text{Bi}_{0.16}\text{Sb}_{0.84})_2\text{Te}_3$ thin film is characterized electrically on the micrometer scale. Four-point resistance measurements in linear configuration are performed in the interior of a BST patch, far away from the

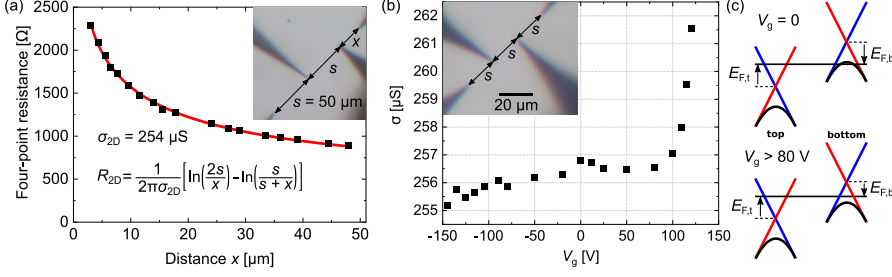


Fig. 6.5. Microscale four-point resistance measurements on the surface of the $(\text{Bi}_{0.16}\text{Sb}_{0.84})_2\text{Te}_3$ thin film. As seen in the optical micrographs featured in the insets, the four STM tips are placed in the interior of the BST patch, where $L = 12\text{QL}$. **(a)** As evident from the fit of the 2D resistance model (Eq. 2.20) denoted by the red curve, the measured distance-dependent resistance is explained by a 2D conductivity of $\sigma_{2\text{D}} = 254\ \mu\text{S}$. **(b)** The sheet conductivity, acquired at fixed tip positions with equidistant spacing as a function of back-gate voltage V_g , shows almost no change for $V_g \lesssim 80\text{V}$. In contrast, a steep increase is observed at $V_g \gtrsim 80\text{V}$. From this characteristic evolution, it is concluded that the position of the Fermi level at the bottom interface is at the valence band edge $E_{\text{F},\text{b}} \approx -50\text{meV}$. **(c)** Schematic representation of the band structure of the TI under the influence of the gate voltage V_g .

film boundary, where the film is at its maximum thickness of 12QL. The distance-dependent data, acquired by moving one of the current-injecting tips, while the others are sitting at a spacing of $s = 50\ \mu\text{m}$, is presented in Fig. 6.5 (a). From the recorded resistance, the corresponding film conductivity is determined from a fit of the 2D model function Eq. 2.20, resulting in $\sigma_{2\text{D}} \approx 254\ \mu\text{S}$. As the charge transport in this configuration only occurs in the interior of the TI patch, this value is ascribed to the BST film at its maximum thickness of $L = 12\text{QL}$.

The use of the SOI structure as a substrate for the BST film not only prevents undesired substrate contributions to charge transport, but also allows gate-dependent measurements of the sample conductivity. Figure 6.5 (b) demonstrates a measurement of the film conductivity at $L = 12\text{QL}$ under variation of the voltage V_g applied to the back gate. Similarly to the distance-dependent resistance measurement in Fig. 6.5 (a), the tips are placed in the interior of a BST patch, but are left at constant equidistant positions with $s = 20\ \mu\text{m}$. While slowly sweeping the gate voltage in the range of $-150\text{V} \leq V_g \leq 120\text{V}$, the sheet conductivity is determined from multiple $I - V$ characteristics according to Eq. 2.35

$$\sigma_{2\text{D}} = \frac{\ln 2}{\pi R_{2\text{D}}^{4\text{P}}} \cdot \quad (6.4)$$

Evidently, there is almost no change in conductivity in the entire voltage range up to $\approx +80\text{V}$. Beyond this voltage, however, the conductivity increases sharply.

The acquired gate dependence of the sheet conductivity is interpreted qualitatively as indi-

cated in the sketch in Fig. 6.5 (c) to ultimately infer the position of the Fermi level $E_{F,b}$ at the bottom TI interface. As is known from ARPES [100], the top interface Fermi level $E_{F,t}$ of the $(\text{Bi}_{0.16}\text{Sb}_{0.84})_2\text{Te}_3$ composition is located approximately 50 meV above the Dirac point and approximately 100 meV above the bulk valence band (Fig. 4.4 (b)). Upon the application of a gate voltage, charge carriers are induced in the TI system by the corresponding electric field and distributed between the bulk states and the TSS at the top and the bottom interfaces. This corresponds to a shift of the band structure relative to the Fermi level, as indicated in Fig. 6.5 (c). The top interface is however only influenced little by the back gate, as it is effectively shielded from the field effect by the bottom interface [101]. The extent of the shift at the bottom interface is dependent on the magnitude of the density of states at the Fermi level $E_{F,b}$.

For gate voltages $V_g \lesssim 80\text{V}$, the Fermi level at the bottom interface intersects the TSS and the bulk valence band, such that induced charge carriers mainly populate the bulk states due to their much larger density of states compared to the Dirac cone. Since the mobility of the bulk carriers is comparatively low at room temperature ($\sim 2\text{ cm}^2/\text{Vs}$) [101], the total conductivity is almost unchanged in this gate voltage range.

At gate voltages $V_g \gtrsim 80\text{V}$, the bulk valence band is fully populated and $E_{F,b}$ is shifted into the bulk band gap. Therefore, the Fermi level only intersects the Dirac cone and additional charge carriers induced by the field effect only populate the TSS, resulting in a steeper increase of the measured conductivity due to the high TSS mobility. Following this interpretation, the characteristic evolution of the conductivity implies that at $V_g = 0$, the bottom Fermi level of the 12 QL $(\text{Bi}_{0.16}\text{Sb}_{0.84})_2\text{Te}_3$ film is situated at the valence band edge, i.e. at $E_{F,b} \approx -50\text{ meV}$. This is in agreement with the fact that the composition of the present sample is close to pure Sb_2Te_3 , which naturally exhibits hole doping, in contrast to Bi_2Te_3 which is typically electron doped. Moreover, the observation of $E_{F,t} > E_{F,b}$ is explained by substrate interactions and is also found in other gate-dependent studies of TI thin films [97, 101].

6.3. Thickness-dependent sheet conductivity measurements

The wedge shape of the structured BST film has the advantage that it comprises regions of different film thickness on a single sample. With the positioning method outlined in chapter 3, the four STM tips can be placed on individual terraces in the film boundary region with inter-tip distances on the nanometer scale. This enables access to electrical properties of the $(\text{Bi}_{0.16}\text{Sb}_{0.84})_2\text{Te}_3$ film at different film thicknesses, as illustrated conceptually in Fig. 6.6 (a).

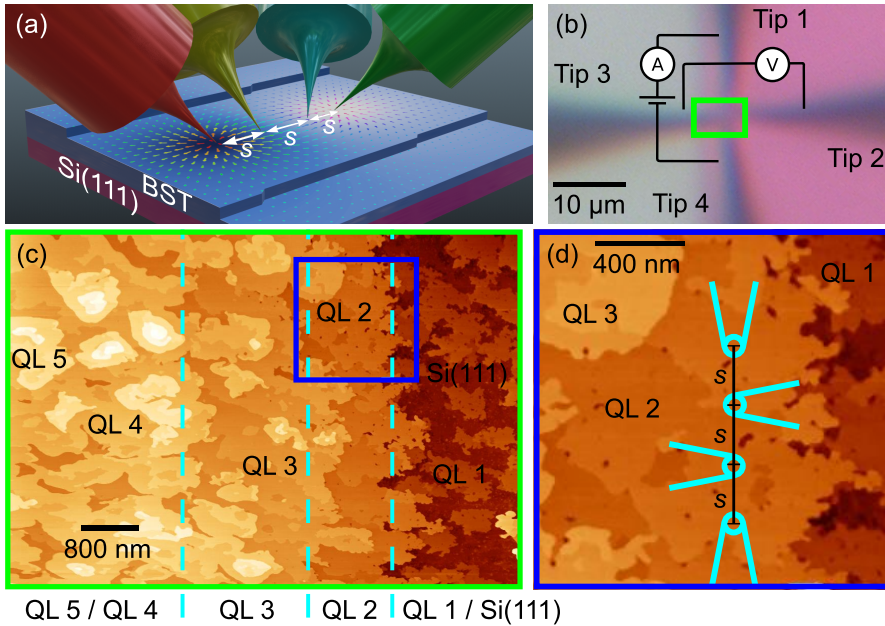


Fig. 6.6.: Principle of the thickness-dependent conductivity measurement on the $(\text{Bi}_{0.16}\text{Sb}_{0.84})_2\text{Te}_3$ thin film. **(a)** Conceptual depiction of the measurement setup. In the wedge-shaped boundary region of the BST film, tips are positioned on single terraces, such that the sheet conductivity of the TI can be measured as a function of film thickness L . The artwork was designed by Vasily Cherepanov. **(b)** Optical microscope image of an exemplary measurement configuration. **(c)** Exemplary overview scan of the local topography used for positioning. The corresponding orientation of the overview scan is indicated in the optical micrograph. **(d)** Final tip configuration on a 2QL terrace in the region that is highlighted as a blue square in the overview scan.

For contacting, the four tips are individually navigated into the boundary region of the film, as shown in the optical micrograph in Fig. 6.6 (b). Using the previously recorded overview scan of the area, the tips are positioned in a linear equidistant configuration on a flat section of a single terrace, with an inter-tip distance of $s \approx 250 \text{ nm}$. This arrangement is shown exemplary in Fig. 6.6 (c) and (d) for the case of a measurement on the 2QL thick film, with the final positions of the tips indicated by cyan symbols. In each set of measurements, the inter-tip distance s is chosen to be as small as possible, such that the edges of neighboring terraces are comparatively far away and therefore their influence on charge transport is minimal.

In the realized configuration, the four-point resistance is determined from multiple $I - V$

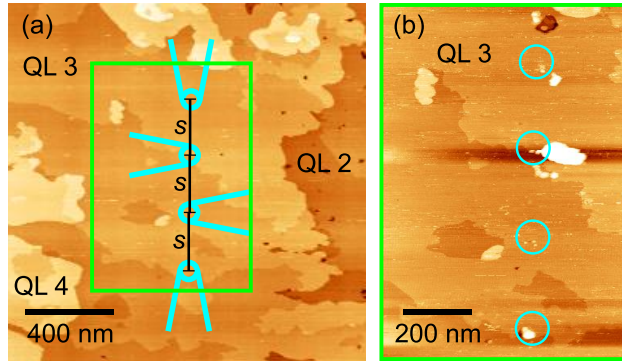


Fig. 6.7.: Topography of a BST terrace imaged before and after electrical measurements. **(a)** Section of the BST thin film with a thickness of $L = 3QL$ that was chosen for a four-point resistance measurement. Corresponding tip positions during the four-point measurements are indicated by cyan symbols. **(b)** Topography scan of the same area immediately after performing the electrical measurements. The contact points of the four tips are discernible as small spots of ~ 1 nm height. Evidently, only little damage is done to the terrace surface during the positioning and measurement process.

characteristics and used to calculate a sheet conductivity following Eq. 6.4. According to this scheme, the conductivity of the BST thin film for varying film thickness $1QL \leq L \leq 5QL$ is determined, with each conductivity value obtained from several measurements in different areas of the sample, as presented in appendix B.1. For $L > 5QL$, four-point measurements on single terraces are not possible to realize, because as a consequence of the sharply increased island density (Fig. 6.4), the terraces are too narrow to reliably place the four tips on them. From subsequent topography scans, as presented exemplary in Fig. 6.7, it is inferred that the film surface, including the local terrace structure, is still intact after the electrical measurements. Therefore, the attribution of the obtained sheet conductivities to BST films of corresponding thickness L is well defined.

Figure 6.8 (a) presents the measured $(Bi_{0.16}Sb_{0.84})_2Te_3$ sheet conductivity as a function of film thickness L . The sheet conductivity that is attributed to 12QL film thickness as inferred from transport measurements in the interior of the BST structure is included in the data set. Evidently, the sheet conductivity exhibits a roughly exponential increase with film thickness from 1QL to 5QL. It is noted that the conductivity of 1 nS measured for $L = 1QL$ is interpreted as an upper boundary, since the conductivity of the underlying Si substrate layer (~ 2 nS) is in the same order of magnitude. The value ascribed to the 12QL film is, within measurement errors, coinciding with the one measured on the 5QL film, suggesting a conductivity plateau. This saturation of the thickness-dependent conductivity substantiates that charge transport in the TI material is dominated by the TSS. A possible parasitic contribution to transport

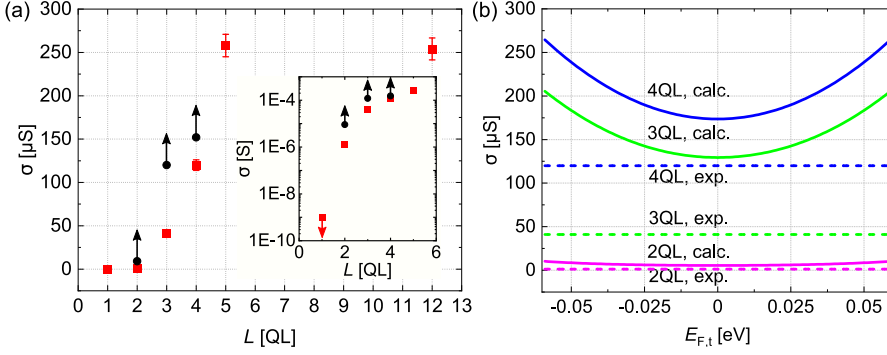


Fig. 6.8.: Measured thickness-dependent sheet conductivity of the BST film in comparison to calculations based on the TSS band structure. **(a)** Thickness-dependent conductivity (red squares with error bars) as obtained from resistance measurements on single terraces of different layer thickness. The black circles denote the global minima of the calculated conductivity resulting from the variation of the model parameters $E_{F,t}$, $E_{F,b}$ and r_μ . A logarithmic plot of the data is featured in the inset. **(b)** Exemplary calculated conductivity based on the change of the band structure (Eq. 6.16) as function of $E_{F,t}$, with $r_\mu = 1$ and $E_{F,b} = -50$ meV.

originating from bulk states would be indicated by a linear dependence of the conductivity on film thickness L .

6.3.1. Modeling the film conductivity

TSS gap opening

One contribution to the drastic decrease of the sheet conductivity with reduced L that needs to be considered in the interpretation of the measurement results is the expected opening of a TSS energy gap Δ [140–143]. In the case of Sb_2Te_3 , spectroscopic investigations [92] and concurrent theoretical predictions [143] demonstrate the opening of a surface gap for $L < 5$ QL. Since the present BST sample is a material of similar composition, the reported $\Delta(L)$ values are adopted to explain the observed change in conductivity for $L < 5$ QL. The adopted TSS energy gaps are $\Delta(2\text{QL}) \approx 250$ meV, $\Delta(3\text{QL}) \approx 60$ meV and $\Delta(4\text{QL}) \approx 25$ meV.

With the TSS of the thin film demonstrated to be the only contribution to charge transport by the observed conductivity plateau, the sheet conductivity is given by the charge carrier concentrations n and carrier mobilities μ in the top and bottom TSS following the Drude formalism

$$\sigma = e [\mu_t n_t(\Delta, E_{F,t}) + \mu_b n_b(\Delta, E_{F,b})], \quad (6.5)$$

where the carrier densities at the two interfaces are determined by the band structure and therefore depend on the respective position of the Fermi level and the surface gap Δ . The change in the band structure with varying film thickness is modeled by [140, 147]

$$E(k, L) = \pm \sqrt{(\hbar v_F k)^2 + (\Delta(L)/2)^2} \quad (6.6)$$

as an approximation of the general massive Dirac dispersion in the ultra-thin film limit given by Eq. 6.3. As part of this approximation for the interpretation of the transport results, the unknown model parameters D and B that influence the curvature of the TSS at the Γ -point are assumed to be zero. The Fermi velocity $v_F = 4.2 \cdot 10^5$ m/s defining the slope of the Dirac cone is inferred for the present BST sample from interpolation of ARPES results [100, 101] (section 4.2). Following the dispersion relation, the density of states under the effect of a gap opening is given by

$$D(\Delta(L), E) = \frac{|E|}{2\pi(\hbar v_F)^2} \Theta(|E| - \Delta(L)/2), \quad (6.7)$$

which is used to determine the charge carrier density as

$$n(\Delta(L), E_F) = \int_0^\infty D(\Delta(L), E) [f_n(E, E_F) + f_p(E, E_F)] dE, \quad (6.8)$$

with the Fermi distribution function

$$f_n(E, E_F) = f_p(E, -E_F) = \left(1 + \exp\left(\frac{E - E_F}{k_B T}\right)\right)^{-1} \quad (6.9)$$

for electrons (n) and holes (p).

With these relations, the thickness-dependent sheet conductivity of the BST thin film can be determined according to Eq. 6.5 for given carrier mobilities $\mu_{t/b}$ and Fermi level positions $E_{F,t/b}$ at the top and bottom surface. For a film thickness of $L \geq 5$ QL, $E_{F,t} = 50$ meV is known from photoemission experiments (section 4.2) and $E_{F,b} = -50$ meV is found from gate-dependent transport measurements. Using these $E_{F,t/b}$, the carrier mobility at $L \geq 5$ QL is determined from the measured conductivity as

$$\mu_t(5 \text{ QL}) = \frac{\sigma(5 \text{ QL})}{e[n_t(5 \text{ QL}) + r_\mu n_b(5 \text{ QL})]}, \quad (6.10)$$

where a ratio r_μ is assumed between the mobilities in the top and bottom TSS, such that $\mu_b(L) = r_\mu \mu_t(L)$. In general, the mobility in the TSS at the top surface is given by

$$\mu_t(L) = \frac{e}{m^*(L)} \tau_0, \quad (6.11)$$

with m^* and τ_0 denoting the effective mass and the scattering time, respectively. τ_0 considers scattering of carriers within the TSS due to surface defects and electron-phonon interaction. As these sources of scattering are not influenced by the physical distance between the opposite

film interfaces, τ_0 does not depend on L . In contrast, the effective mass m^* , being a property of the band structure, is influenced by the opening of the surface gap $\Delta(L)$ according to [148]

$$m^*(L) = \hbar^2 k \left(\frac{dE}{dk} \right)^{-1} \Big|_{k=k_{F,t}} \quad (6.12)$$

$$= \hbar^2 k \left(2k(\hbar v_F)^2 \frac{1}{2\sqrt{[\hbar v_F k]^2 + [\Delta(L)/2]^2}} \right)^{-1} \Big|_{k=k_{F,t}} \quad (6.13)$$

$$= \frac{1}{v_F^2} \sqrt{E_{F,t}^2 + [\Delta(L)/2]^2}. \quad (6.14)$$

Hence, the change of $\mu_t(L)$ following from the change of the band structure associated with the gap opening is extrapolated from its value at $L' = 5QL$ (Eq. 6.15) by

$$\mu_t(L) = \mu_t(L') \cdot \frac{m_t^*(L')}{m_t^*(L)} = \mu_t(L') \cdot v_F^2 \frac{m_t^*(L')}{\sqrt{E_{F,t}^2 + [\Delta(L)/2]^2}}. \quad (6.15)$$

Using Eq. 6.5, this model yields thickness-dependent sheet conductivities

$$\sigma(L) = e\mu_t(L)[n_t(L) + r_\mu n_b(L)] \quad (6.16)$$

based on the surface gap opening alone through a parametric dependence on $E_{F,t}$, $E_{F,b}$ and r_μ . Figure 6.8 (b) presents the calculated sheet conductivities using this model as a function of $E_{F,t}$ for $2QL \leq L \leq 4QL$, assuming $E_{F,b} = -50$ meV and $r_\mu = 1$. Since the values of the parameters are generally not known for $L < 5QL$, a variation within reasonable ranges is considered with $E_{F,t}$, $E_{F,b} \in [-50$ meV; 50 meV]. The parameter r_μ is varied within [0.3; 1], since previous transport investigations in BST thin films have shown r_μ to be as low as 0.3 [101]. The global minima of the sheet conductivities $\sigma(L)$ obtained in these ranges are displayed as black circles in Fig. 6.8. Evidently, this model cannot reproduce the drastic drop in conductivity that is observed in the experiment, as the calculated values are systematically too high for all variations of the parameters in spite of the opened energy gap. It is therefore concluded that a mere band structure effect does not explain the experimental data.

Inter-TSS scattering

From the systematic overestimation by the previous model, it is clear that that an additional mechanism beyond the gap opening emerges and lowers the TSS conductivity at low L . The Dirac cones at the two interfaces of the TI film have opposite helicity, such that charge carriers moving in a common direction have inverted spin in the opposite TSS. In the ultra-thin film limit, the coupling between the opposite TSS on the one hand leads to the formation of a gapped band structure. On the other hand, as the physical distance between the interfaces is

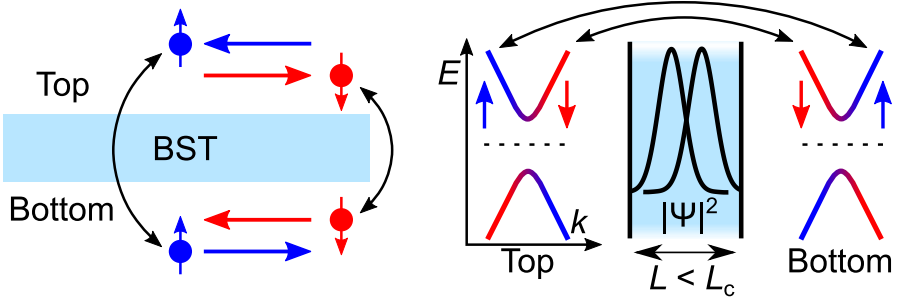


Fig. 6.9.: Real space and momentum space representation of inter-TSS scattering in ultra-thin TI films. Apart from the opening of a surface energy gap, the interaction between the two surface states of inverted helicity enables spin-conserving backscattering, as indicated by the black arrows. As a consequence of the permitted inter-TSS scattering process, carrier mobility is expected to reduce.

reduced, the interaction of top and bottom surface states allows spin-conserving scattering from k to $-k$, as indicated by the black arrows in Fig. 6.9. Effectively, this corresponds to a lifting of spin-momentum locking in the TSS.

The emergence of the additional scattering mechanism is expected to influence the electronic properties of the thin film. In particular, the scattering time τ of charge carriers in the TSS is reduced according to Matthiesen's rule $\tau^{-1} = \tau_0^{-1} + \tilde{\tau}^{-1}$. Here, $\tilde{\tau}$ represents the emerging inter-TSS scattering, whereas τ_0 denotes intra-TSS scattering as defined above. The corresponding contribution of inter-TSS scattering to the carrier mobility is given by

$$\tilde{\mu}_t(L) = \frac{e}{m^*(L, E_{F,t})} \tilde{\tau}_t \quad (6.17)$$

and an analogous expression for $\tilde{\mu}_b$. Following Matthiesen's rule, inter-TSS scattering considered in the conductivity model by including the additional mobility component in the total effective mobility of the thin film as

$$\mu_{\text{eff},t}(L) = (\mu_t(L)^{-1} + \tilde{\mu}_t(L)^{-1})^{-1} = \frac{\mu_t(L)\tilde{\mu}_t(L)}{\mu_t(L) + \tilde{\mu}_t(L)} \quad (6.18)$$

and

$$\mu_{\text{eff},b}(L) = \frac{\mu_b(L)\tilde{\mu}_b(L)}{\mu_b(L) + \tilde{\mu}_b(L)} = \frac{r_\mu \cdot \mu_t(L)\tilde{\mu}_b(L)}{r_\mu \cdot \mu_t(L) + \tilde{\mu}_b(L)}. \quad (6.19)$$

In these relations, $\mu_t(L)$ is identical to the intra-TSS mobility given by the L -dependent change in band structure alone, as considered before in Eq. 6.15.

In the above form, $\mu_{\text{eff},t}(L)$ and $\mu_{\text{eff},b}(L)$ still depend on the two unknown variables $\tilde{\mu}_t(L)$ and $\tilde{\mu}_b(L)$. The relation between the two inter-TSS mobilities is given by

$$\frac{\tilde{\mu}_b(L)}{\tilde{\mu}_t(L)} = \frac{\tilde{\tau}_b}{\tilde{\tau}_t} \frac{m^*(L, E_{F,t})}{m^*(L, E_{F,b})}. \quad (6.20)$$

The scattering between the top and bottom TSS is dictated by Fermi's golden rule as

$$\frac{1}{\tilde{\tau}_t} = \frac{2\pi}{\hbar} D(E_{F,b}) |V_{t \rightarrow b}|^2, \quad (6.21)$$

and the corresponding equation for $\tilde{\tau}_b$. It is intuitive that the squared transition matrix elements corresponding to scattering from the top to the bottom ($|V_{t \rightarrow b}|^2$) and from the bottom to the top ($|V_{b \rightarrow t}|^2$) surfaces must be equal, as they are both determined by the mutual overlap of the TSS wave functions. Therefore, the relation in Eq. 6.20 can be further specified to

$$\frac{\tilde{\mu}_b(L)}{\tilde{\mu}_t(L)} = \frac{D(E_{F,t}) m^*(L, E_{F,t})}{D(E_{F,b}) m^*(L, E_{F,b})} \quad (6.22)$$

$$\Rightarrow \tilde{\mu}_b(L) = \tilde{\mu}_t(L) \frac{D(E_{F,t}) \sqrt{E_{F,t}^2 + [\Delta(L)/2]^2}}{D(E_{F,b}) \sqrt{E_{F,b}^2 + [\Delta(L)/2]^2}} \quad (6.23)$$

by using the definition of the effective mass m^* in Eq. 6.14. Because of the increasing wave function overlap between the two TSS, it is expected that in thermodynamic equilibrium, $E_{F,t}$ and $E_{F,b}$ converge to a common level as L decreases. Following Fermi's golden rule, this eventually results in $\tilde{\tau}_t \rightarrow \tilde{\tau}_b$ and – according to the above relation – consequently in $\tilde{\mu}_t(L) \rightarrow \tilde{\mu}_b(L)$. If this equilibration were not to occur, with $\tilde{\tau}_t$ and $\tilde{\tau}_b$ being unequal in the ultra-thin film limit, one interface would be continuously charged relative to the other, which cannot happen indefinitely.

As an approximation, it is assumed in the model that $E_{F,t} = E_{F,b}$ as soon as the two surface states are observed to interact, i.e. for $L \leq 4$ QL. Consequently, with $\tilde{\mu}_t(L) = \tilde{\mu}_b(L) = \tilde{\mu}(L)$, the Drude formalism is used in analogy to Eq. 6.5 to find the conductivity model with included inter-TSS scattering

$$\sigma(L) = e \left[n_t(L) \mu_{\text{eff},t}(L) + n_b(L) \mu_{\text{eff},b}(L) \right] \quad (6.24)$$

$$= e \left[n_t(L) \frac{\mu_t(L) \tilde{\mu}(L)}{\mu_t(L) + \tilde{\mu}(L)} + n_b(L) \frac{r_\mu \mu_t(L) \tilde{\mu}(L)}{r_\mu \mu_t(L) + \tilde{\mu}(L)} \right], \quad (6.25)$$

which parametrically depends on $E_{F,t}$, $E_{F,b}$ and r_μ .

This model is used to describe the measured thickness-dependent sheet conductivity in Fig. 6.8 (a). For this purpose, Eq. 6.25 is solved numerically for $\tilde{\mu}(E_{F,t}, E_{F,b}, r_\mu)$ at each L , which ultimately yields μ_{eff} at both interfaces. Figure 6.10 presents the correspondingly obtained thickness-dependent effective carrier mobility $\mu_{\text{eff},t}(L)$ in the top TSS. With the model parameters $E_{F,t}$, $E_{F,b}$, r_μ generally being not known for $L < 5$ QL, it is only possible to display a band within which the mobility is located. The band is obtained from the variation of the three parameters within reasonable ranges. Evidently, the total mobility of the top

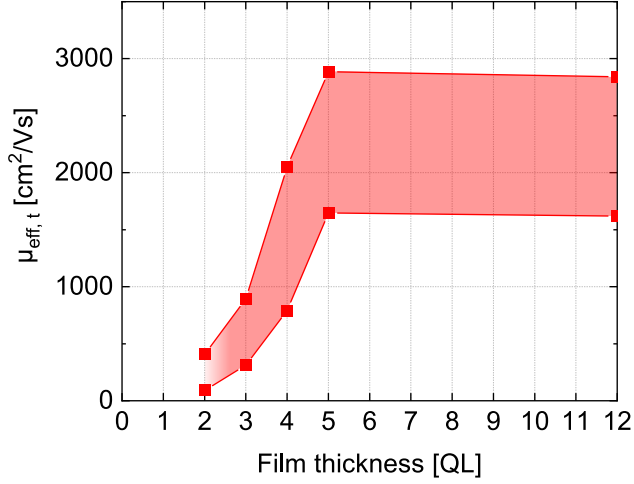


Fig. 6.10. Thickness-dependent electron mobility inferred from experimental results under consideration of spin-conserving backscattering. By using the Drude formalism in Eq. 6.5 and including a thickness-dependent mobility component due to emerging inter-TSS scattering, the top TSS mobility $\mu_{\text{eff},t}$ is determined for each layer thickness using the measured conductivity. The band indicated in red represents the range of mobility values resulting from a variation of the model parameters $E_{F,t}, E_{F,b} \in [-50 \text{ meV}; 50 \text{ meV}]$ and $r_\mu \in [0.3; 1]$. The drop in mobility with decreasing film thickness represents enhanced scattering of charge carriers between the two TSS as the physical distance between the interfaces is reduced. For $L \geq 5\text{QL}$, the carrier mobility $\mu_{\text{eff},t}$ is limited by intra-TSS scattering only. The corresponding inter-TSS scattering times are $11 \text{ fs} < \bar{\tau}_{4\text{QL}} < 56 \text{ fs}$, $10 \text{ fs} < \bar{\tau}_{3\text{QL}} < 19 \text{ fs}$ and $8 \text{ fs} < \bar{\tau}_{2\text{QL}} < 45 \text{ fs}$. For $L \geq 5\text{QL}$, $E_{F,t}$ is known and the displayed range is influenced only by r_μ and $E_{F,b}$.

surface $\mu_{\text{eff},t}$ exhibits a dramatic decrease at low L . It is emphasized that only by accounting for this decrease in mobility, the discrepancy between experimental and calculated sheet conductivity in Fig. 6.8 is explained successfully.

According to Eq. 6.17, a corresponding range of the inter-TSS scattering times $\bar{\tau}$ as a function of L can be determined. It is generally found that $\bar{\tau} < \tau_0$ for all thicknesses $2\text{QL} \leq L \leq 4\text{QL}$, which means that the inter-TSS scattering dominates the intra-TSS scattering. The intra-TSS scattering time is found as $46 \text{ fs} < \tau_0 < 71 \text{ fs}$, depending on the position of $E_{F,t}$ and $E_{F,b}$. The obtained ranges of $11 \text{ fs} < \bar{\tau}_{4\text{QL}} < 56 \text{ fs}$, $10 \text{ fs} < \bar{\tau}_{3\text{QL}} < 19 \text{ fs}$ and $8 \text{ fs} < \bar{\tau}_{2\text{QL}} < 45 \text{ fs}$ demonstrate that the dependence of the inter-TSS scattering time on film thickness is weak. This observation is explained by $\bar{\tau}$ being under influence of two competing effects. As seen from Fermi's golden rule in Eq. 6.21, the increase of the matrix element for scattering with reducing L leads to a reduction of $\bar{\tau}$. On the other hand, the simultaneous opening of the surface gap reduces the density of states at E_F to scatter into, which has the opposite effect

on the scattering time. As a result, the counter-acting influences keep $\bar{\tau}$ approximately in the same range with varying L .

From the interpretation of the thickness-dependent sheet conductivity of the BST sample with the presented model, it is clear that the emerging inter-TSS scattering reduces the conductivity in ultra-thin TI films beyond what is expected from the opening of a surface energy gap. Moreover, the evaluation reveals that the spin-conserving scattering of carriers between top and bottom TSS is in fact the dominant scattering mechanism. For TI thin films in general, it is concluded that the additional scattering mechanism constitutes a significant reduction of surface state conductivity, even if the Fermi level is not located in the TSS gap and the influence of the gap itself on transport is small. This is an important observation, as this effect facilitates the detection of 1D edge states in transport measurements on 2D TIs against the residual parasitic conductivity of the 2D surface states.

6.4. Summary

In this chapter, the interaction of the opposite TSS of a $(\text{Bi}_{0.16}\text{Sb}_{0.84})_2\text{Te}_3$ thin film and its effect on charge transport were investigated. By exploiting the boundary region of the structured thin film with its systematically decreasing thickness, the surface state conductivity was measured as a function of film thickness. The thickness-dependent electrical measurements were performed by nanoscale positioning of the STM tips on single terraces of the thin film.

It was found that a characteristic change of conductivity occurs below a critical film thickness of $L_c = 5\text{QL}$. From the constant behavior of the acquired sheet conductivity in the regime of separated interfaces ($L > L_c$), it was inferred that the induced current in the sample is carried by TSS exclusively. Furthermore, the experimental data led to the conclusion that the interaction of the two TI interfaces in the ultra-thin limit ($L < L_c$) has two implications for transport. It was demonstrated that beyond the opening of a TSS energy gap $\Delta(L)$, the close proximity of the Dirac cones with inverted spin orientations allows spin-conserving backscattering and therefore opens an efficient scattering channel for carriers. To enable the interpretation of the experimental data, a semiclassical conductivity model taking both effects into account was derived.

While the gap opening is a known effect in ultra-thin TI films that is experimentally accessible by spectroscopic means, the emergence of the new scattering mechanism was not observed previously due to the required access to the pristine transport properties of the TI. The demonstrated measurement scheme overcomes the associated experimental difficulties, as it allows to probe the TSS conductivity *in situ* as a function of film thickness on a single

sample, which furthermore eliminates the possible influence of inconsistencies from the growth process.

CHAPTER 7

Search for ballistic 1D channels on topological insulator edges

In the previous chapter, the opening of an energy gap as observed in transport measurements in the TSS of a BST thin film was presented. In the transition from a 3D TI thin film to a 2D TI, the observed gap opening Δ is a necessary condition for the establishment of a QSH phase in the thin film. Beyond the formation of an insulating 2D interior, the topological phase transition requires a non-trivial parity of the opened gap. This chapter presents a systematic approach to investigate the corresponding sufficient condition, which is related to the presence of 1D states at the edges of the film.

The experimental procedure is demonstrated on the example of the $(\text{Bi}_{0.16}\text{Sb}_{0.84})_2\text{Te}_3$ thin film that was investigated in the previous chapter. First, the general condition for the formation of edge states in an ultra-thin TI film is outlined. After introducing the measurement principle, the influence of an existing edge state on the 2D potential landscape during a transport measurement is discussed. With the deduced implications for charge transport, the experimental results from two different four-point resistance measurement configurations in the vicinity of TI film edges are evaluated qualitatively. It is shown that in spite of spectroscopic data suggesting the opposite, conducting 1D edge states are not found in the investigated film.

7.1. Transition into two-dimensional topological insulator regime

As discussed in section 6.1, a QSH phase can be realized by reducing the thickness of a TI film (Fig. 7.1). Below a critical thickness, usually 2–5 QL [142, 143], the TSS on the interfaces of the material develop an energy gap $\Delta(L)$, which transforms their band structure according to [140, 144]

$$E_{\pm}(k) = E_0 - Dk^2 \pm \sqrt{(\hbar v_F k)^2 + \left(\frac{\Delta}{2} - Bk^2\right)^2}. \quad (7.1)$$

However, the existence of non-trivial gapless states at the edge of the system is not guaranteed and depends on the invariant ν^{2D} , which is unrelated to the topological nature of the 3D TI [143]. From the massive Dirac model, it is found that topological edge states develop in the opened gap under the condition of $\Delta/B > 0$ [140, 144]. The related Hall conductance of the 2D system is given by

$$\sigma_{xy}^{\pm} = \pm \frac{e^2}{2h} [\text{sgn}(\Delta) + \text{sgn}(B)], \quad (7.2)$$

for each spin type (\pm), such that helical edge modes with quantized conductance appear for $\Delta/B > 0$. In this expression, the term $[\text{sgn}(\Delta) + \text{sgn}(B)]/2$ corresponds to the parity of the opened TSS gap. The resulting helical edge states denote the existence of the QSH phase. It is noted that B and Δ both depend on film thickness L , such that the topological invariant and therefore the existence of helical edge states can change with L [140, 141]. This is important to consider for real TI thin films, since the QSH phase is possibly only expected for specific film thicknesses L .

The transport properties of an edge state of the QSH phase can be understood by applying the Landauer-Büttiker formalism [149, 150]. In the helical 1D channels, carriers moving in one direction have reversed spin orientation with respect to counter-propagating carriers. As this property prohibits backscattering, charge transport in the channels is ballistic in nature. When the 1D edge channel is contacted by source/drain leads and a charge current is induced, the resulting two-terminal conductivity of the channel is given by the quantum of conductance $\sigma_{1D} = \frac{e^2}{h}$. This value is different by a factor of 2 from the two-terminal conductance of a QHE edge mode due to absence of spin degeneracy. The voltage drop causing the finite conductance occurs at the contact leads, while the potential along the 1D channel is constant in correspondence to ballistic transport behavior. Importantly, σ_{1D} is independent of the channel length, contrary to a diffusive 1D conductance, due to the lack of dissipation in the channel itself. In a multi-terminal measurement, the additional voltage-probes along the channel therefore return a potential difference of zero.

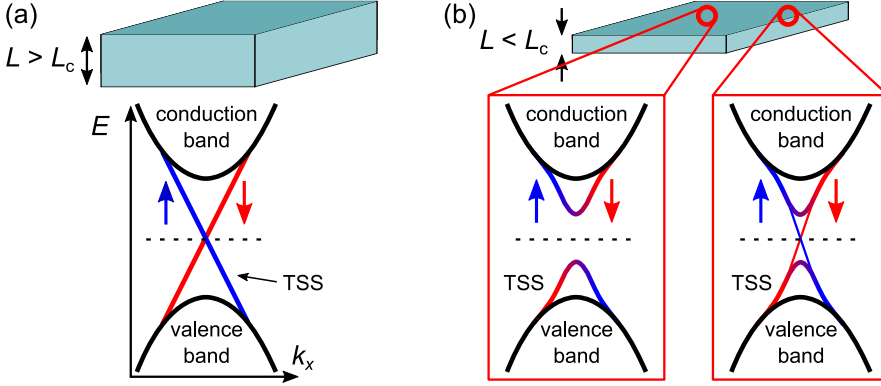


Fig. 7.1.: Sketch of the transition from a 3D TI to a 2D TI by reducing film thickness. **(a)** In a strong TI thin film with $L > L_c$, the system has well separated interfaces, each with a helical Dirac cone in the bulk band gap. **(b)** When the opposite TSS start to interact in the low thickness limit, an additional gap Δ in the surface bands opens, forming a massive Dirac dispersion. If the TI thin film further satisfies $v^{2D} = 1$, a pair of topologically protected 1D edge states at the boundary of the film is formed in the surface gap.

For the case of a trivial ballistic channel that contains N scattering centers between the voltage probes at a distance x , each with a transmission probability of T_0 , the resistance according to the Landauer-Büttiker formalism is given by [151]

$$R = \frac{h}{e^2} \frac{1}{T(N)} = \frac{h}{e^2} \frac{N(1 - T_0) + T_0}{T_0} \quad (7.3)$$

$$= \frac{h}{e^2} \left[1 + \frac{x}{\lambda} \right], \quad (7.4)$$

where $\lambda = \frac{xT_0}{(1-T_0)N}$ is a characteristic scattering length depending on the linear density of scatterers N/x along the channel. This relation reveals a linear distance dependence and describes quasi-ballistic transport with occasional backscattering of charge carriers. In the helical 1D states of a QSH phase however, backscattering is only possible with a simultaneous flipping of the carrier spin due to spin-momentum locking. Non-magnetic scattering centers therefore have no influence on the ballistic resistance of the channel and a constant potential difference is expected in a transport measurement.

7.2. Edge state measurement scheme

To confirm the formation of a QSH phase experimentally, it is required to not only show that the 2D interior of the system is insulating [92, 152, 153], but also to demonstrate the

existence of the topologically protected 1D states at the edges of the sample. By means of transport measurements, this is generally a hard task, as it requires the delicate contacting of the spatially confined transport channels. In addition, any unintended contribution from parasitic background conductivity conceals the conductivity of the edge states and hence impedes their electrical detection. This is further complicated by the fact that the usually required *ex situ* sample preparation is known to destroy the topological properties of the system [31]. While the QSH phase in general has been observed in transport in the past [13, 154], the successful detection of topological edge states in 3D TI films has not been possible, yet.

7.2.1. Scanning tunneling spectroscopy

A frequently used approach to investigate the edge states of topological phases is their detection via scanning tunneling spectroscopy (STS) at different energies. As an STM tip is used to scan across a sample surface, the derivative of the tunneling current with respect to the bias voltage can be acquired simultaneously, yielding a dI/dV map. In first order approximation, the recorded STS signal is proportional to the local density of states at the respective probe position and at the energy $E = eV_b$ corresponding to the bias voltage [155]. The acquisition of the signal is achieved by employing a lock-in technique. During the scanning process, the bias voltage is modulated with an amplitude V_{mod} at a constant frequency to detect the spatial dependence of the density of states parallel to the sample topography.

Similarly, spectroscopic measurements were performed in the frame of this work on the $(\text{Bi}_{0.16}\text{Sb}_{0.84})_2\text{Te}_3$ thin film that was subject of investigations in chapter 6. Figure 7.2 (a) shows the topography of an investigated area, comprising a step edge between 3 QL and 4 QL film thickness. Corresponding spectroscopic dI/dV maps at different sample bias voltages from 1V to 50mV are displayed in Fig. 7.2 (b)–(i). The topographic STM image and the spectroscopic images are recorded in constant-current mode. The dI/dV signal is acquired with a modulation of $V_{\text{mod}} = 30\text{mV}$ at a frequency of $f = 320\text{Hz}$.

At energies larger than 220 meV with respect to the Fermi level at the sample surface, a uniform density of states is observed, as the recorded dI/dV signal shows no spatial variations in the scanned area. In contrast, spectroscopic scans at energies smaller than 220 meV reveal an elevated density of states confined to $\sim 5\text{nm}$ at the step edge between the terraces. Since the signal appears in equal strength in both scanning directions across the step edge in Fig. 7.2, it cannot be attributed to a feedback artifact.

The Fermi level at the top interface of the present $\text{Bi}_{0.16}\text{Sb}_{0.84}\text{Te}_3$ film is known from the interpolation of ARPES measurements [100, 101], as discussed in section 4.2. Its approxi-

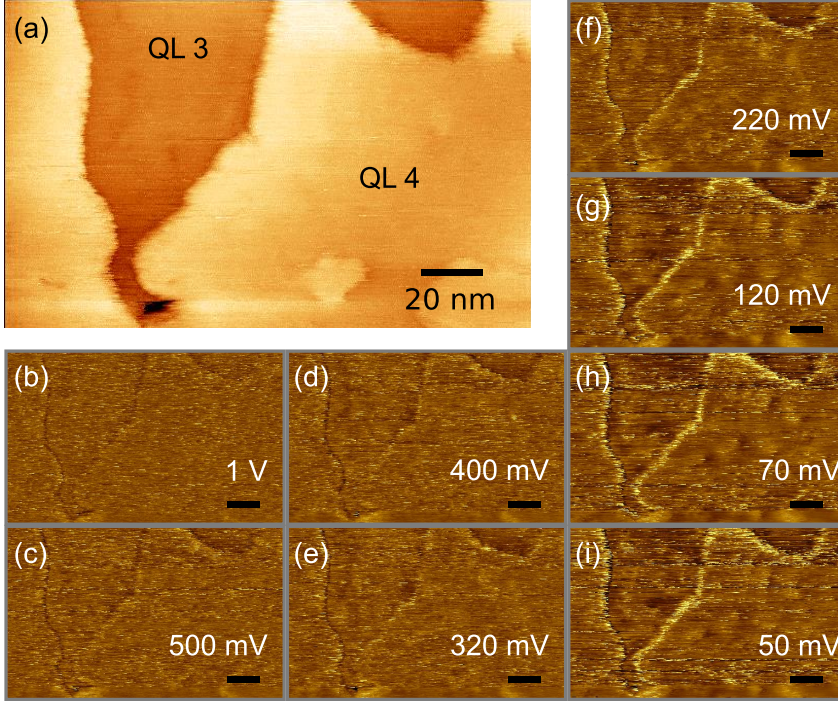


Fig. 7.2.: Scanning tunneling spectroscopy maps at a step edge in a BST thin film. (a) Topography scan of an investigated $170\text{ nm} \times 100\text{ nm}$ sized area featuring a 3QL terrace, a 4QL terrace and a step edge in between. (b)–(i) Spectroscopic dI/dV maps of the area at sample bias voltages between 1V and 50mV. At $V_b > 220\text{ mV}$, a uniform density of states attributed to bulk states is observed. At $V_b < 220\text{ mV}$, a distinct feature along the terrace edge in the dI/dV signal appears, indicating an increased local density of states confined to the step edge.

mate position in the band gap, 50 meV above the Dirac point and $\sim 200\text{ meV}$ below the bulk conduction band, as sketched in Fig. 4.4 (b), is used to interpret the energy dependence of the spectroscopic data. According to the inferred position of $E_{F,t}$, a spectroscopic energy range of $0\text{ meV} < eV_b \lesssim 200\text{ meV}$ would correspond to states in the bulk band gap. As seen from Fig. 7.2 (b)–(i), $eV_b \approx 220\text{ meV}$ denotes the energy above which the enhanced dI/dV signal starts to disappear. It is concluded that this energy corresponds to the bulk conduction band edge and that the observed edge states at energies up to 220 meV are located within the bulk band gap. This value is shifted by 20 meV compared to the expected position of the conduction band from ARPES. This is explained by the poor STS resolution resulting from thermal broadening at room temperature and the modulation amplitude V_{mod} . Furthermore,

the extrapolated position of $E_{F,t}$ in the band gap is primarily valid for films of > 4 QL thickness. In the imaged 3QL/4QL region of the film, the position of the bands with respect to the Fermi level is expected to be shifted. The recorded uniform dI/dV signal in the STS scans beyond 220 meV is attributed to the comparatively high density of states of the bulk conduction band.

In the context of TI thin film samples, characteristic dI/dV signals at step edges like these are usually attributed to topologically protected edge channels [156–158]. However, the observation of a locally increased density of states is to be understood only as an indication. From spectroscopic data alone, it is not clear whether observed states at the TI edge are in fact topologically non-trivial. For a characterization of the topological nature of the observed edge states, it is necessary to measure the local conductivity at the film edges, as only the detection of ballistic transport properties would constitute sufficient evidence.

7.2.2. Nanoscale transport measurements

The detection of spatially confined conductivity on the nanometer scale is enabled by exploiting the maneuverability of the STM tips in four-point measurements. The corresponding transport measurement scheme for transport close to step edges is depicted exemplarily in Fig. 7.3. Due to the small spatial extent of edge states and the wrinkled, irregular contour of the terrace edges, the positioning method outlined in chapter 3 is indispensable for precise contacting.

In the experiment, the STM tips are positioned in a four-point configuration at different step edges using overview STM scans. Two approaches are used to probe the transport contribution of step edges. In one approach, the potential drop along a step edge is probed explicitly by positioning all four tips directly on a step edge and using one voltage-probing tip to follow its contour. An exemplary measurement procedure at the edge of a 2QL film is depicted in Fig. 7.3 (d). The second method entails the implicit detection of the edge contribution by measuring the local potential in a tip alignment parallel to a step edge with one voltage-probing tip being moved perpendicularly. According to this scheme, the electrical properties of step edges of 2, 3 and 4 QL films are investigated. Since the transport experiments are performed *in situ*, the electronic structure of the sample is left intact. In each case, the acquired four-point resistance is compared to finite element calculations based on the known conductivities of the terraces. All of the presented finite element calculations have been performed by Helmut Soltner.

7.3. Four-point resistance measurement directly on a step edge

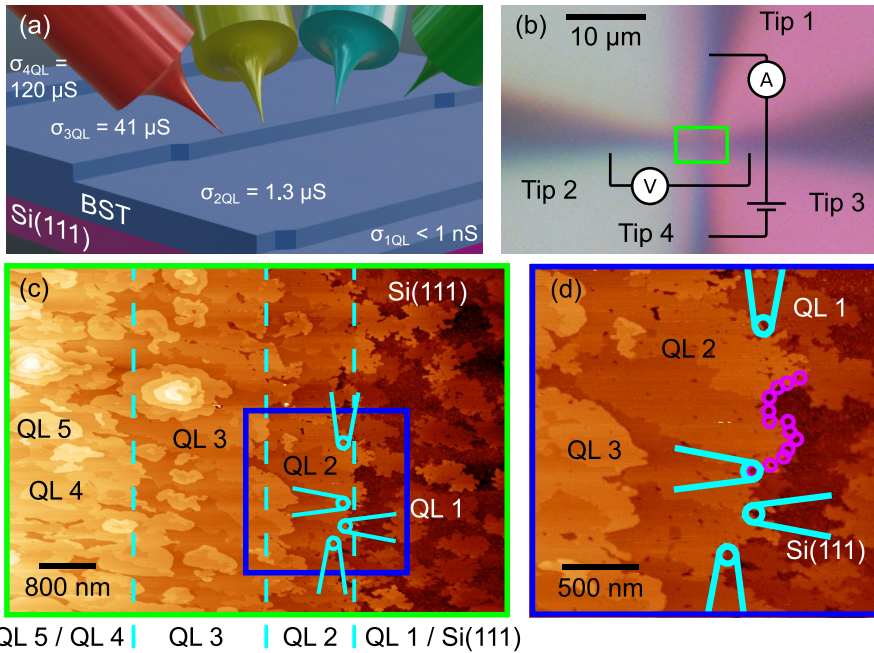


Fig. 7.3.: Edge state conductivity measurement principle on the investigated $\text{Bi}_{0.16}\text{Sb}_{0.84}\text{Te}_3$ thin film. (a) Sketch of the measurement setup. The STM tips are positioned in close proximity to a step edge between two terraces in the boundary region of the film. Position-dependent resistance measurements parallel or perpendicular to the step edge allow to probe possible edge state transport contributions. The artwork was designed by Vasily Cherepanov. (b) Optical microscope image of the tip configuration during a measurement. (c) Overview scan used to bring the tips into position on the 2QL terrace edge. (d) Exemplary position-dependent resistance measurement along the edge of a 2QL terrace. Corresponding tip positions are indicated by the symbols.

7.3. Four-point resistance measurement directly on a step edge

To achieve direct contact to a possible edge state of the TI film, the four STM tips are placed on the step edge of a terrace at well-defined distances. The outer two tips are used to inject a current, while the inner ones act as voltage probes. In the frame of a position-dependent resistance measurement with direct contact to the edge, one of the voltage-probing tips is moved to different positions on the edge contour. By tracing the voltage profile in this manner, the resistance drop along the step edge can be characterized to distinguish between ballistic

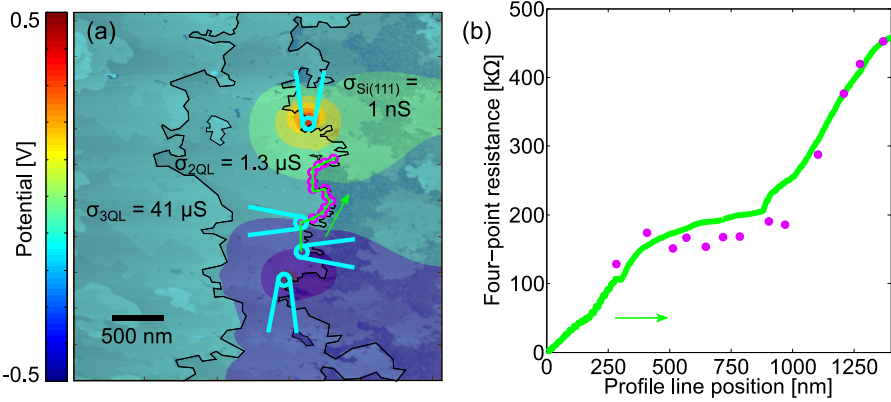


Fig. 7.4.: Four-point resistance measurement in direct contact to the step edge between the 2QL terrace and the Si(111) substrate. **(a)** Topography scan of the investigated area superimposed with the 2D potential landscape resulting from finite element calculations. The terrace edges are highlighted as black lines. With edge states not being considered in the finite element model, the calculated potential originates only from the 2D conductivity of the terraces. **(b)** Measured and calculated four-point resistance as a function of the tip position on the profile line along the 2QL terrace edge. The measured values are represented by purple circles, while the finite element model result is indicated by the green line. The related positions of the voltage probe and the appropriate trace along the step edge are shown in the scan image by corresponding colors. The position dependence of the measured data suggests that there is no ballistic 1D channel along the step edge, which is expected to be constant. This is further supported by the good correspondence to the model resistance, which only considers the 2D conductivity of the terraces.

and diffusive charge transport from its spatial dependence [159–161].

Figure 7.4 presents the results of an according four-point resistance measurement with direct contact to a step edge between a 2QL terrace and the silicon substrate. As indicated by the purple circles in Fig. 7.4 (a), one voltage-probing tip is moved along the terrace edge while the other ones reside at fixed positions with $\sim 1.7 \mu\text{m}$ between the points of current injection. The corresponding measured four-point resistance as a function of distance between the voltage probes along the edge is presented in Fig. 7.4 (b) as purple circles. The recorded resistance is in the order of 100 k Ω and exhibits an approximately linear distance dependence with a kink at the profile line position $\sim 1 \mu\text{m}$, resulting in two segments with different slopes of $\gtrsim 100 \text{ k}\Omega/\mu\text{m}$. Evidently, the four-point resistance demonstrates that there is no ballistic transport behavior at the terrace edge. As discussed above, the four-point resistance R_b^{4P} of a ballistic edge channel is constant along its length, as there is no potential drop in the channel itself. For non-spin-degenerate ballistic channels in general, where the voltage

probes themselves can in principle act as scattering centers, the four-terminal resistance yields $R_b^{4P} = h/e^2 \approx 26 \text{ k}\Omega$ or $R_b^{4P} \approx 0$, depending on whether the voltage probes are invasive or not, respectively [162]. In the case of a QSH material, where backscattering at non-magnetic defects is systematically prevented by helicity, $R_b^{4P} \approx 0$ is expected along the entirety of the step edge. In principle, it is possible that a QSH phase is actually developed, but is concealed by enabled elastic inter-band scattering if the Fermi level is not situated in the surface band gap Δ . At 2QL film thickness, the surface state gap that is opened at the Dirac point of the Sb-rich BST compound is $\Delta \approx 250 \text{ meV}$ [92, 143]. Taking into account the approximate position of the top surface Fermi level $E_{F,t} \approx 50 \text{ meV}$, it is deduced that the Fermi level does not cross the TSS in the band structure. This large separation in energy means that if there are any helical edge states in the surface band gap, they inevitably must appear as ballistic, since elastic scattering into surface states is not possible at the Fermi energy. As a consequence, it is concluded that in case of the investigated 2QL film, helical edge states do not exist at the step edge to the silicon substrate. With the neighboring Si(111) being a topologically trivial system, it follows that a $\text{Bi}_{0.16}\text{Sb}_{0.84}\text{Te}_3$ film of 2QL thickness is also topologically trivial regarding its invariant ν^{2D} .

Complementary to the transport experiment, classical calculations using finite element methods are performed to explore whether the measured four-point resistance is instead explained by the residual parasitic 2D conductivity of the terraces. To this end, the potential landscape is calculated by reconstructing the measurement geometry and solving the related boundary value problem. Here, the measurement geometry is given by the shapes of the terraces, as inferred from the STM scan. The boundary conditions are defined by the positions of the current-injecting tips, where the potential in the model is set to $+0.5 \text{ V}$ and -0.5 V , and the experimentally known conductivities of each terrace that are assigned to the appropriate regions in the reconstructed geometry. Thus, the numeric model only comprises the remaining parasitic 2D conductivity of the terraces and yields the reference potential without edge state contribution. The resulting calculated potential landscape for the specific measurement geometry on the 2QL terrace edge is shown superimposed with the scan image in Fig. 7.4 (a). The contours of the terraces are indicated as black lines.

To compare the numerical results to the measured transport data quantitatively, the potential landscape is used to determine the local four-point resistance $R_{\text{calc}}^{4P} = \Delta V_{\text{calc}} / I_{\text{calc}}$. ΔV_{calc} is inferred directly from the difference of the potential at the positions of the two voltage probes, while I_{calc} is obtained from numerical differentiation of the calculated potential and subsequent integration along a closed path around the position of a current probe. The resulting calculated four-point resistance profile following the contour of the terrace edge according to the tip movement in the experiment is shown as a green curve in Fig. 7.4 (b). The corresponding trace of the profile line and its orientation are also indicated in the scan

image. The profile line position zero corresponds to the position of the static voltage probe. From the quantitative comparison, the measured four-point resistance is in agreement with the simulation results, with even details such as the kink at $\sim 1 \mu\text{m}$ resulting from the specific terrace shape being reproduced by the calculation. Since the numeric model yields the reference potential that only considers the 2D conductivity originating from the TSS as the sole transport channel, the good correspondence of the results agrees with the previous assertion that there are no ballistic states at the 2QL film edge.

7.4. Four-point resistance measurements in proximity to a step edge

The direct contacting of a step edge on the TI film with all four tips is intricate and time consuming as it requires very precise positioning. A tip configuration with much less stringent requirements that can be used to identify 1D channels is achieved by placing the tips in close proximity to a terrace edge, e.g. in a parallel linear arrangement at a lateral distance of Δy . This configuration is depicted conceptually in Fig. 7.5 (a).

In such an arrangement, with the distance Δy to the step edge being smaller than the average tip spacing, an existing 1D edge state can be interpreted as a parallel conduction channel. As described in detail in the next section, an existing edge channel with comparatively high conductivity warps the current density between the injection tips, which is detectable in the probed potential difference. First, however, it is essential to understand to what extent this scenario pertains to the case of a ballistic channel.

In a non-spin-degenerate ballistic channel, a resistance drop of h/e^2 occurs at the contact points, while within the channel itself, the conductivity is infinite, since there is no potential drop in the interior of the channel. In a sense, a ballistic channel can therefore be understood as a highly conductive channel with an entry/exit barrier of h/e^2 . The treatment of a ballistic channel in parallel to the tip arrangement as a classical channel of high conductivity is justified if the two-terminal resistance between the current-injecting tips on the terrace is in the order of h/e^2 . In this case, the ballistic contact resistance appears as transparent, allowing the involvement of the channel in transport. On a two-dimensional sheet, the two-point resistance is given by [34]

$$R_{2D}^{2P} = \frac{1}{\pi\sigma_{2D}} \ln \left[\frac{D-r}{r} \right], \quad (7.5)$$

where D and r are the distance between the current-injecting tips and their contact radius, respectively. In the case of the investigation on the 3QL terrace presented below, with $\sigma_{3QL} = 41 \mu\text{S}$, $D \approx 1.7 \mu\text{m}$ and $r \approx 10 \text{ nm}$, this expression yields $R_{2D}^{2P} \approx 40 \text{ k}\Omega$. Here, r is estimated from

7.4. Four-point resistance measurements in proximity to a step edge

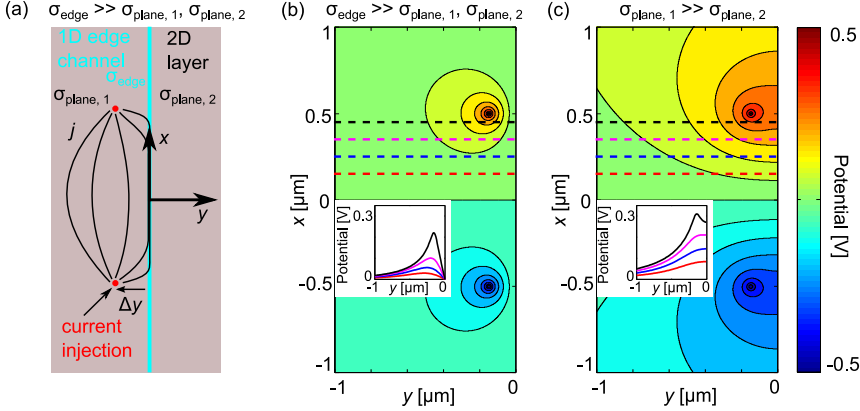


Fig. 7.5.: Influence of a parallel conductive edge channel on the 2D potential landscape. **(a)** Illustration of a parallel tip configuration in close proximity to a conductive 1D channel. The points of current injection are at a lateral distance of $\Delta y = 150 \text{ nm}$ to the step edge at $y = 0$. The latter separates two regions with conductivities $\sigma_{\text{plane},1}$ and $\sigma_{\text{plane},2}$, corresponding to the different terraces in the experiment. **(b)** Potential landscape corresponding to the configuration depicted in (a) with $\sigma_{\text{edge}} \gg \sigma_{\text{plane},1}, \sigma_{\text{plane},2}$. Due to the presence of the conductive edge channel, the potential distribution is distorted with respect to isotropic conditions as described by Eq. 2.20. **(c)** Potential landscape corresponding to the case without a conductive edge channel, but with a low conductivity region at $y > 0$, as present in the experiment. The insets in (b) and (c) show the evolution of the potential perpendicular to the edge orientation at different elevations x . The related traces are indicated by the dashed lines in (b) and (c). The evolution of the potential towards the step edge is characteristic for the two considered limit cases. In case of a highly conducting step edge (b) the potential increases towards the step edge, reaches a maximum and falls to zero at the step edge. In contrast, the potential monotonously rises towards $y = 0$ in the case without an edge channel, as considered in (c). The distinct difference of the potential distribution between these cases can be used to characterize the nature of the step edge conductivity in the experiment.

the average size of the spots observed in post-measurement topography scans, as presented in Fig. 6.7. Since $R_{2D}^{2P} > h/e^2$, the treatment of a parallel ballistic edge state as a highly conductive channel is valid.

7.4.1. Influence of a 1D channel on 2D resistance measurements

With the treatment of a parallel ballistic channel as a spatially confined region of high conductivity σ_{edge} , its influence on the 2D potential landscape can be determined classically. Figure 7.5 (b) presents the analytically determined potential warping caused by the presence of the conductive 1D channel in parallel to the tip arrangement. As illustrated in Fig. 7.5 (a),

the tips are placed at a lateral distance Δy from the channel at $y = 0$, which separates two 2D regions with conductivities $\sigma_{\text{plane},1} \gg \sigma_{\text{plane},2}$, which correspond to the different terraces in the experiment. As a comparison, Fig. 7.5 (c) presents the potential landscape that results without any edge state contribution. In both of the presented limit cases, the potential is obtained by applying the method of mirror images [38], analogous to the example in section 2.2.4. It is to be noted that for the case of $\sigma_{\text{edge}} \gg \sigma_{\text{plane},1}, \sigma_{\text{plane},2}$ the distortion of the electric potential between the tips is identical to that of $\sigma_{\text{plane},2} \gg \sigma_{\text{plane},1}$. This is demonstrated by a comparison to finite element calculations in appendix B.2.

As evident from Fig. 7.5 (b), the presence of a highly conductive edge channel forces the charge current to flow at the edge, which results in a significant potential drop towards the edge position. The potential landscape is thus distorted compared to the symmetric dipole-type potential of an isotropic infinite 2D plane, as described by Eq. 2.20. The detailed evolution of the potential towards the edge along the horizontal dashed lines is presented in the inset.

In the contrary case presented in Fig. 7.5 (c), without a conducting edge channel, while $\sigma_{\text{plane},1} \gg \sigma_{\text{plane},2}$ (as present in the experiment), the current is inhibited from entering the low conducting half plane and the distortion of the potential is opposite. As evident from the inset, the potential increases monotonously towards the step edge and up to a constant elevated level. This potential distribution is identical to the potential resulting from a termination of the 2D plane as discussed in section 2.2.4.

The two discussed limit cases, experimentally corresponding to the presence/absence of a conductive 1D channel between two TI terraces of different 2D conductivity, yield characteristically different potential distributions. The different evolution of the potential perpendicular to the orientation of the step edge can be used qualitatively to determine whether a ballistic 1D state is present.

7.4.2. Measurement results

According transport measurements in proximity to a step edge are performed on the 3QL terrace of the TI sample, as presented in Fig. 7.6. The STM tips are positioned in a linear configuration in parallel to the average orientation of the step edge to the 2QL terrace, at a lateral distance of $\Delta y \approx 200$ nm. In the experiment, the two outer tips at a distance of $D \approx 1.7 \mu\text{m}$ inject a current of $\sim 10 \mu\text{A}$. Within the scope of the four-point resistance measurements, one of the inner voltage-probing tips is moved to different positions perpendicular to the tip arrangement over a range of $\sim 3 \mu\text{m}$. By doing so, the position-dependent resistance is acquired along the perpendicular profile line in vicinity to the two opposite step edges of

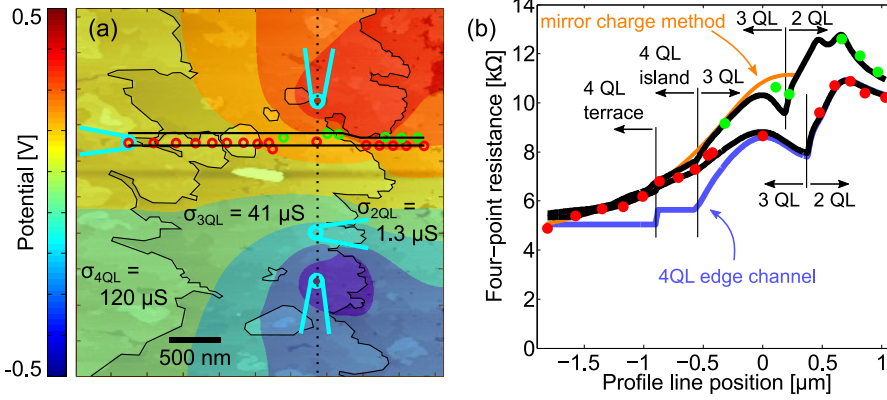


Fig. 7.6.: Four-point resistance measurement on a 3QL thin film in proximity to a step edge. **(a)** Topography scan of the investigated area superimposed with finite element calculation results. As indicated by the cyan symbols, the STM tips are placed at a distance of $\Delta y \approx 200$ nm to the step edge bordering the 2QL film. In the experiment, the local four-point resistance is acquired at different positions of one of the voltage-probing tips, as indicated by red and green circles. The calculated potential landscape considers only the 2D conductivity of the three terraces. **(b)** Measured and calculated four-point resistance along the horizontal profile lines indicated in the scan image. As evident from the correspondence to the two black curves, the experimental data denoted by red and green circles is accurately described by the finite element model based on the terrace conductivity alone. An analytic fit to the data according to Eq. 2.43 is represented by the orange curve. The analytic model assumes a straight film boundary at $\Delta y = 250$ nm with $\sigma_{3QL} \gg \sigma_{2QL}$ and constitutes a good approximation for the measured resistance. The blue curve, denoting the expected resistance profile that is obtained from an inclusion of a narrow region with $\sigma_{edge} \gg \sigma_{4QL}$ at the 4QL film edge in the finite element calculations, does not reproduce the measured data. Based on the behavior of the resistance close to the two step edges, the presence of conductive channels at the edges of the 3QL terrace is excluded.

the 3QL terrace and also beyond, in the 4QL and 2QL film regions. The probed positions are indicated by red and green circles in the scan image in Fig. 7.6 (a). The corresponding four-point resistance as a function of profile line position is presented in Fig. 7.6 (b) by correspondingly colored dots. A profile line position of zero corresponds to the symmetry axis defined by the tip configuration, which is indicated as a dotted line in the scan image.

In the region of the 3QL terrace, the evolution of the resistance on the perpendicular axis can be compared to the limit cases presented in Fig. 7.5 to deduce whether a ballistic channel is present at the two step edges of the 3QL film. The comparison is reasonable, since the four-point resistance directly corresponds to the electric potential up to a proportionality factor and an offset. As estimated above by Eq. 7.5, a ballistic edge state in the present case can

be treated classically as a parallel region of high conductivity σ_{edge} due to the comparatively high two-point resistance compared to the ballistic contact resistance h/e^2 .

From qualitative comparison, it is apparent that the behavior of the measured resistance close to the step edge between 3QL and 2QL resembles that of Fig. 7.5 (c), where $\sigma_{3\text{QL}} \gg \sigma_{2\text{QL}}$ without a conductive 1D edge channel is assumed. In both instances, the potential/resistance profile increases towards the step edge, as opposed to the model with high edge conductivity in Fig. 7.5 (b). At the opposite side of the terrace, towards the 4QL film, the local four-point resistance is observed to decrease slowly and continue to do so, even beyond the edge in the 4QL region at profile line positions $< -0.5\mu\text{m}$. This behavior is also not what is expected from a conductive 1D channel, which contrarily would force a drastic potential drop towards the step edge. Moreover, a highly conductive channel at the terrace edge would screen the 4QL region beyond from the induced electric field, causing the surface of the 4QL film to be an equipotential area.

As a first approximation, the measured resistance data in the 3QL region is explained by applying the mirror image method as outlined in section 2.2.4. By assuming insulating behavior in the 2QL region and approximating the step edge in between as a straight vertical line, Eq. 2.43 is used to describe the resistance. The corresponding fit, with a model parameter of $\Delta y \approx 250\text{ nm}$ is denoted by the orange line in Fig. 7.6 (b). Evidently, the mirror image model reproduces the trend of the data well, even with the irregular contour of the edge unaccounted for.

Altogether, the similarity of the position-dependent resistance in the experiment to the model considering no enhanced edge conductivity suggests that there is no indication of ballistic channels at the edges of the 3QL film.

In addition to the above considerations, finite element calculations are performed to obtain the reference potential that results from the known 2D terrace conductivities. The topography of the investigated film area is used as the model input, resulting in the potential landscape that is superimposed with the scan image in Fig. 7.6 (a). Following from this result, the calculated local four-point resistance is compared to the measured data along the two horizontal black lines in the scan image (Fig. 7.6 (a)), which correspond to the movement of the voltage-probing tip in the experiment. The respective resistance profile is represented by the two black curves in Fig. 7.6 (b). Evidently, the correspondence of the finite element result to the experimental data is exceptionally good. Even the details of the measured resistance profile that originate from the specific shape of the terrace are reproduced by the numeric model. With conductive edge states not being included in the calculation, the agreement implies that the measured resistance is fully explained by the parasitic 2D conductivities of the terraces alone.

To emulate the potential landscape that would result from an edge channel at the 4 QL film, the configuration in Fig 7.6 (a) is used to perform an additional finite element calculation, including a highly conductive region with $\sigma_{\text{edge}} \gg \sigma_{4\text{QL}}$ along the respective step edge. The corresponding four-point resistance along the horizontal profile line is denoted as a blue curve in Fig. 7.6 (b). In agreement with the intuitive expectation discussed above, the model resistance exhibits a sharp decrease towards the step edge, at profile line positions of $> -0.5\mu\text{m}$. Beyond the step edge, in the 4 QL film region, the constant resistance denotes the existence of an equipotential area. This calculation result vastly differs from the measured local four-point resistance.

Again, it is to be noted that, since the finite element calculations are based on a classical resistance model, they do not consider the contact resistance $R_b = h/e^2$ that the charge carriers have to overcome to even enter a possible ballistic channel. The comparison to the model results is however still reasonable due to the comparatively high two-terminal resistance on the 2D terrace determined by Eq. 7.5.

In total, the measurements on the 3 QL film in proximity to a terrace edge show no indication of ballistic channels at the step edges to the 2 QL and the 4 QL region. Instead, the acquired four-point resistance is explained entirely by the residual 2D conductivity of the TSS as the sole contribution to transport. This finding has two possible reasons. If the Fermi level is situated in the TSS band gap Δ of the investigated film, the experimental data is only explained by an actual absence of topological edge states in the system. With the 2 QL film being topologically trivial regarding ν^{2D} , this assertion would imply that the material is confirmed to not host a QSH phase at 3 QL and 4 QL thickness, as well. If, on the other hand, the Fermi level crosses the surface bands, the elastic scattering of carriers from the edge state into the TSS on the vicinal terrace is enabled, resulting in the deterioration of the ballistic properties of the channel. In this case, a possible formation of a QSH phase in the band gap cannot be entirely excluded. In case of the present $(\text{Bi}_{0.16}\text{Sb}_{0.84})_2\text{Te}_3$ thin film, the size of the opened TSS band gap is estimated to 60 meV and 25 meV for 3 QL and 4 QL thickness, respectively [92, 143]. The position of the Fermi level is only known for the full film thickness of 12 QL. Since its location in the band structure is generally dependent on the film thickness, both of the outlined reasons for the absence of ballistic channels are possible. *Ab initio* calculations of the topological 2D invariant based on the known atomic composition of the investigated film yield $\nu^{2D} = 0$ for film thicknesses $\leq 5\text{QL}$ ¹. Complementary to the experimental transport investigation, it is therefore suggested that $(\text{Bi}_{0.16}\text{Sb}_{0.84})_2\text{Te}_3$ films do not exhibit a transition into a QSH phase with reduced thickness.

¹Private communication. *GW* calculations performed by Irene Aguilera.

7.5. Summary

In this chapter, a scheme for the investigation of topological insulator thin films regarding indications of a QSH phase was presented. In the ultra-thin limit of a 3D TI film, the opening of a band gap in the Dirac cone due to the interaction of the TSS, as investigated in chapter 6, constitutes a necessary condition of the phase transition into a QSH insulator. Using the same structured $(\text{Bi}_{0.16}\text{Sb}_{0.84})_2\text{Te}_3$ sample as in chapter 6, the possible presence of ballistic edge states, which constitute the sufficient condition for the topological phase transition, was studied with various methods.

As a first approach, scanning tunneling spectroscopy measurements were performed in a sample region with a step edge between the 3 QL and 4 QL film. In the spectroscopic results, a dI/dV signal was revealed at the step edge at bias voltages that coincide with the bulk band gap of the sample, indicating a spatially confined local density of states that is increased with respect to the 2D background.

Beyond the spectroscopic results, which indicate the presence of edge states, nanoscale transport measurements were performed to characterize the electrical properties of various step edges. In the wedge shaped boundary region of the TI sample, the transport contribution of individual terrace edges was examined based on two approaches. By directly contacting the step edge between a 2 QL film and the underlying substrate, a position-dependent four-point resistance measurement was performed along the corresponding edge. With a relatively large resistance drop observed along its contour, contrary to the expectation from a ballistic channel, the formation of a QSH phase was excluded in the 2 QL film. Instead, the acquired resistance along the step edge was explained by a finite element calculation based on the known thickness-dependent 2D conductivity of the thin film. Additionally, nanoscale four-point measurements on a 3 QL film were performed in a tip configuration parallel to an adjacent step edge, with one of the voltage probes being moved perpendicularly across three terraces. The position-dependent behavior of the measured resistance in proximity to the edge indicated an absence of ballistic edge channels at both edges of the 3 QL film. Again, the experimental data was found to be reproduced in detail by finite element calculations relying on the residual 2D conductivity of the TSS alone. The implications of the absence of ballistic edge channels on the 3 QL film for the formation of a QSH phase were discussed.

In general, it was shown that in spite of an observed increase in the density of states at terrace edges, experimentally detected by a localized increase in the dI/dV signal, ballistic edge channels are absent in the thin film. This emphasizes that spectroscopic signals on TI samples are to be understood only as a requirement of a QSH phase.

Conclusion and outlook

Within the scope of this work, the characteristic properties of different topological insulator thin films were investigated on the nanometer scale by means of charge transport measurements. Generally, an accessible way to study the characteristic topological surface states of 3D TIs is given by spectroscopic methods, which can reveal the band structure of the system. However, the manifestation of the topological properties in charge transport and their significance for possible device applications can only be studied by electrical measurements. Such studies are accompanied by various obstacles due to the nature of conventional transport measurements. The realization of external electrical contacts usually entails the *ex situ* deposition of material and implies multiple lithographic preparation steps, leaving the topological insulator sample exposed to atmospheric conditions for extended periods of time. Such exposure is known to deteriorate the surface states and therefore is detrimental to the purpose of the investigation. Furthermore, lithographically fabricated structures result in extended and generally undefined contact areas, which introduces a further uncertainty of what is actually measured in a transport experiment. Additionally, the immobile electrical contacts restrict the geometry to only one predetermined measurement configuration, which does not allow to study the spatial dependence of charge transport. For these reasons, the conclusive demonstration of topological transport properties in electrical measurements is hard to achieve.

Here, the use of a room temperature multi-tip STM allows to circumvent these difficulties. With the individual STM tips acting as electrical contacts, no sample processing is needed and transport measurements can be realized after UHV transfer fully *in situ*, which leaves the electronic structure of the TI intact. Precise piezoelectric control of the tips allows to establish

delicate electric contact to the sample, guaranteeing absolutely minimal invasiveness. Over the course of an investigation, the variation of tip positions enables access to the inter-tip distance as a further parameter.

The basic principle of the measurement procedure, including the relation of the measured quantities to intrinsic properties of the sample, depending on the dimensionality of the system, was outlined in chapter 2. Additionally, the principle was demonstrated on the example of thermally treated SrTiO₃, which was observed to exhibit a continuous transition from a 2D to a 3D conductor with increased thermal reduction. To access charge transport properties with vastly enhanced spatial resolution, an advanced positioning method was elaborated and presented in chapter 3. Being based on overlaps of STM scans with each of the four tips, this method allows to realize measurement configurations that are otherwise impossible to achieve and require either a small uncertainty of tip positions or small inter-tip distances, as is the case in the measurements presented in chapters 5 – 7. In these chapters, thin films based on the ternary alloy system of (Bi_{1-x}Sb_x)₂Te₃ were investigated systematically by the four-point probe technique.

The electrical detection of the helical spin texture of the topological surface states was presented in chapter 5. Using a specifically prepared ferromagnetic STM tip, the spin-dependent electrochemical potential that results from current injection in a TI was extracted from distance-dependent four-point resistance measurements. While no spin signal was observed in a (Bi_{0.53}Sb_{0.47})₂Te₃ film due to an unfavorable position of the Fermi level in the Dirac cone, corresponding measurements in case of (Bi_{0.06}Sb_{0.94})₂Te₃ revealed a finite spin voltage that reverses its sign upon inversion of the tip magnetization direction. From the measured spin-dependent potential, a degree of spin polarization close to its maximum value was estimated.

Chapter 6 featured the investigation of the interaction between the two opposite topological surface states of a (Bi_{0.16}Sb_{0.84})₂Te₃ thin film and the corresponding manifestation in charge transport. On a single structured sample, the sheet conductivity, as inferred from nanoscale four-point measurements, was determined as a function of film thickness. It was demonstrated that below a critical thickness of 5 QL, a hybridization of the surface states occurs. In the non-interacting regime above this thickness, the current was confirmed to be carried exclusively by the topological surface states. Based on the known band structure of the system, the observed exponential drop of the sheet conductivity was found to be explained by an emerging spin-conserving scattering mechanism between the two opposite surface states.

To confirm the successful transition into a QSH phase in the ultra-thin film limit of a 3D TI, it is required to demonstrate the existence of ballistic 1D channels at the edge of the TI film beyond the interaction of the surface states. For this purpose, an according measurement scheme was

demonstrated on the $(\text{Bi}_{0.16}\text{Sb}_{0.84})_2\text{Te}_3$ film in chapter 7. By contacting a 2QL film edge with all four tips directly on the nanometer scale and probing the resistance along its contour, it was shown that no ballistic states exist at the corresponding edge and the 2QL film therefore forms no QSH phase. In the case of a more simple tip configuration, in close proximity to the film edge, the influence of an adjacent ballistic 1D channel on the measured local resistance was elaborated. The expected result was compared to the measured resistance profile across several terrace edges, leading to the conclusion that no ballistic states are situated at the edges of the 4QL and the 3QL film. Instead, the acquired position-dependent four-point resistance was explained in detail by a classical finite element model considering only the 2D conductivity of the residual surface states. While no indications of a topological phase transition were found in case of the investigated $(\text{Bi}_{0.16}\text{Sb}_{0.84})_2\text{Te}_3$ film, the demonstrated scheme constitutes a generic method for the detection of topological phases by means of multi-tip STM.

In future projects, the presented measurements can possibly be combined and extended to probe other topologically non-trivial systems. In particular, Bi_2Te_3 is predicted to undergo a topological phase transition into a QSH insulator state and therefore is a system that could be studied with the shown techniques. Contrary to the Sb-rich ternary composition that was investigated in this work and that was chosen for the advantageous position of its Fermi level in the band gap, topological edge states are therefore expected for Bi_2Te_3 in the ultra-thin film limit. Moreover, similar to the approach in chapter 5, a ferromagnetic tip can be used as a spin-dependent detector in contact to a thin film edge to further solidify the helical nature of QSH states. In case of Bi_2Te_3 , however, such a measurement requires gate controllability, since the Fermi level is situated in the bulk conduction band of the system. Further studies on thin films in general should involve the use of gate control. The sophisticated interpretation of measured electrical properties heavily relies on knowing details of the band structure of the investigated system. In multiple instances of this work, corresponding quantities were either estimated or extrapolated from previous studies. Additionally, an extension of the instrumental capabilities to allow for an increase in the experimental parameter space is a worthwhile effort for any future projects. For instance, investigations in a low temperature multi-tip STM, preferably with the possibility to apply a magnetic field would open a wide range of experimental options for sample characterization. The experimental access to these traditional parameters of transport measurements, combined with the advantages of the multi-tip STM as it is, would result in a truly ideal instrument for electrical measurements.

Bibliography

- [1] F. Capasso, *Band-gap engineering: From physics and materials to new semiconductor devices*. *Science* **235**, 172 (1987). DOI:10.1126/science.235.4785.172 1
- [2] C. G. Smith, *Low-dimensional quantum devices*. *Reports on Progress in Physics* **59**, 235 (1996). DOI:10.1088/0034-4885/59/2/003
- [3] M. Grundmann, *Quantum devices of reduced dimensionality*, in: *Encyclopedia of Condensed Matter Physics*, 17–22 (Elsevier, Oxford, 2005), ISBN 978-0-12-369401-0, DOI: <https://doi.org/10.1016/B0-12-369401-9/00500-3> 1
- [4] R. Tsu and L. Esaki, *Tunneling in a finite superlattice*. *Applied Physics Letters* **22**, 562 (1973). DOI:10.1063/1.1654509 1
- [5] L. L. Chang, L. Esaki, and R. Tsu, *Resonant tunneling in semiconductor double barriers*. *Applied Physics Letters* **24**, 593 (1974). DOI:10.1063/1.1655067
- [6] N. Yokoyama, K. Imamura, S. Muto, S. Hiyamizu, and H. Nishi, *A new functional, resonant-tunneling hot electron transistor (RHET)*. *Japanese Journal of Applied Physics* **24**, L853 (1985). DOI:10.1143/jjap.24.l853 1
- [7] R. Ashoori, *Electrons in artificial atoms*. *Nature* **379**, 413 (1996). DOI:10.1038/379413a0 1
- [8] L. Zhuang, L. Guo, and S. Y. Chou, *Silicon single-electron quantum-dot transistor switch operating at room temperature*. *Applied Physics Letters* **72**, 1205 (1998). DOI:10.1063/1.121014 1
- [9] S. Datta and B. Das, *Electronic analog of the electro-optic modulator*. *Applied Physics Letters* **56**, 665 (1990). DOI:10.1063/1.102730 1
- [10] Y. Tokura, M. Kawasaki, and N. Nagaosa, *Emergent functions of quantum materials*. *Nature Physics* **13**, 1056 (2017). DOI:10.1038/nphys4274 1

- [11] B. Keimer, *The physics of quantum materials*. *Nature Physics* **13**, 1045 (2017). DOI: 10.1038/nphys4302 1
- [12] C. L. Kane and E. J. Mele, *Z₂ Topological Order and the Quantum Spin Hall Effect*. *Phys. Rev. Lett.* **95**, 146802 (2005). DOI:10.1103/PhysRevLett.95.146802 1, 43
- [13] M. König, S. Wiedmann, C. Brüne, A. Roth, H. Buhmann, L. W. Molenkamp, X.-L. Qi, and S.-C. Zhang, *Quantum Spin Hall Insulator State in HgTe Quantum Wells*. *Science* **318**, 766 (2007). DOI:10.1126/science.1148047 1, 44, 102
- [14] B. A. Bernevig, T. L. Hughes, and S.-C. Zhang, *Quantum Spin Hall Effect and Topological Phase Transition in HgTe Quantum Wells*. *Science* **314**, 1757 (2006). DOI:10.1126/science.1133734 1, 44
- [15] Y. Xia, D. Qian, D. Hsieh, L. Wray, A. Pal, H.-H. Lin, A. Bansil, D. Grauer, Y. Hor, R. J. Cava, and M. Z. Hasan, *Observation of a large-gap topological-insulator class with a single Dirac cone on the surface*. *Nat. Phys.* **5**, 398 (2009). DOI:10.1038/nphys1274 2, 45, 60
- [16] I. Zutic, J. Fabian, and S. Das Sarma, *Spintronics: Fundamentals and applications*. *Rev. Mod. Phys.* **76**, 323 (2004). DOI:10.1103/RevModPhys.76.323 2, 53
- [17] D. P. DiVincenzo, *Quantum computation*. *Science* **270**, 255 (1995). DOI:10.1126/science.270.5234.255 2
- [18] D. P. DiVincenzo, *The physical implementation of quantum computation*. *Fortschritte der Physik* **48**, 771 (2000). DOI:10.1002/1521-3978(200009)48:9/11<771::AID-PROP771>3.0.CO;2-E 2
- [19] F. Arute *et al.*, *Quantum supremacy using a programmable superconducting processor*. *Nature* **574**, 505 (2019). DOI:10.1038/s41586-019-1666-5 2
- [20] J. R. Williams, A. J. Bestwick, P. Gallagher, S. S. Hong, Y. Cui, A. S. Bleich, J. G. Analytis, I. R. Fisher, and D. Goldhaber-Gordon, *Unconventional Josephson Effect in Hybrid Superconductor-Topological Insulator Devices*. *Phys. Rev. Lett.* **109**, 056803 (2012). DOI:10.1103/PhysRevLett.109.056803 2
- [21] Y. Makhlin, G. Schön, and A. Shnirman, *Quantum-state engineering with Josephson-junction devices*. *Rev. Mod. Phys.* **73**, 357 (2001). DOI:10.1103/RevModPhys.73.357 2
- [22] A. Kitaev, *Fault-tolerant quantum computation by anyons*. *Annals of Physics* **303**, 2 (2003). DOI:https://doi.org/10.1016/S0003-4916(02)00018-0 2

- [23] C. Nayak, S. H. Simon, A. Stern, M. Freedman, and S. Das Sarma, *Non-Abelian anyons and topological quantum computation*. *Rev. Mod. Phys.* **80**, 1083 (2008). DOI:10.1103/RevModPhys.80.1083
- [24] S. Das Sarma, M. Freedman, and C. Nayak, *Majorana zero modes and topological quantum computation*. *npj Quantum Materials* **1**, 15001 (2015). DOI:10.1038/npjqi.2015.1 2
- [25] L. Fu and C. L. Kane, *Superconducting Proximity Effect and Majorana Fermions at the Surface of a Topological Insulator*. *Phys. Rev. Lett.* **100**, 096407 (2008). DOI:10.1103/PhysRevLett.100.096407 2, 53
- [26] T. D. Stanescu, J. D. Sau, R. M. Lutchyn, and S. Das Sarma, *Proximity effect at the superconductor–topological insulator interface*. *Phys. Rev. B* **81**, 241310 (2010). DOI: 10.1103/PhysRevB.81.241310 2
- [27] I. Shiraki, F. Tanabe, R. Hobarra, T. Nagao, and S. Hasegawa, *Independently driven four-tip probes for conductivity measurements in ultrahigh vacuum*. *Surface Science* **493**, 633 (2001). DOI:https://doi.org/10.1016/S0039-6028(01)01276-6 2
- [28] V. Cherepanov, E. Zubkov, H. Junker, S. Korte, M. Blab, P. Coenen, and B. Voigtländer, *Ultra compact multitip scanning tunneling microscope with a diameter of 50 nm*. *Review of Scientific Instruments* **83**, 033707 (2012). DOI:10.1063/1.3694990 2, 4
- [29] J. G. Analytis, J.-H. Chu, Y. Chen, F. Corredor, R. D. McDonald, Z. X. Shen, and I. R. Fisher, *Bulk Fermi surface coexistence with Dirac surface state in Bi_2Se_3 : A comparison of photoemission and Shubnikov–de Haas measurements*. *Phys. Rev. B* **81**, 205407 (2010). DOI:10.1103/PhysRevB.81.205407 2
- [30] D. Kong, J. J. Cha, K. Lai, H. Peng, J. G. Analytis, S. Meister, Y. Chen, H.-J. Zhang, I. R. Fisher, Z.-X. Shen, and Y. Cui, *Rapid Surface Oxidation as a Source of Surface Degradation Factor for Bi_2Se_3* . *ACS Nano* **5**, 4698 (2011). DOI:10.1021/nn200556h
- [31] P. Ngabonziza, R. Heimbuch, N. de Jong, R. A. Klaassen, M. P. Stehno, M. Snelder, A. Solmaz, S. V. Ramankutty, E. Frantzeskakis, E. van Heumen, G. Koster, M. S. Golden, H. J. W. Zandvliet, and A. Brinkman, *In situ spectroscopy of intrinsic Bi_2Te_3 topological insulator thin films and impact of extrinsic defects*. *Phys. Rev. B* **92**, 035405 (2015). DOI:10.1103/PhysRevB.92.035405 2, 102
- [32] V. Cherepanov, P. Coenen, and B. Voigtländer, *A nanopositioner for scanning probe microscopy: The KoalaDrive*. *Review of Scientific Instruments* **83**, 023703 (2012). DOI: 10.1063/1.3681444 3

- [33] S. Just, *Disentangling parallel conduction channels by charge transport measurements on surfaces with a multi-tip scanning tunneling microscope*, Ph.D. thesis, Zentralbibliothek Verlag, RWTH Aachen University, Forschungszentrum Jülich GmbH (2021) **4**, 58
- [34] Voigtländer, B., Cherepanov, V., Korte, S., Leis, A., Cuma, D., Just, S., and Lüpke, F., *Invited Review Article: Multi-tip Scanning Tunneling Microscopy: Experimental Techniques and Data Analysis*. *Review of Scientific Instruments* **89**, 101101 (2018). DOI: 10.1063/1.5042346 **4**, 5, 34, 108
- [35] T. Hallam, M. J. Butcher, K. E. J. Goh, F. J. Ruess, and M. Y. Simmons, *Use of a scanning electron microscope to pattern large areas of a hydrogen resist for electrical contacts*. *Journal of Applied Physics* **102**, 034308 (2007). DOI:10.1063/1.2736873 **5**
- [36] C. Durand, M. Berthe, Y. Makoudi, J.-P. Nys, R. Leturcq, P. Caroff, and B. Grandidier, *Persistent enhancement of the carrier density in electron irradiated InAs nanowires*. *Nanotechnology* **24**, 275706 (2013). DOI:10.1088/0957-4484/24/27/275706 **30**
- [37] C. Blömers, T. Grap, M. I. Lepsa, J. Moers, S. Trellenkamp, D. Grützmacher, H. Lüth, and T. Schäpers, *Hall effect measurements on InAs nanowires*. *Applied Physics Letters* **101**, 152106 (2012). DOI:10.1063/1.4759124 **5**, 30
- [38] L. B. Valdes, *Resistivity Measurements on Germanium for Transistors*. *Proceedings of the IRE* **42**, 420 (1954). DOI:10.1109/JRPROC.1954.274680 **13**, 15, 110
- [39] K. van Benthem, C. Elsässer, and R. H. French, *Bulk electronic structure of SrTiO₃: Experiment and theory*. *Journal of Applied Physics* **90**, 6156 (2001). DOI:10.1063/1.1415766 **16**
- [40] A. Schindlmayr, C. Friedrich, E. Sasioglu, and S. Blügel, *First-Principles Calculation of Electronic Excitations in Solids with SPEX*. *Zeitschrift für Physikalische Chemie* **224** (2011). DOI:10.1524/zpch.2010.6110 **16**
- [41] A. Spinelli, M. A. Torija, C. Liu, C. Jan, and C. Leighton, *Electronic transport in doped SrTiO₃: Conduction mechanisms and potential applications*. *Phys. Rev. B* **81**, 155110 (2010). DOI:10.1103/PhysRevB.81.155110 **16**, 17
- [42] R. Moos and K. Haerdtl, *Defect chemistry of donor-doped and undoped strontium titanate ceramics between 1000 ° and 1400 ° C*. *J. Am. Ceram. Soc.* **80**, 2549 (1997). DOI:10.1111/j.1151-2916.1997.tb03157.x **16**
- [43] R. Waser, R. Dittmann, G. Staikov, and K. Szot, *Redox-Based Resistive Switching Memories - Nanoionic Mechanisms, Prospects and Challenges*. *Adv. Mater.* **21**, 2632 (2009). DOI:10.1002/adma.200900375 **16**, 22, 24, 26

- [44] O. N. Tufte and P. W. Chapman, *Electron Mobility in Semiconducting Strontium Titanate*. *Phys. Rev.* **155**, 796 (1967). DOI:10.1103/PhysRev.155.796 17
- [45] H. P. R. Frederikse, W. R. Thurber, and W. R. Hosler, *Electronic Transport in Strontium Titanate*. *Phys. Rev.* **134**, A442 (1964). DOI:10.1103/PhysRev.134.A442
- [46] D. Parker and J. Yahia, *ac Hall Measurements in Crystals of Strontium Titanate from 190 to 500° K: Dependence of Hall Mobility on Charge-Carrier Density*. *Phys. Rev.* **169**, 605 (1968). DOI:10.1103/PhysRev.169.605
- [47] C. Lee, J. Yahia, and J. L. Brebner, *Electronic conduction in slightly reduced strontium titanate at low temperatures*. *Phys. Rev. B* **3**, 2525 (1971). DOI:10.1103/PhysRevB.3.2525 17, 20
- [48] K. Szot, W. Speier, R. Carius, U. Zastrow, and W. Beyer, *Localized Metallic Conductivity and Self-Healing during Thermal Reduction of SrTiO₃*. *Phys. Rev. Lett.* **88**, 075508 (2002). DOI:10.1103/PhysRevLett.88.075508 17, 20, 22, 25
- [49] M. S. J. Marshall, A. E. Becerra-Toledo, L. D. Marks, and M. R. Castell, *Surface and Defect Structure of Oxide Nanowires on SrTiO₃*. *Phys. Rev. Lett.* **107**, 086102 (2011). DOI:10.1103/PhysRevLett.107.086102 17
- [50] S. Gerhold, Z. Wang, M. Schmid, and U. Diebold, *Stoichiometry-driven switching between surface reconstructions on SrTiO₃(001)*. *Surface Science* **621**, L1 (2014). DOI: 10.1016/j.susc.2013.10.015 17
- [51] C. Rodenbücher, P. Meuffels, G. Bihlmayer, W. Speier, H. Du, A. Schwedt, U. Breuer, C.-L. Jia, J. Mayer, R. Waser, and K. Szot, *Electrically controlled transformation of memristive titanates into mesoporous titanium oxides via incongruent sublimation*. *Sci. Rep.* **8**, 3374 (2018). DOI:10.1038/s41598-018-22238-4 18
- [52] K. Szot, W. Speier, G. Bihlmayer, and R. Waser, *Switching the Electrical Resistance of Individual Dislocations in Single-Crystalline SrTiO₃*. *Nat. Mater.* **5**, 312 (2006). DOI: 10.1038/nmat1614 21, 22
- [53] D. Wrana, C. Rodenbücher, W. Belza, K. Szot, and F. Krok, *In situ study of redox processes on the surface of SrTiO₃ single crystals*. *Applied Surface Science* **432**, 46 (2018). DOI: 10.1016/j.apsusc.2017.06.272 21, 22, 27
- [54] S. Just, H. Soltner, S. Korte, V. Cherepanov, and B. Voigtländer, *Surface conductivity of Si(100) and Ge(100) surfaces determined from four-point transport measurements using an analytical N-layer conductance model*. *Phys. Rev. B* **95**, 075310 (2017). DOI: 10.1103/PhysRevB.95.075310 21, 24

- [55] D. Marrocchelli, L. Sun, and B. Yildiz, *Dislocations in SrTiO₃: Easy To Reduce but Not so Fast for Oxygen Transport*. *Journal of the American Chemical Society* **137**, 4735 (2015). DOI:10.1021/ja513176u 21
- [56] D. D. Cuong, B. Lee, K. M. Choi, H.-S. Ahn, S. Han, and J. Lee, *Oxygen Vacancy Clustering and Electron Localization in Oxygen-Deficient SrTiO₃: LDA + U Study*. *Phys. Rev. Lett.* **98**, 115503 (2007). DOI:10.1103/PhysRevLett.98.115503 21
- [57] F. Cordero, *Hopping and clustering of oxygen vacancies in SrTiO₃ by anelastic relaxation*. *Phys. Rev. B* **76**, 172106 (2007). DOI:10.1103/PhysRevB.76.172106 21
- [58] C. L. Jia, M. Lentzen, and K. Urban, *Atomic-Resolution Imaging of Oxygen in Perovskite Ceramics*. *Science* **299**, 870 (2003). DOI:10.1126/science.1079121 21
- [59] L. Jin, X. Guo, and C. Jia, *TEM study of <110>-type 35.26° dislocations specially induced by polishing of SrTiO₃ single crystals*. *Ultramicroscopy* **134**, 77 (2013). DOI:10.1016/j.ultramic.2013.06.009 21, 25
- [60] K. Szot, C. Rodenbücher, G. Bihlmayer, W. Speier, R. Ishikawa, N. Shibata, and Y. Ikuhara, *Influence of Dislocations in Transition Metal Oxides on Selected Physical and Chemical Properties*. *Crystals* **8**, 241 (2018). DOI:10.3390/cryst8060241 22, 23, 25, 27
- [61] Alexandrov, V. E., Kotomin, E. A., Maier, J., and Evarestov, R. A., *First-principles study of bulk and surface oxygen vacancies in SrTiO₃ crystal*. *Eur. Phys. J. B* **72**, 53 (2009). DOI:10.1140/epjb/e2009-00339-4 22
- [62] S. P. Waldow and R. A. De Souza, *Computational Study of Oxygen Diffusion along a[100] Dislocations in the Perovskite Oxide SrTiO₃*. *ACS Applied Materials & Interfaces* **8**, 12246 (2016). DOI:10.1021/acsami.5b12574 24
- [63] S. Just, M. Blab, S. Korte, V. Cherepanov, H. Soltner, and B. Voigtländer, *Surface and Step Conductivities on Si(111) Surfaces*. *Phys. Rev. Lett.* **115**, 066801 (2015). DOI:10.1103/PhysRevLett.115.066801 24
- [64] R. Wang, Y. Zhu, and S. M. Shapiro, *Structural Defects and the Origin of the Second Length Scale in SrTiO₃*. *Phys. Rev. Lett.* **80**, 2370 (1998). DOI:10.1103/PhysRevLett.80.2370 24, 25
- [65] P. Hofmann and J. W. Wells, *Surface-sensitive conductance measurements*. *Journal of Physics: Condensed Matter* **21**, 013003 (2009). DOI:10.1088/0953-8984/21/1/013003 25

- [66] K. Szot, G. Bihlmayer, and W. Speier, in: *Nature of the Resistive Switching Phenomena in TiO_2 and $SrTiO_3$: Origin of the Reversible Insulator-Metal Transition*, volume 65 of *Solid State Physics*, chapter 5, 353 – 559 (Academic Press, 2014), DOI: [10.1016/B978-0-12-800175-2.00004-2](https://doi.org/10.1016/B978-0-12-800175-2.00004-2) 27
- [67] A. Leis, C. Rodenbücher, K. Szot, V. Cherepanov, F. Tautz, and B. Voigtländer, *In-situ four-tip STM investigation of the transition from 2D to 3D charge transport in $SrTiO_3$* . *Sci. Rep.* **9**, 2476 (2019). DOI:[10.1038/s41598-019-38888-x](https://doi.org/10.1038/s41598-019-38888-x) 28
- [68] M. Blab, *Ladungstransportmessungen an $Si(111)$ Oberflächen mit einem Multispitzen-Rastertunnelmikroskop*, Ph.D. thesis, Zentralbibliothek Verlag, RWTH Aachen University, Forschungszentrum Jülich GmbH (2014) 34
- [69] D. J. Thouless, M. Kohmoto, M. P. Nightingale, and M. den Nijs, *Quantized Hall Conductance in a Two-Dimensional Periodic Potential*. *Phys. Rev. Lett.* **49**, 405 (1982). DOI:[10.1103/PhysRevLett.49.405](https://doi.org/10.1103/PhysRevLett.49.405) 42
- [70] M. V. Berry, *Quantal Phase Factors Accompanying Adiabatic Changes*. *Proceedings of the Royal Society of London. Series A, Mathematical and Physical Sciences* **392**, 45 (1984). DOI:[10.1098/rspa.1984.0023](https://doi.org/10.1098/rspa.1984.0023) 42
- [71] J. Zak, *Berry's phase for energy bands in solids*. *Phys. Rev. Lett.* **62**, 2747 (1989). DOI: [10.1103/PhysRevLett.62.2747](https://doi.org/10.1103/PhysRevLett.62.2747)
- [72] R. Resta, *Manifestations of Berry's phase in molecules and condensed matter*. *Journal of Physics: Condensed Matter* **12**, R107 (2000). DOI:[10.1088/0953-8984/12/9/201](https://doi.org/10.1088/0953-8984/12/9/201) 42
- [73] C. Wu, B. A. Bernevig, and S.-C. Zhang, *Helical Liquid and the Edge of Quantum Spin Hall Systems*. *Phys. Rev. Lett.* **96**, 106401 (2006). DOI:[10.1103/PhysRevLett.96.106401](https://doi.org/10.1103/PhysRevLett.96.106401) 43
- [74] Q. Niu, D. J. Thouless, and Y.-S. Wu, *Quantized Hall conductance as a topological invariant*. *Phys. Rev. B* **31**, 3372 (1985). DOI:[10.1103/PhysRevB.31.3372](https://doi.org/10.1103/PhysRevB.31.3372) 43
- [75] M. Z. Hasan and C. L. Kane, *Colloquium: Topological insulators*. *Rev. Mod. Phys.* **82**, 3045 (2010). DOI:[10.1103/RevModPhys.82.3045](https://doi.org/10.1103/RevModPhys.82.3045) 43, 44, 45
- [76] L. Fu and C. L. Kane, *Time reversal polarization and a Z_2 adiabatic spin pump*. *Phys. Rev. B* **74**, 195312 (2006). DOI:[10.1103/PhysRevB.74.195312](https://doi.org/10.1103/PhysRevB.74.195312) 43
- [77] L. Fu and C. L. Kane, *Topological insulators with inversion symmetry*. *Phys. Rev. B* **76**, 045302 (2007). DOI:[10.1103/PhysRevB.76.045302](https://doi.org/10.1103/PhysRevB.76.045302) 44, 45
- [78] C. L. Kane and E. J. Mele, *Quantum Spin Hall Effect in Graphene*. *Phys. Rev. Lett.* **95**, 226801 (2005). DOI:[10.1103/PhysRevLett.95.226801](https://doi.org/10.1103/PhysRevLett.95.226801) 44, 45

- [79] L. Fu, C. L. Kane, and E. J. Mele, *Topological Insulators in Three Dimensions*. *Phys. Rev. Lett.* **98**, 106803 (2007). DOI:10.1103/PhysRevLett.98.106803 44
- [80] J. E. Moore and L. Balents, *Topological invariants of time-reversal-invariant band structures*. *Phys. Rev. B* **75**, 121306 (2007). DOI:10.1103/PhysRevB.75.121306
- [81] R. Roy, *Topological phases and the quantum spin Hall effect in three dimensions*. *Phys. Rev. B* **79**, 195322 (2009). DOI:10.1103/PhysRevB.79.195322 44
- [82] D. Hsieh, D. Qiann, L. Wray, Y. Xia, Y. Hor, R. Cava, and M. Hasan, *A topological Dirac insulator in a quantum spin Hall phase*. *Nature* **452**, 970 (2008). DOI:10.1038/nature06843 45
- [83] D. Hsieh, Y. Xia, L. Wray, D. Qian, A. Pal, J. H. Dil, J. Osterwalder, F. Meier, G. Bihlmayer, C. L. Kane, Y. S. Hor, R. J. Cava, and M. Z. Hasan, *Observation of Unconventional Quantum Spin Textures in Topological Insulators*. *Science* **323**, 919 (2009). DOI:10.1126/science.1167733 45
- [84] H. Zhang, C.-X. Liu, X.-L. Qi, X. Dai, Z. Fang, and S.-C. Zhang, *Topological insulators in Bi_2Se_3 , Bi_2Te_3 and Sb_2Te_3 with a single Dirac cone on the surface*. *Nat. Phys.* **5**, 438 (2009). DOI:10.1038/nphys1270 45, 46, 48, 60, 82
- [85] Y. L. Chen, J. G. Analytis, J.-H. Chu, Z. K. Liu, S.-K. Mo, X. L. Qi, H. J. Zhang, D. H. Lu, X. Dai, Z. Fang, S. C. Zhang, I. R. Fisher, Z. Hussain, and Z.-X. Shen, *Experimental Realization of a Three-Dimensional Topological Insulator, Bi_2Te_3* . *Science* **325**, 178 (2009). DOI:10.1126/science.1173034 45, 48
- [86] D. Hsieh, Y. Xia, D. Qian, L. Wray, F. Meier, J. H. Dil, J. Osterwalder, L. Patthey, A. V. Fedorov, H. Lin, A. Bansil, D. Grauer, Y. S. Hor, R. J. Cava, and M. Z. Hasan, *Observation of Time-Reversal-Protected Single-Dirac-Cone Topological-Insulator States in Bi_2Te_3 and Sb_2Te_3* . *Phys. Rev. Lett.* **103**, 146401 (2009). DOI:10.1103/PhysRevLett.103.146401 45, 48
- [87] R. Winkler, *Spin-Orbit Coupling Effects in Two-Dimensional Electron and Hole Systems* (Springer, Berlin, Heidelberg, 2003). ISBN 978-3-540-01187-3 46
- [88] Y. Ando, *Topological Insulator Materials*. *Journal of the Physical Society of Japan* **82**, 102001 (2013). DOI:10.7566/JPSJ.82.102001 46, 48
- [89] S.-Q. Shen, *Topological Insulators* (Springer, Berlin, Heidelberg, 2017). ISBN 978-3-642-32857-2 46, 82
- [90] T. Zhang, P. Cheng, X. Chen, J.-F. Jia, X. Ma, K. He, L. Wang, H. Zhang, X. Dai, Z. Fang, X. Xie, and Q.-K. Xue, *Experimental Demonstration of Topological Surface*

- States Protected by Time-Reversal Symmetry*. *Phys. Rev. Lett.* **103**, 266803 (2009). DOI: 10.1103/PhysRevLett.103.266803 48
- [91] P. Roushan, J. Seo, C. Parker, Y. Hor, D. Hsieh, D. Qian, A. Richardella, M. Hasan, R. Cava, and A. Yazdani, *Topological surface states protected from backscattering by chiral spin texture*. *Nature* **460**, 1106 (2009). DOI:10.1038/nature08308 48
- [92] Y. Jiang, Y. Wang, M. Chen, Z. Li, C. Song, K. He, L. Wang, X. Chen, X. Ma, and Q.-K. Xue, *Landau Quantization and the Thickness Limit of Topological Insulator Thin Films of Sb_2Te_3* . *Phys. Rev. Lett.* **108**, 016401 (2012). DOI:10.1103/PhysRevLett.108.016401 48, 50, 91, 101, 107, 113
- [93] J. Zhang, C.-Z. Chang, Z. Zhang, J. Wen, X. Feng, K. Li, M. Liu, K. He, L. Wang, X. Chen, Q.-K. Xue, X. Ma, and Y. Wang, *Band structure engineering in $(Bi_{1-x}Sb_x)_2Te_3$ ternary topological insulators*. *Nature Communications* **2**, 574 (2011). DOI:10.1038/ncomms1588 48, 50, 63
- [94] D. Kong, Y. Chen, J. J. Cha, Q. Zhang, J. G. Analytis, K. Lai, Z. Liu, S. Sae Hong, K. Koski, S.-K. Mo, Z. Hussain, I. R. Fisher, Z.-X. Shen, and Y. Cui, *Ambipolar field effect in the ternary topological insulator $(Bi_xSb_{1-x})_2Te_3$ by composition tuning*. *Nature Nanotechnology* **6**, 705 (2011). DOI:10.1038/nnano.2011.172
- [95] X. He, T. Guan, X. Wang, B. Feng, P. Cheng, L. Chen, Y. Li, and K. Wu, *Highly tunable electron transport in epitaxial topological insulator $(Bi_{1-x}Sb_x)_2Te_3$ thin films*. *Applied Physics Letters* **101**, 123111 (2012). DOI:10.1063/1.4754108
- [96] S. Shimizu, R. Yoshimi, T. Hatano, K. S. Takahashi, A. Tsukazaki, M. Kawasaki, Y. Iwasa, and Y. Tokura, *Gate control of surface transport in MBE-grown topological insulator $(Bi_{1-x}Sb_x)_2Te_3$ thin films*. *Phys. Rev. B* **86**, 045319 (2012). DOI:10.1103/PhysRevB.86.045319
- [97] C. Weyrich, M. Drögeler, J. Kampmeier, M. Eschbach, G. Mussler, T. Merzenich, T. Stolica, I. E. Batov, J. Schubert, L. Plucinski, B. Beschoten, C. M. Schneider, C. Stampfer, D. Grützmacher, and T. Schäpers, *Growth, characterization, and transport properties of ternary $(Bi_{1-x}Sb_x)_2Te_3$ topological insulator layers*. *J. Phys.: Condens. Matter* **28**, 495501 (2016). DOI:10.1088/0953-8984/28/49/495501 48, 51, 88
- [98] M. Lanius, J. Kampmeier, S. Kölling, G. Mussler, P. Koenraad, and D. Grützmacher, *Topography and structure of ultrathin topological insulator Sb_2Te_3 films on $Si(111)$ grown by means of molecular beam epitaxy*. *Journal of Crystal Growth* **453**, 158 (2016). DOI:10.1016/j.jcrysgro.2016.08.016 49, 85, 86

- [99] F. Lüpke, S. Just, G. Bihlmayer, M. Lanius, M. Luysberg, J. Dolezal, E. Neumann, V. Cherepanov, I. Ostadal, G. Mussler, D. Grützmacher, and B. Voigtländer, *Chalcogenide-based van der Waals epitaxy: Interface conductivity of tellurium on Si(111)*. *Phys. Rev. B* **96**, 035301 (2017). DOI:10.1103/PhysRevB.96.035301 49
- [100] J. Kellner, M. Eschbach, J. Kampmeier, M. Lanius, E. Mlynczak, G. Mussler, B. Holländer, L. Plucinski, M. Liebmann, D. Grützmacher, C. M. Schneider, and M. Morgenstern, *Tuning the Dirac point to the Fermi level in the ternary topological insulator $(\text{Bi}_{1-x}\text{Sb}_x)_2\text{Te}_3$* . *Applied Physics Letters* **107**, 251603 (2015). DOI:10.1063/1.4938394 49, 50, 62, 72, 75, 88, 92, 102
- [101] F. Lüpke, J. Sven, M. Eschbach, T. Heider, E. Mlynczak, M. Lanius, P. Schüffelgen, D. Rosenbach, N. v d Driesch, V. Cherepanov, G. Mussler, L. Plucinski, D. Grützmacher, C. M. Schneider, F. S. Tautz, and B. Voigtländer, *In situ disentangling surface state transport channels of a topological insulator thin film by gating*. *npj Quantum Materials* **3**, 46 (2018). DOI:10.1038/s41535-018-0116-1 50, 51, 62, 63, 72, 75, 76, 88, 92, 93, 102
- [102] D. Pesin and A. Macdonald, *Spintronics and Pseudospintronics in Graphene and Topological Insulators*. *Nature Materials* **11**, 409 (2012). DOI:10.1038/nmat3305 53
- [103] S. M. Hus, X.-G. Zhang, G. D. Nguyen, W. Ko, A. P. Baddorf, Y. P. Chen, and A.-P. Li, *Detection of the Spin-Chemical Potential in Topological Insulators Using Spin-Polarized Four-Probe STM*. *Phys. Rev. Lett.* **119**, 137202 (2017). DOI:10.1103/PhysRevLett.119.137202 53, 60, 67, 75, 76
- [104] W. Ko, G. D. Nguyen, H. Kim, J. S. Kim, X.-G. Zhang, and A.-P. Li, *Accessing the Intrinsic Spin Transport in a Topological Insulator by Controlling the Crossover of Bulk-to-Surface Conductance*. *Phys. Rev. Lett.* **121**, 176801 (2018). DOI:10.1103/PhysRevLett.121.176801 53, 60, 63, 67, 75
- [105] J. P. Ibe, P. P. Bey, S. L. Brandow, R. A. Brizzolara, N. A. Burnham, D. P. DiLella, K. P. Lee, C. R. K. Marrian, and R. J. Colton, *On the electrochemical etching of tips for scanning tunneling microscopy*. *Journal of Vacuum Science & Technology A* **8**, 3570 (1990). DOI:10.1116/1.576509 54, 55, 56
- [106] M. Cavallini and F. Biscarini, *Electrochemically etched nickel tips for spin polarized scanning tunneling microscopy*. *Review of Scientific Instruments* **71**, 4457 (2000). DOI: 10.1063/1.1311936 54
- [107] C. Albonetti, M. Cavallini, M. Massi, J. F. Moulin, and F. Biscarini, *Electrochemical fabrication of cobalt and nickel tips for scanning tunneling microscopy*. *Journal of Vacuum Science & Technology B: Microelectronics and Nanometer Structures Processing, Measurement, and Phenomena* **23**, 2564 (2005). DOI:10.1116/1.2131873 54

- [108] D. Hsieh, Y. Xia, D. Qian, L. Wray, H. Dil, F. Meier, J. Osterwalder, L. Patthey, J. G Checkelsky, N. P Ong, A. Fedorov, H.-H. Lin, A. Bansil, D. Grauer, Y. Hor, R. J Cava, and M. Z. Hasan, *A tunable topological insulator in the spin helical Dirac transport regime*. *Nature* **460**, 1101 (2009). DOI:10.1038/nature08234 60
- [109] Z.-H. Pan, E. Vescovo, A. V. Fedorov, D. Gardner, Y. S. Lee, S. Chu, G. D. Gu, and T. Valla, *Electronic Structure of the Topological Insulator Bi_2Se_3 Using Angle-Resolved Photoemission Spectroscopy: Evidence for a Nearly Full Surface Spin Polarization*. *Phys. Rev. Lett.* **106**, 257004 (2011). DOI:10.1103/PhysRevLett.106.257004
- [110] C. Jozwiak, Y. L. Chen, A. V. Fedorov, J. G. Analytis, C. R. Rotundu, A. K. Schmid, J. D. Denlinger, Y.-D. Chuang, D.-H. Lee, I. R. Fisher, R. J. Birgeneau, Z.-X. Shen, Z. Hussain, and A. Lanzara, *Widespread spin polarization effects in photoemission from topological insulators*. *Phys. Rev. B* **84**, 165113 (2011). DOI:10.1103/PhysRevB.84.165113 60
- [111] C. H Li, O. van 't Erve, J. Robinson, Y. Liu, L. Li, and B. Jonker, *Electrical detection of charge-current-induced spin polarization due to spin-momentum locking in Bi_2Se_3* . *Nature Nanotechnology* **9**, 218 (2014). DOI:10.1038/nnano.2014.16 60
- [112] A. Dankert, J. Geurs, M. V. Kamalakar, S. Charpentier, and S. P. Dash, *Room Temperature Electrical Detection of Spin Polarized Currents in Topological Insulators*. *Nano Letters* **15**, 7976 (2015). DOI:10.1021/acs.nanolett.5b03080 75
- [113] Y. Ando, T. Hamasaki, T. Kurokawa, K. Ichiba, F. Yang, M. Novak, S. Sasaki, K. Segawa, Y. Ando, and M. Shiraishi, *Electrical Detection of the Spin Polarization Due to Charge Flow in the Surface State of the Topological Insulator $\text{Bi}_{1.5}\text{Sb}_{0.5}\text{Te}_{1.7}\text{Se}_{1.3}$* . *Nano Letters* **14**, 6226 (2014). DOI:10.1021/nl502546c
- [114] J. Tian, I. Miotkowski, S. Hong, and Y. Chen, *Electrical injection and detection of spin-polarized currents in topological insulator $\text{Bi}_2\text{Te}_2\text{Se}$* . *Scientific Reports* **5**, 14293 (2015). DOI:10.1038/srep14293 75
- [115] L. Liu, A. Richardella, I. Garate, Y. Zhu, N. Samarth, and C.-T. Chen, *Spin-polarized tunneling study of spin-momentum locking in topological insulators*. *Phys. Rev. B* **91**, 235437 (2015). DOI:10.1103/PhysRevB.91.235437
- [116] J. S. Lee, A. Richardella, D. R. Hickey, K. A. Mkhoyan, and N. Samarth, *Mapping the chemical potential dependence of current-induced spin polarization in a topological insulator*. *Phys. Rev. B* **92**, 155312 (2015). DOI:10.1103/PhysRevB.92.155312 75
- [117] J. Tang, L.-T. Chang, X. Kou, K. Murata, E. S. Choi, M. Lang, Y. Fan, Y. Jiang, M. Montazeri, W. Jiang, Y. Wang, L. He, and K. L. Wang, *Electrical Detection of Spin-Polarized Surface States Conduction in $(\text{Bi}_{0.53}\text{Sb}_{0.47})_2\text{Te}_3$ Topological Insulator*. *Nano Letters* **14**, 5423 (2014). DOI:10.1021/nl5026198 60

- [118] S. Just, F. Lüpke, V. Cherepanov, F. S. Tautz, and B. Voigtländer, *Parasitic conduction channels in topological insulator thin films*. *Phys. Rev. B* **101**, 245413 (2020) 61, 75, 76
- [119] D. Kim, S. Cho, N. Butch, P. Syers, K. Kirshenbaum, S. Adam, J. Paglione, and M. Fuhrer, *Surface conduction of topological Dirac electrons in bulk insulating Bi_2Se_3* . *Nature Physics* **8**, 459 (2011). DOI:10.1038/nphys2286 63
- [120] M. Johnson and R. H. Silsbee, *Electron spin injection and detection at a ferromagnetic-paramagnetic interface*. *Journal of Applied Physics* **63**, 3934 (1988). DOI:10.1063/1.340611 63
- [121] M. Johnson and R. H. Silsbee, *Coupling of electronic charge and spin at a ferromagnetic-paramagnetic metal interface*. *Phys. Rev. B* **37**, 5312 (1988). DOI:10.1103/PhysRevB.37.5312 63
- [122] S. Hong, V. Diep, S. Datta, and Y. P. Chen, *Modeling potentiometric measurements in topological insulators including parallel channels*. *Phys. Rev. B* **86**, 085131 (2012). DOI:10.1103/PhysRevB.86.085131 63, 75, 76
- [123] F. Yang, S. Ghatak, A. A. Taskin, K. Segawa, Y. Ando, M. Shiraishi, Y. Kanai, K. Matsumoto, A. Rosch, and Y. Ando, *Switching of charge-current-induced spin polarization in the topological insulator BiSbTeSe_2* . *Phys. Rev. B* **94**, 075304 (2016). DOI:10.1103/PhysRevB.94.075304 63, 75, 76
- [124] P. Li and I. Appelbaum, *Interpreting current-induced spin polarization in topological insulator surface states*. *Phys. Rev. B* **93**, 220404 (2016). DOI:10.1103/PhysRevB.93.220404 65, 67, 75
- [125] S. F. Alvarado, *Tunneling Potential Barrier Dependence of Electron Spin Polarization*. *Phys. Rev. Lett.* **75**, 513 (1995). DOI:10.1103/PhysRevLett.75.513 75
- [126] R. J. Soulen, J. M. Byers, M. S. Osofsky, B. Nadgorny, T. Ambrose, S. F. Cheng, P. R. Broussard, C. T. Tanaka, J. Nowak, J. S. Moodera, A. Barry, and J. M. D. Coey, *Measuring the Spin Polarization of a Metal with a Superconducting Point Contact*. *Science* **282**, 85 (1998). DOI:10.1126/science.282.5386.85
- [127] T. H. Kim and J. S. Moodera, *Large spin polarization in epitaxial and polycrystalline Ni films*. *Phys. Rev. B* **69**, 020403 (2004). DOI:10.1103/PhysRevB.69.020403 75
- [128] A. Dankert, P. Bhaskar, D. Khokhriakov, I. H. Rodrigues, B. Karpiak, M. V. Kamalakar, S. Charpentier, I. Garate, and S. P. Dash, *Origin and evolution of surface spin current in topological insulators*. *Phys. Rev. B* **97**, 125414 (2018). DOI:10.1103/PhysRevB.97.125414 75

- [129] O. V. Yazyev, J. E. Moore, and S. G. Louie, *Spin Polarization and Transport of Surface States in the Topological Insulators Bi_2Se_3 and Bi_2Te_3 from First Principles*. *Phys. Rev. Lett.* **105**, 266806 (2010). DOI:10.1103/PhysRevLett.105.266806 75
- [130] E. K. de Vries, A. M. Kamerbeek, N. Koirala, M. Brahlek, M. Salehi, S. Oh, B. J. van Wees, and T. Banerjee, *Towards the understanding of the origin of charge-current-induced spin voltage signals in the topological insulator Bi_2Se_3* . *Phys. Rev. B* **92**, 201102 (2015). DOI:10.1103/PhysRevB.92.201102 75
- [131] P. D. C. King, R. C. Hatch, M. Bianchi, R. Ovsyannikov, C. Lupulescu, G. Landolt, B. Slomski, J. H. Dil, D. Guan, J. L. Mi, E. D. L. Rienks, J. Fink, A. Lindblad, S. Svensson, S. Bao, G. Balakrishnan, B. B. Iversen, J. Osterwalder, W. Eberhardt, F. Baumberger, and P. Hofmann, *Large Tunable Rashba Spin Splitting of a Two-Dimensional Electron Gas in Bi_2Se_3* . *Phys. Rev. Lett.* **107**, 096802 (2011). DOI:10.1103/PhysRevLett.107.096802 76
- [132] M. Buehler and G. Pearson, *Magnetoconductive correction factors for an isotropic Hall plate with point sources*. *Solid-State Electronics* **9**, 395 (1966). DOI:10.1016/0038-1101(66)90154-7 76
- [133] M. Buehler, *A hall four-point probe on thin plates: Theory and experiment*. *Solid-State Electronics* **10**, 801 (1967). DOI:10.1016/0038-1101(67)90163-3 76
- [134] A. Leis, M. Schleenvoigt, A. Jalil, V. Cherepanov, G. Mussler, D. Grützmacher, F. Tautz, and B. Voigtländer, *Room temperature in-situ measurement of the spin voltage of a BiSbTe_3 thin film*. *Sci. Rep.* **10**, 2816 (2020). DOI:10.1038/s41598-020-59679-9 79
- [135] C.-Z. Chang, J. Zhang, X. Feng, J. Shen, Z. Zhang, M. Guo, K. Li, Y. Ou, P. Wei, L.-L. Wang, Z.-Q. Ji, Y. Feng, S. Ji, X. Chen, J. Jia, X. Dai, Z. Fang, S.-C. Zhang, K. He, Y. Wang, L. Lu, X.-C. Ma, and Q.-K. Xue, *Experimental Observation of the Quantum Anomalous Hall Effect in a Magnetic Topological Insulator*. *Science* **340**, 167 (2013). DOI:10.1126/science.1234414 82
- [136] X. Kou, S.-T. Guo, Y. Fan, L. Pan, M. Lang, Y. Jiang, Q. Shao, T. Nie, K. Murata, J. Tang, Y. Wang, L. He, T.-K. Lee, W.-L. Lee, and K. L. Wang, *Scale-Invariant Quantum Anomalous Hall Effect in Magnetic Topological Insulators beyond the Two-Dimensional Limit*. *Phys. Rev. Lett.* **113**, 137201 (2014). DOI:10.1103/PhysRevLett.113.137201
- [137] C.-Z. Chang, W. Zhao, D. Y. Kim, H. Zhang, B. A. Assaf, D. Heiman, S.-C. Zhang, C. Liu, M. H. W. Chan, and J. S. Moodera, *High-precision realization of robust quantum anomalous Hall state in a hard ferromagnetic topological insulator*. *Nat. Mater.* **14**, 473 (2015). DOI:10.1038/nmat4204

- [138] Y. Deng, Y. Yu, M. Z. Shi, Z. Guo, Z. Xu, J. Wang, X. H. Chen, and Y. Zhang, *Quantum anomalous Hall effect in intrinsic magnetic topological insulator $MnBi_2Te_4$* . *Science* **367**, 895 (2020). DOI:10.1126/science.aax8156
- [139] C. Liu, Y. Wang, H. Li, Y. Li, J. Li, K. He, Y. Xu, J. Zhang, and Y. Wang, *Robust axion insulator and Chern insulator phases in a two-dimensional antiferromagnetic topological insulator*. *Nat. Mater.* **19**, 522 (2020). DOI:10.1038/s41563-019-0573-3 82
- [140] H.-Z. Lu, W.-Y. Shan, W. Yao, Q. Niu, and S.-Q. Shen, *Massive Dirac fermions and spin physics in an ultrathin film of topological insulator*. *Phys. Rev. B* **81**, 115407 (2010). DOI:10.1103/PhysRevB.81.115407 82, 83, 91, 92, 100
- [141] C.-X. Liu, H. Zhang, B. Yan, X.-L. Qi, T. Frauenheim, X. Dai, Z. Fang, and S.-C. Zhang, *Oscillatory crossover from two-dimensional to three-dimensional topological insulators*. *Phys. Rev. B* **81**, 041307 (2010). DOI:10.1103/PhysRevB.81.041307 82, 100
- [142] T. Förster, P. Krüger, and M. Rohlfing, *Two-dimensional topological phases and electronic spectrum of Bi_2Se_3 thin films from GW calculations*. *Phys. Rev. B* **92**, 201404 (2015). DOI:10.1103/PhysRevB.92.201404 100
- [143] T. Förster, P. Krüger, and M. Rohlfing, *GW calculations for Bi_2Te_3 and Sb_2Te_3 thin films: Electronic and topological properties*. *Phys. Rev. B* **93**, 205442 (2016). DOI:10.1103/PhysRevB.93.205442 82, 91, 100, 107, 113
- [144] W.-Y. Shan, H.-Z. Lu, and S.-Q. Shen, *Effective continuous model for surface states and thin films of three-dimensional topological insulators*. *New Journal of Physics* **12**, 043048 (2010). DOI:10.1088/1367-2630/12/4/043048 83, 100
- [145] M. Lanius, *Topological Insulating Tellurides : How to tune Doping, Topology, and Dimensionality*, Ph.D. thesis, Zentralbibliothek Verlag, RWTH Aachen University, Forschungszentrum Jülich GmbH (2018) 85, 86
- [146] S. Borisova, J. Kampmeier, M. Luysberg, G. Mussler, and D. Grützmacher, *Domain formation due to surface steps in topological insulator Bi_2Te_3 thin films grown on Si (111) by molecular beam epitaxy*. *Applied Physics Letters* **103**, 081902 (2013). DOI: 10.1063/1.4818456 85, 86
- [147] B. Skinner, T. Chen, and B. I. Shklovskii, *Effects of bulk charged impurities on the bulk and surface transport in three-dimensional topological insulators*. *J. Exp. Theor. Phys.* **117**, 579 (2013). DOI:10.1134/S1063776113110150 92
- [148] V. Ariel and A. Natan, *Electron Effective Mass in Graphene*, <https://arxiv.org/abs/1206.6100> (2012) . 93

- [149] M. Büttiker, *Four-Terminal Phase-Coherent Conductance*. *Phys. Rev. Lett.* **57**, 1761 (1986). DOI:10.1103/PhysRevLett.57.1761 100
- [150] M. Büttiker, *Absence of backscattering in the quantum Hall effect in multiprobe conductors*. *Phys. Rev. B* **38**, 9375 (1988). DOI:10.1103/PhysRevB.38.9375 100
- [151] S. Datta, *Electronic Transport in Mesoscopic Systems*, Cambridge Studies in Semiconductor Physics and Microelectronic Engineering (Cambridge University Press, 1995) 101
- [152] Y. Zhang, K. He, C.-Z. Chang, C.-L. Song, L.-L. Wang, X. Chen, J.-F. Jia, Z. Fang, X. Dai, W.-Y. Shan, S.-Q. Shen, Q. Niu, X.-L. Qi, S.-C. Zhang, X.-C. Ma, and Q.-K. Xue, *Crossover of the three-dimensional topological insulator Bi₂Se₃ to the two-dimensional limit*. *Nat. Phys.* **6**, 584 (2010). DOI:10.1038/nphys1689 101
- [153] T. Zhang, J. Ha, N. Levy, Y. Kuk, and J. Stroschio, *Electric-Field Tuning of the Surface Band Structure of Topological Insulator Sb₂Te₃ Thin Films*. *Phys. Rev. Lett.* **111**, 056803 (2013). DOI:10.1103/PhysRevLett.111.056803 101
- [154] S. Wu, V. Fatemi, Q. D. Gibson, K. Watanabe, T. Taniguchi, R. J. Cava, and P. Jarillo-Herrero, *Observation of the quantum spin hall effect up to 100 kelvin in a monolayer crystal*. *Science* **359**, 76 (2018). DOI:10.1126/science.aan6003 102
- [155] B. Voigtländer, *Scanning Probe Microscopy: Atomic Force Microscopy and Scanning Tunneling Microscopy* (Springer, New York, Berlin, Heidelberg, 2015). ISBN 978-3-662-45240-0 102
- [156] C. Pauly, B. Rasche, K. Koepf, M. Liebmann, M. Pratzner, M. Richter, J. Kellner, M. Eschbach, B. Kaufmann, L. Plucinski, C. M. Schneider, M. Ruck, J. van den Brink, and M. Morgenstern, *Subnanometre-wide electron channels protected by topology*. *Nature Physics* **11**, 338 (2015). DOI:10.1038/nphys3264 104
- [157] F. Reis, G. Li, L. Dudy, M. Bauernfeind, S. Glass, W. Hanke, R. Thomale, J. Schäfer, and R. Claessen, *Bismuthene on a SiC substrate: A candidate for a high-temperature quantum spin Hall material*. *Science* **357**, 287 (2017). DOI:10.1126/science.aai8142
- [158] F. Lüpke, D. Waters, A. D. Pham, J. Yan, D. G. Mandrus, P. Ganesh, and B. M. Hunt, *Quantum spin Hall edge states in twisted-bilayer 1T'-WTe₂*, <https://arxiv.org/abs/2010.13699> (2020) . 104
- [159] J. Baringhaus, M. Ruan, F. Edler, A. Tejeda, M. Sicot, A. Taleb-Ibrahimi, A.-P. Li, Z. Jiang, E. H. Conrad, C. Berger, C. Tegenkamp, and W. A. de Heer, *Exceptional ballistic transport in epitaxial graphene nanoribbons*. *Nature* **506**, 349 (2014). DOI:10.1038/nature12952 106

- [160] J. Aprojanz, I. Miccoli, J. Baringhaus, and C. Tegenkamp, *1D ballistic transport channel probed by invasive and non-invasive contacts*. *Applied Physics Letters* **113**, 191602 (2018). DOI:10.1063/1.5054393
- [161] J. Aprojanz, S. R. Power, P. Bampoulis, S. Roche, A.-P. Jauho, H. J. W. Zandvliet, A. A. Zakharov, and C. Tegenkamp, *Ballistic tracks in graphene nanoribbons*. *Nature Communications* **9**, 4426 (2018). DOI:10.1038/s41467-018-06940-5 106
- [162] R. de Picciotto, H. L. Stormer, L. N. Pfeiffer, K. W. Baldwin, and K. W. West, *Four-terminal resistance of a ballistic quantum wire*. *Nature* **411**, 51 (2001). DOI:10.1038/35075009 107

Publications

Publications that result from individual parts of this work are listed below.

- [A. Leis](#), C. Rodenbücher, K. Szot, V. Cherepanov, F. S. Tautz and B. Voigtländer, *In-situ four-tip STM investigation of the transition from 2D to 3D charge transport in SrTiO₃*. Sci. Rep. **9**, 2476 (2019).
- [A. Leis](#), M. Schleenvoigt, A. R. Jalil, V. Cherepanov, G. Mussler, D. Grützmacher, F. S. Tautz, and B. Voigtländer, *Room temperature in-situ measurement of the spin voltage of a BiSbTe₃ thin film*. Sci. Rep. **10**, 2816 (2020).
- [A. Leis](#), M. Schleenvoigt, V. Cherepanov, F. Lüpke, P. Schüffelgen, G. Mussler, D. Grützmacher, B. Voigtländer, and F. S. Tautz, *Lifting the spin-momentum locking in ultra-thin topological insulator films*. Accepted for publication in Adv. Quantum Technol.
- [A. Leis](#), M. Schleenvoigt, H. Soltner, V. Cherepanov, I. Aguilera, F. Lüpke, G. Mussler, D. Grützmacher, B. Voigtländer, and F. S. Tautz, *A method of unequivocally detecting edge states in topological insulator films*. In preparation.
- [A. Leis](#), V. Cherepanov, B. Voigtländer, and F. S. Tautz, *Nanoscale tip positioning based on overlapping scans for four-point measurements with a multi-tip STM*. In preparation.

Acknowledgements

The research presented in this work was performed in the group of Prof. Dr. Bert Voigtländer of the Peter Grünberg Institut (PGI-3) at Forschungszentrum Jülich. In the following, I would like to thank the people who supported me during the time of my work.

First of all, I want to thank Prof. Dr. Bert Voigtländer for his superb supervision and support. Thank you for constantly providing me with new concepts, challenging me on my interpretations of data and for supporting me mentally during my moments of self-doubt. Working in your group not only supplied me with experience and knowledge, even beyond science, but was also always a pleasure.

In addition, I thank Prof. Dr. Markus Morgenstern for being the associate assessor of this PhD work.

Furthermore, I would like to thank Prof. Dr. Stefan Tautz for initially introducing me to the research activities at PGI-3 during my Master studies and for giving me the opportunity to perform my scientific work in the institute.

I thank Dr. Vasily Cherepanov for his indispensable help with occasional repairs of the multi-tip STM, critical scientific input and casual discussions about everyday life.

Additionally, I want to thank Dipl.-Ing. Franz-Peter Coenen and Helmut Stollwerk for assistance with various technical challenges.

Special thanks are dedicated to my other colleagues in the multi-tip STM group. I thank my predecessor Sven Just for giving me a thorough introduction into the working and measurement principle of the instrument. I am also thankful to Dr. Stefan Korte, Dr. Felix Lüpke and David Cuma for their helpful contributions.

Beyond the multi-tip STM group, I would like to thank all colleagues of PGI-3 for contributing to an extraordinarily nice working atmosphere.

I further acknowledge Michael Schleenvoigt and other collaborators from PGI-9 for supplying

Acknowledgements

me with interesting samples to investigate.

Moreover, I want to thank all my close friends for occasionally keeping me distracted in stressful times during my scientific work. In particular, I thank Lisa Kastenholz for being an important part of my life.

Lastly, I also want to thank my family - Andrej Leis, Elena Leis and Christian Leis - for their everlasting and unconditional support in all of my endeavors.

Detailed derivations

A.1. Resistance uncertainty

In section 2.2.3, the measured four-point resistance $R^{4P} = V_{23}/I_{14}$ resulting from an equidistant tip configuration on the surface of a conducting 2D and 3D system was presented as Eq. 2.35 and Eq. 2.37. In case of finite positioning accuracy, the position of each tip is subject to an uncertainty δr , as illustrated by the square areas in Fig. A.1. It is assumed that the actual tip positions are uniformly distributed in a square area around the desired target locations. The uncertainty of positions propagates to an uncertainty of the measured four-point resistance δR . As an accessible approximation, the resulting resistance error is determined from the extremal resistance values in the areas spanned by δr . Within the four square areas, there exists one configuration resulting in a minimum resistance $R^{\min}(s)$ and one configuration which yields a resistance maximum $R^{\max}(s)$.

Intuitively, these configurations can be estimated from symmetry considerations, as sketched in the lower panel of Fig. A.1. The maximum resistance in the uncertainty areas is obtained when the potential drop is as steep as possible, which is achieved when tips 1 and 4 have the smallest possible distance. Simultaneously, the potential difference V_{23} probed by tips 2 and 3 needs to be maximal, i.e. the corresponding tips need to be far apart. The corresponding configuration is indicated by blue dots in Fig. A.1. By inserting the corresponding positions in the general position-dependent resistance expressions Eq. 2.20 and Eq. 2.33, the maximum

as

$$R_{2D}^{\min}(\epsilon) = \frac{1}{2\pi\sigma_{2D}} \left[\ln\left(\frac{2s}{\sqrt{(s+\delta r)^2 + (\delta r)^2}}\right) - \ln\left(\frac{\sqrt{(s+\delta r)^2 + (\delta r)^2}}{2s}\right) \right] \quad (\text{A.5})$$

$$= \frac{1}{2\pi\sigma_{2D}} \ln\left(\frac{4}{(1+\epsilon)^2 + \epsilon^2}\right) \quad (\text{A.6})$$

and

$$R_{3D}^{\min}(\epsilon) = \frac{1}{2\pi\sigma_{3D}} \left[\frac{1}{\sqrt{(s+\delta r)^2 + (\delta r)^2}} - \frac{1}{2s} - \frac{1}{2s} + \frac{1}{\sqrt{(s+\delta r)^2 + (\delta r)^2}} \right] \quad (\text{A.7})$$

$$= \frac{1}{2\pi\sigma_{3D}s} \left[\frac{2}{\sqrt{(1+\epsilon)^2 + \epsilon^2}} - 1 \right] \quad (\text{A.8})$$

for the 2D and the 3D case, respectively.

Using these extremal values, the uncertainty of the four-point resistance δR resulting from misplacement of the tips within δr is estimated as

$$\delta R/R^{4P} = \frac{R^{\max} - R^{\min}}{R^{4P}} \quad (\text{A.9})$$

for both dimensions, which results in

$$\delta R_{2D}/R_{2D}^{4P} = \frac{1}{2\ln(2)} \left[\ln\left(\frac{4}{(1-\epsilon)^2}\right) - \ln\left(\frac{4}{(1+2\epsilon+2\epsilon^2)}\right) \right] \quad (\text{A.10})$$

$$= \frac{1}{2\ln(2)} \ln\left(\frac{1+2\epsilon+2\epsilon^2}{1-2\epsilon+\epsilon^2}\right) \quad (\text{A.11})$$

and

$$\delta R_{3D}/R_{3D}^{4P} = \left[\frac{2}{1-\epsilon} - \frac{2}{\sqrt{1+2\epsilon+2\epsilon^2}} \right], \quad (\text{A.12})$$

which are identical to the expressions presented in Eq. 2.39 and Eq. 2.40.

A.2. Dimensionless tip distance χ

For the presentation of the results of the spin-sensitive resistance measurements in chapter 5, a normalized dimensionless inter-tip distance χ is used to compare the different measurements to each other. For a given configuration of the fixed tip positions s_{12} and s_{14} between each set of measurements, the distance-dependent four-point resistance is determined by

$$R = \frac{1}{2\pi\sigma_{2D}} \left[\ln\left(\frac{s_{24}}{s_{12}}\right) - \ln\left(\frac{s_{24}-D}{s_{12}+D}\right) \right] + R_s, \quad (\text{A.13})$$

where D is the distance between the two voltage-probing tips, which is changed in the experiment. According to this equation, $\frac{dR}{dD}$ depends on s_{12} and s_{14} . This makes extrapolation

of $R(D \rightarrow 0)$ from data points with different s_{12} and s_{14} difficult. Therefore, a dimensionless distance χ instead of D is used such that the slope of the four-point resistance is approximately constant.

$$\frac{dR}{d\chi} = \frac{dR}{dD} \frac{dD}{d\chi} = \frac{1}{2\pi\sigma_{2D}} \left(\frac{s_{12} + D}{s_{24} - D} \right) \frac{(s_{12} + D) + (s_{24} - D)}{(s_{12} + D)^2} \cdot \frac{dD}{d\chi} \quad (\text{A.14})$$

$$= \frac{1}{2\pi\sigma_{2D}} \frac{s_{12} + s_{24}}{(s_{12} + D)(s_{24} - D)} \cdot \frac{dD}{d\chi} \quad (\text{A.15})$$

$$= \frac{1}{2\pi\sigma_{2D}} \frac{s_{12} + s_{24}}{s_{12}s_{24}} \frac{1}{\left(1 + \frac{D}{s_{12}}\right)\left(1 - \frac{D}{s_{24}}\right)} \cdot \frac{dD}{d\chi}. \quad (\text{A.16})$$

By defining $\chi \equiv \frac{s_{12} + s_{24}}{s_{12}s_{24}} D$, it is found that $\frac{dD}{d\chi} = \frac{s_{12}s_{24}}{s_{12} + s_{24}}$ and consequently $\frac{dR}{d\chi} = \frac{1}{2\pi\sigma_{2D}} \frac{1}{\left(1 + \frac{D}{s_{12}}\right)\left(1 - \frac{D}{s_{24}}\right)}$. With the approximation of $s_{12}, s_{24} \gg D$ in the experiment, the resulting slope of the four-point resistance resistance becomes $\frac{dR}{d\chi} = \frac{1}{2\pi\sigma_{2D}}$ and therefore independent of s_{12} and s_{24} .

Additional data

B.1. Four-point measurements on different $(\text{Bi}_{0.16}\text{Sb}_{0.84})_2\text{Te}_3$ terraces

In chapter 6, the conductivity of a $(\text{Bi}_{0.16}\text{Sb}_{0.84})_2\text{Te}_3$ thin film was investigated as a function of film thickness. While four-point measurements were performed on different terraces of thicknesses $1\text{ QL} \leq L \leq 5\text{ QL}$, only one exemplary measurement configuration was shown. In Fig. B.1 and Fig. B.2, other examples of measured terraces and the employed tip configurations that were included in the investigation are presented.

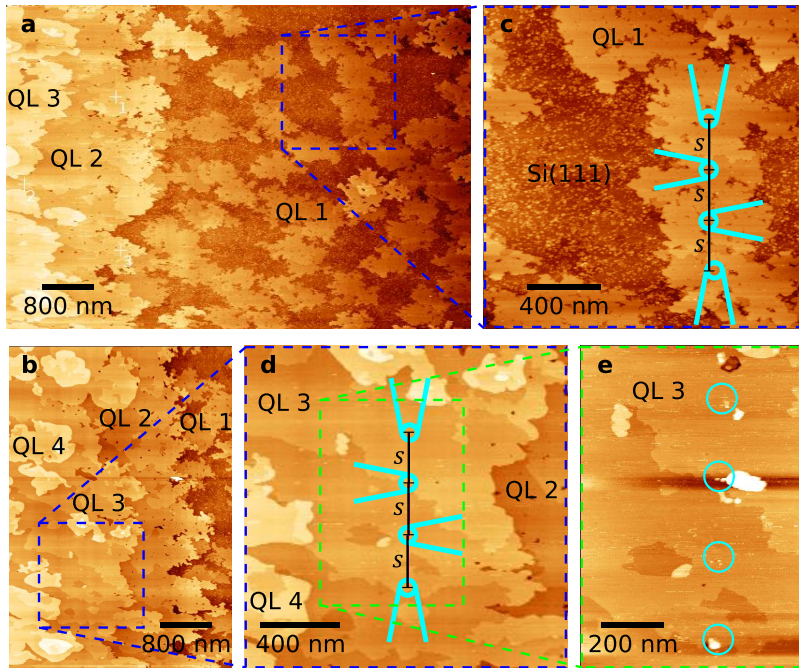


Fig. B.1.: Four-point resistance measurements on a 1QL terrace and a 3QL terrace. (a), (c) Large overview scans of the local topography that serve as maps to identify terraces and to navigate the STM tips. (b), (d) Using small overlapping STM scans, the tips are navigated to the area of interest on the corresponding terrace. As indicated by the cyan symbols, electric measurements are performed in an equidistant configuration with $s \approx 250$ nm. (e) After the measurement procedure, topography scans of the contacted area are performed, revealing minimal damage to the surface.

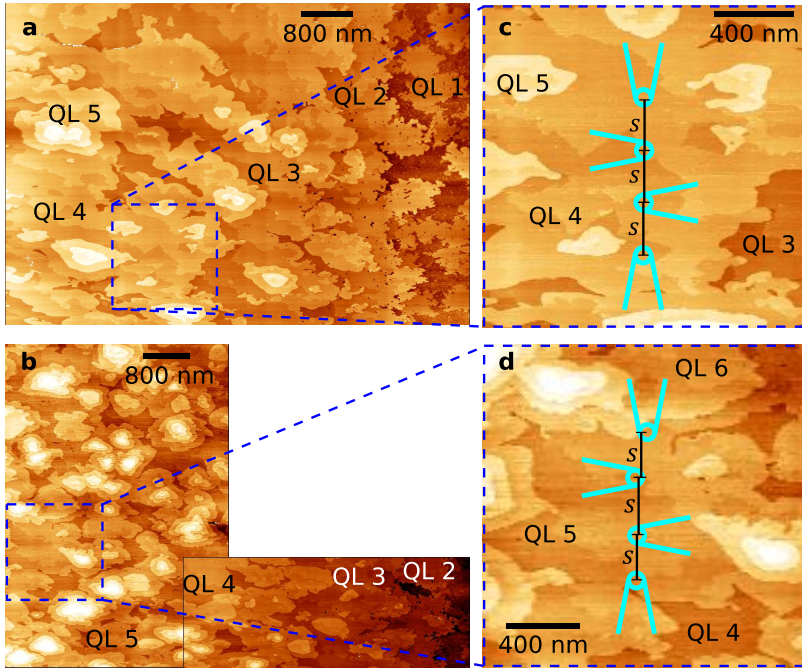


Fig. B.2.: Four-point resistance measurement on a 4QL terrace and a 5QL terrace. (a), (c) Large overview scans of the local topography that serve as maps to identify terraces and to navigate the STM tips. (b), (d) Using small overlapping STM scans, the tips are navigated to the area of interest on the corresponding terrace. As indicated by the cyan symbols, electric measurements are performed in an equidistant configuration with $s \approx 250$ nm.

B.2. Analytic solution for a conductive 1D channel

In section 7.4.1, the influence of a highly conductive 1D channel on the 2D potential distribution that results from adjacent current injection in parallel was investigated qualitatively. To determine the resulting potential analytically, the conductive edge channel was treated as a half-infinite plane with a conductivity σ_2 that is much higher than the conductivity of the terrace background σ_1 , such that the method of mirror images can be applied to solve the problem. The fact that this treatment is indeed valid is shown here by a comparison of the analytic solution to the result obtained by a finite element calculation.

Figure B.3 (a) conceptually shows the geometry that is used as input for the simulation of a highly conductive edge channel and presents the resulting calculated potential distribution. Two half-infinite planes, with conductivities $\sigma_1 \gtrsim \sigma_2$, are modeled separated by a region of infinitesimal width and conductivity $\sigma_{\text{edge}} \gg \sigma_1, \sigma_2$ in between. In Fig. B.3 (b), the geometry of the approximated scenario, as well as the resulting analytic potential distribution are presented. The analytic model entails two mirror current sources with opposite sign across the straight boundary of two regions with $\sigma_2 \gg \sigma_1$. As evident from the correspondence of the two results of the potential distribution, the analytic solution based on two half-infinite planes is a good approximation of the potential landscape resulting from a highly conductive 1D channel. This is intuitive, as for $\sigma_{\text{edge}} \rightarrow \infty$, the width of the 'edge region', as well as what lies beyond does not matter, such that the plane with conductivity σ_2 in the analytic model can be considered as an extended edge channel.

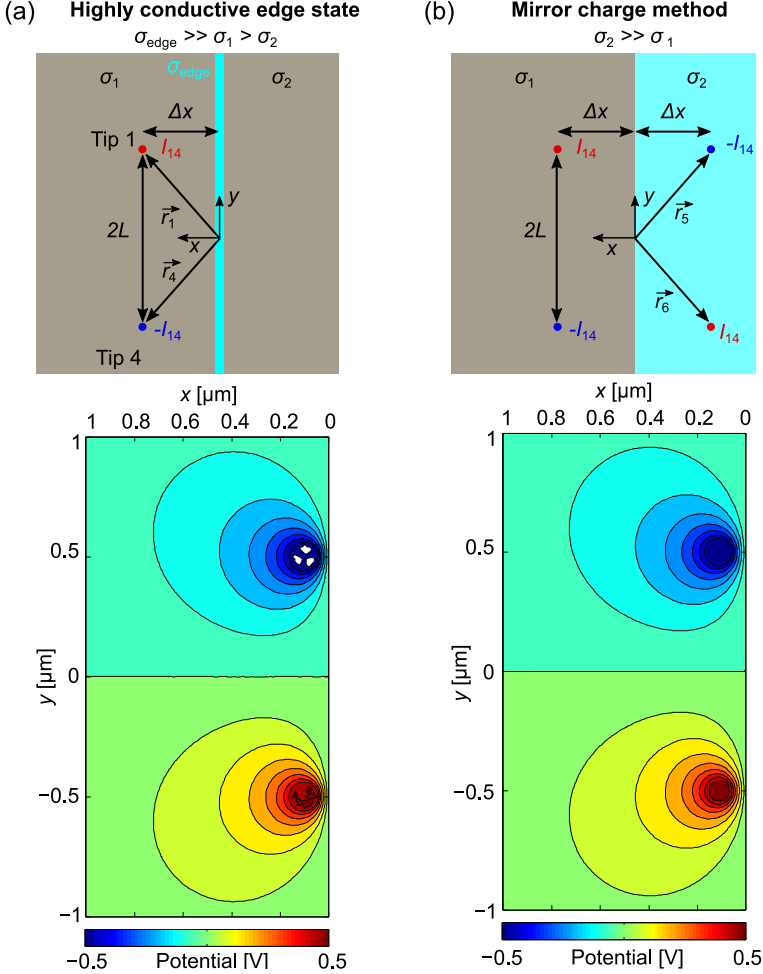


Fig. B.3.: Comparison of the electric potential due to a narrow highly conductive edge channel to that resulting from a highly conductive half-infinite plane. **(a)** Between two half-infinite regions with conductivities $\sigma_1 > \sigma_2$, an edge region with a high conductivity $\sigma_{\text{edge}} \gg \sigma_1 > \sigma_2$ at $x = 0$ is assumed. In correspondence to the experiment, a bias voltage of $\pm 0.5\text{V}$ is defined at the positions of the current-injecting tips parallel to the boundary line at a distance $\Delta x = 150\text{nm}$. As shown in the bottom panel, the resulting electric potential that is obtained from finite element calculations is distorted due to the presence of the conducting edge channel. The discontinuities close to the contact region are artifacts of the numerical calculation due to discretization. **(b)** In the analytic model, the same configuration is applied, but without the edge region at $x = 0$. Instead, $\sigma_2 \gg \sigma_1$ is assumed, such that the resulting potential can be described analytically by using the method of mirror images. For this purpose, imaginary sources with opposite sign are inserted across the boundary for each of the two real current sources. As evident from the lower panel, both methods yield the same electric potential.

Technical descriptions

C.1. Contacting procedure

To be able to perform four-point measurements with the multi-tip STM, it is necessary to bring the individual STM tips into direct contact to the sample surface. As both, damage to the sample and deformations of the tips, are to be prevented, the contacting procedure has to be carried out in a cautious and controlled manner.

To establish hard contact to a grounded sample, the STM tips are first approached into tunneling contact with the sample surface. While in tunneling contact, the STM feedback is deactivated and the tip is simultaneously retracted several nanometers, leaving it stationary above the sample. In this state, the respective tip is gently lowered to the surface manually by small adjustments of the voltage that is applied to the piezo element of the nanopositioner. This is done incrementally until a sudden increase of the current, usually to $\gtrsim 1 \mu\text{A}$, is registered, which is used as the indication of successful establishment of hard contact.

Depending on the condition of the tip apex, it is possible that the contact resistance is too high to reach the desired current range, e.g. when the apex is covered by contaminations after prolonged use. In this case, the onset of a current cannot be used reliably as an indication of hard contact, since electrical contact might not be perceived as such, even if the tip is already touching the surface. Alternatively, the tip can be switched into voltage-probe mode during the manual lowering of the tip. Whether the tip is in hard contact to the surface yet can then be verified by observing the recorded voltage signal. If the measured voltage floats to some unspecific value, the tip is still above the surface. If the voltage fluctuates around $\sim 0\text{V}$, hard contact is established.

C.2. Tip cleaning

C.2.1. Cleaning by field emission

Before fresh STM tips can be used in the experiment, a cleaning procedure has to be carried out to remove the natural oxide layer on their apices. If this is not done, the resistance of the tip-sample junction is too high to establish tunneling contact, which results in a crash of the tip during approaching. To clean the tips from their oxide layers a cleaning procedure based on field emission is employed immediately after introduction into the UHV system.

The tip that is cleaned by field emission is connected to ground potential via a 100 M Ω resistance and a current meter with sufficient resolution. The analog output of the current meter is connected to an input channel of the Createc box to observe the emission current in the STM software. On the other side of the circuit, a template Omicron plate of stainless steel is inserted into the sample slot and connected to a HV power source with a BNC cable. To initiate the field emission process, the respective tip is first brought into position above the sample plane by roughly approaching it to the same focus in the optical microscope. Typically, a distance of $\sim 200\ \mu\text{m}$ between the tip and the steel plate results in the used setup. With the tip in position, the bias voltage applied to the plate is increased incrementally in steps of $\sim 25\ \text{V}$ until an increase of the measured current (usually $< 5\ \text{nA}$) from the noise level is observed in the data recorder of the STM software. The corresponding voltage that is required for the onset of current generally depends on the quality of the tip (apex geometry, oxide thickness) and the distance to the steel plate. Typical voltages for fresh tips with good quality are in the range of 200 V – 300 V. In case of blunt tips that were exposed to ambient conditions for a long time, it is possible to not see any emission current at voltages up to 1 kV, which is an indication of poor tip quality. To start the cleaning process, the bias voltage is carefully increased further until the emission current amounts to $\sim 100\ \text{nA}$. Usually, the required additional increase in voltage is only 10 V – 30 V from the point of current onset. In these conditions, large fluctuations of the emission current by $\pm 50\ \text{nA}$ within a few seconds at constant bias voltage are common, initially. After a few minutes of prolonged field emission, the measured current naturally rises to $\sim 200\ \text{nA}$ – 300 nA, which requires a manual adjustment of the voltage to reobtain the setpoint value of 100 nA. Occasionally, multiple fine adjustments of the current are necessary over the course of the entire process. After a continued field emission for 15–30 minutes, the current is generally observed to fluctuate less with approximately $\pm 20\ \text{nA}$. At this point, the tip is considered clean and the process is terminated by ramping down the voltage.

C.2.2. Cleaning in hard contact

During the investigation of a sample, the STM tips can occasionally pick up sample material that sticks to the tip apex and increases the contact resistance. Contaminations like this impede clean imaging and the establishing of ohmic contact to samples in further measurements if the same tips are reused. Simple application of voltage pulses in tunneling contact often does not suffice to remove the contaminations, which requires a more thorough procedure. In general, a current of $> 1 \mu\text{A}$ is fed through the tip while in hard contact with a sample to remove minor contaminations. This is oftentimes more reliable than the fundamentally similar approach of voltage pulsing in tunneling contact, since the current used for cleaning is larger.

Once hard contact is established to the surface, the applied bias voltage is varied, which results in a response of the current to ground. The magnitude of the response is usually small if the tip is contaminated, with $< 0.1 \mu\text{A}$ at $\sim 1\text{V} - 2\text{V}$. This response also confirms that there is hard contact to the surface. The bias voltage is then increased, typically up to $\sim 6\text{V} - 8\text{V}$, until a large and sudden increase of the current occurs, which is interpreted as a sudden reduction of the contact resistance as the contamination on the tip is removed. Depending on the conductivity of the sample, the current might reach the setpoint current after the sudden drop of the contact resistance, leading to the onset of the tip feedback. If this happens, the bias voltage is reduced until the current is below the setpoint value again.

Lastly, it remains to confirm that a macroscopic current, e.g. $\sim 1 \mu\text{A}$, can be achieved with much lower bias voltage, e.g. $\sim 1\text{mV}$ on a highly conducting stainless steel sample, than before cleaning. After the successful cleaning, the tip is retracted.

Empirically, this procedure works better the more conducting the template sample is. As a reference, a BST sample with $\sigma_{2D} \approx 3\text{mS}$ typically yields satisfying results. Another very reliable example is a simple Omicron plate of stainless steel.

C.3. Preparation of UHV suitcase

The vacuum suitcase is used to transfer delicate samples between different UHV systems without exposing them to atmospheric conditions. As depicted in Fig. C.1 (a), the vacuum suitcase consists of a small chamber with two CF 35 view ports, a cold cathode ionization gauge and a wobble stick that allows for the storage of one sample at a time. Additionally, a passive non-evaporable getter (NEG) pump by Gamma Vacuum is installed to maintain low pressures in the chamber for extended periods of time without the need of a power supply. The small design and low weight of the vacuum suitcase makes it very convenient for quick

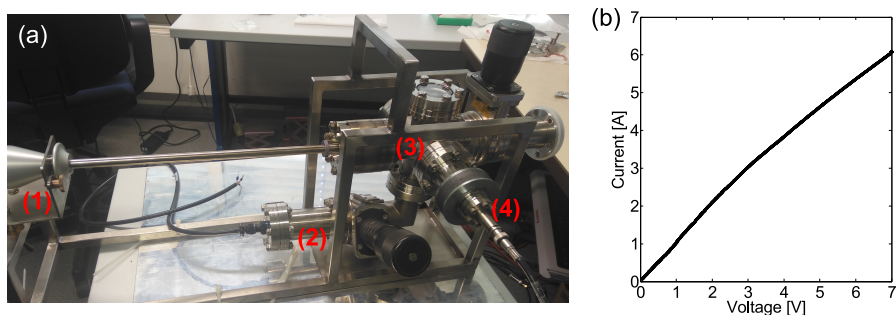


Fig. C.1.: (a) Photograph of the UHV suitcase that was used for the transfer of all investigated samples in this work. (1) Wobble stick used for the manipulation and storage of a transferred sample. (2) NEG pump segment with a power supply cable connected to its feedthrough. (3) Body of the suitcase that the sample is situated in. (4) Feedthrough of the pressure sensor inside the chamber. (b) I-V characteristics of the NEG pump. For conditioning, the pump is treated with resistive heating by applying a current of $\sim 6\text{A}$ for 1 hour.

sample transfer.

The passive NEG pump establishes and maintains low pressure by adsorbing residual gas molecules in the chamber and forming compounds on its surface. On its own, with prolonged time, the pressure in the vacuum suitcase rises as the surface area of the getter material saturates with the residual gas. With an initial pressure of $\sim 10^{-10}$ mbar, the NEG pump can maintain this order of magnitude for approximately one month, before it usually goes up to 10^{-8} mbar within a few weeks. Once the pressure reaches $\sim 10^{-7}$ mbar, it is advised to condition the suitcase by baking the chamber and reactivating the NEG pump.

Prior to the conditioning process, a turbomolecular pump is connected to the valve of the suitcase chamber and switched on. After letting the turbomolecular pump run for about 20–30 minutes, the valve to the suitcase chamber is opened. This usually causes the pressure in the chamber to settle in the 10^{-7} mbar range. If the eventual pressure exceeds $1 \cdot 10^{-5}$ mbar, there is probably a leak between the valve and the turbomolecular pump that needs to be removed before conditioning.

For conditioning, the vacuum suitcase is first wrapped in heating elements and packaged in aluminium foil to ensure a uniform distribution of heat during baking. Using a temperature controller, the heating elements are heated up to 150°C incrementally and slowly, usually within a span of 1-2 hours, to reduce thermal stress due to excessive local overheating. During this process, the pressure inside the suitcase typically rises to the medium 10^{-6} mbar range. Once the temperature of the wall of the chamber has reached 150°C , the vacuum suitcase is left in this state to be pumped until the pressure has dropped to the upper 10^{-8} mbar range,

which can typically be reached overnight. Baking and pumping the suitcase for a full day is ideal and usually results in the pressure to settle in the medium 10^{-8} mbar range. When the pressure is satisfying, the heating elements can be turned off so that the chamber can cool down. After 1-2 hours, when the chamber is not hot anymore, the conditioning of the NEG pump can be initiated.

The conditioning of the NEG pump is done by treating it with resistive heating at temperatures close to 400°C to remove compounds that formed on the surface of the getter material as a cause of the normal operation of the pump. In order to begin the conditioning process, the input of the NEG pump feedthrough has to be connected to a low voltage power supply via a specific cable (NEG Cables-N-S1-N50). Using the power supply, the bias voltage is increased slowly (over a span of a few minutes) until a current of 6A is reached. This should happen at a voltage of $\sim 7\text{V}$. For voltages $> 4\text{V}$, the NEG element heavily degasses, leading to a rise of the pressure up to $1 \cdot 10^{-5}$ mbar. A detailed I-V curve of the NEG element can be seen in Fig. C.1 (b). At a current of 6A, the temperature of the NEG pump should be approximately 370°C . After one hour in this state, the power supply is turned off to finish the conditioning process. As the NEG element cools down, the pressure in the chamber drops quickly before eventually saturating in the 10^{-9} mbar range after approximately 1-2 hours. Finally, the valve between the suitcase chamber and the turbomolecular pump is closed and the turbomolecular pump is turned off and disconnected, so that the pressure in the chamber can drop further. After a day of being pumped by the NEG pump, the vacuum suitcase should contain a pressure of $1 \cdot 10^{-10}$ mbar.

Band / Volume 57

Resistive switching phenomena in stacks of binary transition metal oxides grown by atomic layer deposition

H. Zhang (2019), ix, 196 pp

ISBN: 978-3-95806-399-0

Band / Volume 58

Element-Selective Investigation of Femtosecond Spin Dynamics in Ni_xPd_{1-x} Magnetic Alloys using Extreme Ultraviolet Radiation

S. Gang (2019), 93, xx pp

ISBN: 978-3-95806-411-9

Band / Volume 59

Defect engineering in oxide thin films

F. V. E. Hensling (2019), 10, 164 pp

ISBN: 978-3-95806-424-9

Band / Volume 60

Chemical control of the electrical surface properties of *n*-doped transition metal oxides

M. Andrä (2019), X, 150, XXXVIII pp

ISBN: 978-3-95806-448-5

Band / Volume 61

Digital Signal Processing and Mixed Signal Control of Receiver Circuitry for Large-Scale Particle Detectors

P. Muralidharan (2020), xv, 109 pp

ISBN: 978-3-95806-489-8

Band / Volume 62

Development of Electromagnetic Induction Measurement and Inversion Methods for Soil Electrical Conductivity Investigations

X. Tan (2020), ix, 124 pp

ISBN: 978-3-95806-490-4

Band / Volume 63

Novel System Approach for a mm-range Precision Indoor Positioning System

R. Xiong (2020), xi, 144 pp

ISBN: 978-3-95806-517-8

Band / Volume 64

Quantitative investigation of group III-nitride interfaces by a combination of scanning tunneling microscopy and off-axis electron holography

Y. Wang (2021), 102 pp

ISBN: 978-3-95806-534-5

Band / Volume 65

Scalable Control Electronics for a Spin Based Quantum Computer

L. Geck (2021), xiv, 114, xv-xxxiii

ISBN: 978-3-95806-540-6

Band / Volume 66

DNA-capped silver nanoparticles for stochastic nanoparticle impact electrochemistry

L. Nörbel (2021), VI, 142 pp

ISBN: 978-3-95806-541-3

Band / Volume 67

Development, characterization, and application of intraretinal implants

V. Rincón Montes (2021), XII, 173 pp

ISBN: 978-3-95806-553-6

Band / Volume 68

Optogenetic and electrical investigation of network dynamics in patterned neuronal cultures

T. J. J. Hondrich (2021), x, 177 pp

ISBN: 978-3-95806-555-0

Band / Volume 69

Disentangling parallel conduction channels by charge transport measurements on surfaces with a multi-tip scanning tunneling microscope

S. Just (2021), xii, 225 pp

ISBN: 978-3-95806-574-1

Band / Volume 70

Nanoscale four-point charge transport measurements in topological insulator thin films

A. Leis (2021), ix, 153 pp

ISBN: 978-3-95806-580-2

Weitere **Schriften des Verlags im Forschungszentrum Jülich** unter
<http://www.zb1.fz-juelich.de/verlagextern1/index.asp>

Information

Band / Volume 70

ISBN 978-3-95806-580-2